INFORMATION TO USERS

This manuscript has been reproduced from the microfilm master. UMI films the text directly from the original or copy submitted. Thus, some thesis and dissertation copies are in typewriter face, while others may be from any type of computer printer.

The quality of this reproduction is dependent upon the quality of the copy submitted. Broken or indistinct print, colored or poor quality illustrations and photographs, print bleedthrough, substandard margins, and improper alignment can adversely affect reproduction.

In the unlikely event that the author did not send UMI a complete manuscript and there are missing pages, these will be noted. Also, if unauthorized copyright material had to be removed, a note will indicate the deletion.

Oversize materials (e.g., maps, drawings, charts) are reproduced by sectioning the original, beginning at the upper left-hand corner and continuing from left to right in equal sections with small overlaps. Each original is also photographed in one exposure and is included in reduced form at the back of the book.

Photographs included in the original manuscript have been reproduced xerographically in this copy. Higher quality 6" x 9" black and white photographic prints are available for any photographs or illustrations appearing in this copy for an additional charge. Contact UMI directly to order.

UMI

A Bell & Howell Information Company
300 North Zeeb Road, Ann Arbor, MI 48106-1346 USA
313/761-4700 800/521-0600

OZONE DEPLETION AND BIOLOGICALLY RELEVANT ULTRAVIOLET RADIATION

by

Jun Zeng

RECOMMENDED:

Dr. Richard Benner

Dr. Sue Ann Bowling

Dr. David Eslinger

Dr. Koji Kawasaki

Dr. Brenton Watkins

Dr. Knut Stamnes, Chairman, Advisory Committee

Dr. John Morack, Head, Physics Department

APPROVED:

Dr. Paul Reichardt, Dean, College of Natural Sciences

Dr. Joseph Kan, Dean of the Graduate School

April 27, 1995

Date

OZONE DEPLETION AND BIOLOGICALLY RELEVANT ULTRAVIOLET RADIATION

A

THESIS

Presented to the Faculty

of the University of Alaska Fairbanks

in Partial Fulfillment of the Requirements

for the Degree of

DOCTOR OF PHILOSOPHY

By

Jun Zeng, B.S., M.S.

Fairbanks, Alaska

May 1995

Abstract

An atmospheric radiative transfer model is used to calculate surface spectral ultraviolet irradiance under cloud-free conditions, and compared with measurements made at Lauder, New Zealand (45^0S, 170^0E) before and after the eruption of Mt. Pinatubo, and including a snow-covered surface. The ratios of diffuse to direct irradiance depend critically on solar elevation, surface albedo, and aerosol extinction. Ozone changes have pronounced effects on the global UVB irradiance, but have only a minor effect on these ratios. The comparison suggests that the ultraviolet radiation exposure can be computed with confidence for clear sky conditions, if the appropriate atmospheric pressure and temperature profiles, ozonesonde data, surface albedo, and aerosol optical properties are available.

The total ozone abundances are derived by using ground-based UV irradiance measurements and compared with TOMS in Antarctica and the Arctic from 1990 to 1994. The comparisons show that they are generally in good agreement. Possible reasons for the discrepancies between the two methods are discussed. The equivalent cloud optical depths are also inferred from these data.

Ozone depletion can also increase the penetration of ultraviolet radiation into the aquatic system. A coupled atmosphere-ocean radiative transfer model is used to investigate the effect of ozone depletion on UV penetration through the atmosphere and into the underlying water column. Comparisons between model computations and *in situ* measurements of irradiances made in Antarctic water show good agreement in the UV spectral range between 300 and 350 nm. The ratio of UVB (280 - 320 nm) to total (280 - 700 nm) irradiance also compared well. For a

given ozone reduction the largest relative increase of UVB radiation arriving at the surface and penetrating to various depths in the ocean occurs at large solar zenith angles. At high latitudes the most pronounced increase in UVB exposure due to an ozone depletion occurs in the early spring, when ozone depletion is expected to be the most severe.

The sensitivities of irradiance reflectance and diffuse attenuation coefficients to solar zenith angle, sky conditions, and chlorophyll concentration are discussed by using a coupled atmosphere-ocean radiative transfer model. The irradiance reflectance is sensitive to solar zenith angle, cloud cover, and chlorophyll concentration; the diffuse attenuation coefficient is sensitive to solar zenith angle and chlorophyll concentration, but less sensitive to sky conditions.

Contents

List of Figures

List of Tables

Acknowledgments

I would like to give my most sincere gratitude to Dr. Knut Stamnes for encouragement, understanding, support, and patient guidance; Dr. David Eslinger for tutoring me in biological oceanography, encouraging me to explore the colorful oceanic world, and spending long hours reading my writing; Drs. Richard Benner, Sue Ann Bowling, Koji Kawasaki, and Brenton Watkins for constructive discussions and criticism of this work; Dr. Richard McKenzie of NIWA, New Zealand for taking time out of his heavy schedule to respond in well thought out E-mail to my sometimes half formed and unclear analysis, and for teaching me rigorous scholarship in forming a scientific paper; Drs. C.R. Booth, Tim B. Lucas, and John H. Morrow of Biospherical Instruments Inc. for kindly providing me the NSF/UV data and useful discussions. I would also like to thank Dr. Si-Chee Tsay, all my friends and fellow graduate students, too many to mention, for criticism, discussions, and cooperations; the National Science Foundation for financial support.

Thanks goes to my beloved parents who live far away in China for their understanding and endless supporting during my pursuit of Ph.D. at the University of Alaska Fairbanks. It is to them that I dedicate this dissertation. Final thanks goes to my dear husband and lovely daughter for their encouragement and understanding.

Chapter 1

Introduction

Ozone is produced when molecular oxygen absorbs solar ultraviolet energy and breaks up into oxygen atoms. The oxygen atoms then react with molecular oxygen to form ozone. Ozone itself absorbs both visible and ultraviolet light to produce an oxygen molecule and an oxygen atom. Oxygen atoms react rapidly with oxygen molecules to form ozone. Some of the oxygen atoms, however, react with the ozone to reform two oxygen molecules, thus causing a loss of ozone. Through this process, called the Chapman mechanism, a balance of ozone concentration is established which is greatest in the lower stratosphere between about 15 and 30 km of altitude. This ozone layer prevents much of the sun's ultraviolet radiation from reaching the earth's surface although ozone constitutes less than one part per million of the gases in the atmosphere.

A summary of the solar flux at the top of the atmosphere is provided in Table 1. Most of the radiative energy is in the infrared and visible regions. Emission at wavelengths shorter than 280 nm (UVC) accounts for only 0.5% of the total ir-

Table 1.1 Wavelength distribution of solar irradiance prior to attenuation by the earth's atmosphere. (After *Frederick et al.*, 1989) .

Wavelength region	Irradiance (W/m^2)	Percent of total
UV-C (< 280 nm)	6.4	0.5
UV-B (280-320 nm)	21.1	1.5
UV-A (320-400 nm)	85.7	6.3
Visible (400-700 nm)	532	38.9
Infrared (> 700 nm)	722	52.8

radiance, while the UVB (280-320 nm) and UVA (320-400 nm) regions constitute 1.5% and 6.3% of the total solar irradiance, respectively. Absorption by molecular oxygen and ozone prevents essentially all UVC radiation from reaching the surface of the earth.

Farman and his coworkers (1985) first reported that significant ozone depletion had been occurring over Antarctica since the late 1970s. Measurements made with balloon-borne sensors (*Hofmann et al.*, 1987) showed that the maximum ozone depletion occurred between 14 and 22 km altitude, indicating that ozone depletion occurs at the altitude of maximum ozone concentration. Satellite measurements from *Nimbus* 7 showed that over the years the depletion from austral spring to austral spring has generally worsened. About 70% of the ozone above Antarctica, which equals about 3% of the total stratospheric ozone, is lost during September and October. The dramatic loss of so much ozone over such a short time demonstrates that global-scale atmospheric changes can occur very rapidly. Although remotely located, the ozone "hole" in Antarctica is nonetheless cause for concern: shifting circulation patterns carry masses of ozone-depleted air north. It may thus

forebode widespread ozone depletion throughout the stratosphere.

Significant ozone reduction in the stratosphere has already been reported from the re-analysis of the Total Ozone Mapping Spectrometer (TOMS) observations with a new retrieval method based on internally self-consistent calibration (*Herman et al.*, 1991). Measurements made by the Stratospheric Aerosol and Gas Experiment (SAGE) have shown that the most important decreases are occurring in the lower stratosphere (*McCormick et al.*, 1992). The TOMS total ozone data from November 1978 to March 1991 indicate a seasonally averaged decrease of 4% per decade in the Southern Hemisphere around 40^0 S, the reduction becoming larger when moving southward. In the Northern Hemisphere, the 4% contour line varies from 30^0 N in the winter to 60^0 N in the summer (*Stolarski et al.*, 1992). The largest decrease in Antarctica occurred in October during the Austral spring, reaching more than a factor of 2 in 1992 as compared to the value observed in the 1960's. In the Northern Hemisphere, the maximum reduction took place during the winter and spring, at high latitudes.

Scientists have advanced a number of theories to explain what causes the Antarctic ozone hole. The most convincing one is the PSC (polar stratospheric clouds)-chlorofluorocarbon theory.

Chlorofluorocarbons (CFCs) are useful substances, which are excellent for refrigeration, insulation, and cleaning of sophisticated electronics and instruments. They contain only carbon and a selection of chlorine, fluorine, and hydrogen atoms. Other manufactured chemicals, such as halons, which also contain bromine, are used to extinguish fires where people and electronic equipment are likely to be present. These chemicals are virtually nonreactive, noncorrosive, and nontoxic.

CFCs may survive 50 to 100 years in the atmosphere. In only a few years, winds throughout the troposphere uniformly distribute CFC molecules released from a single point. Over the decades, the molecules eventually reach the middle stratosphere, about 30 km or higher. They are harmless to ozone until they have been photolysed in the stratosphere into chlorine, which is capable of depleting the earth's protective shield of ozone. Each Cl atom can destroy 100,000 ozone molecules through catalytic cycles. The agreement already obtained between atmospheric observations and computer simulations provides strong scientific evidence that CFCs released at the surface are linked to ozone depletion in the stratosphere (*WMO*, 1985). It is now believed (*Anderson et al.*, 1991) that at least 95% of the chemically catalyzed ozone loss can be attributed to two chemical schemes: About 75% of the ozone loss results from reactions involving the ClO dimer, and most of the remaining ozone is destroyed in reactions involving bromine (*McElroy et al.*, 1986).

The release of CFCs from human activities, mainly in the Northern Hemisphere, is responsible for depleting ozone in the Southern Hemisphere because the long atmospheric lifetime of CFCs causes them to be uniformly distributed throughout the atmosphere. The ozone hole occurs near Antarctica during spring because the formation of the hole requires the presence of stratospheric clouds, which form only during the coldest times of the year. The first rays of spring sunlight initiate the chemical reactions that deplete ozone.

The ozone loss is more severe over Antarctica than over the Arctic because the Antarctic stratosphere is colder, enabling more polar stratospheric clouds to form. More clouds produce additional reactive chlorine atoms and remove nitrogen

compounds, leading to greater ozone loss. A more important difference between the two poles concerns the longevity of the Antarctic vortex, which remains intact throughout the polar winter, well into midspring. In the Arctic, where circulation patterns differ significantly from those in Antarctica, the vortex has usually disintegrated long before the polar spring arrives.

All other factors being constant, depletion of stratospheric ozone implies increased transmission of solar ultraviolet radiation to the surface of the earth. For moderate ozone changes, the radiation most likely to be affected falls in the UVB range, and to a much lesser extent in the UVA range (as shown in Figure 2.1b). Many biological processes are sensitive to the radiation at these wavelengths from 280 to 400 nm.

The biological response to UV radiation is generally a function of wavelength. A few of these response functions, termed biological *action spectra*, are shown in Figure 1.1. Typically, sensitivities are greatest at the shortest wavelengths, and fall rapidly with increasing wavelength. The biological effect of UV radiation may be expressed in terms of the effective UV-dose defined as a convolution of an action spectrum with the irradiance spectrum. The dose rate and the daily (yearly) dose D are given by (*cf. e.g. Dahlback et al.*, 1989)

$$\frac{dD}{dt} = \int A(\lambda)F(\lambda)d\lambda \tag{1.1}$$

$$D = \int dt \int A(\lambda)F(\lambda)d\lambda \tag{1.2}$$

where the time integral is over one day (year), $A(\lambda)$ is the action spectrum of

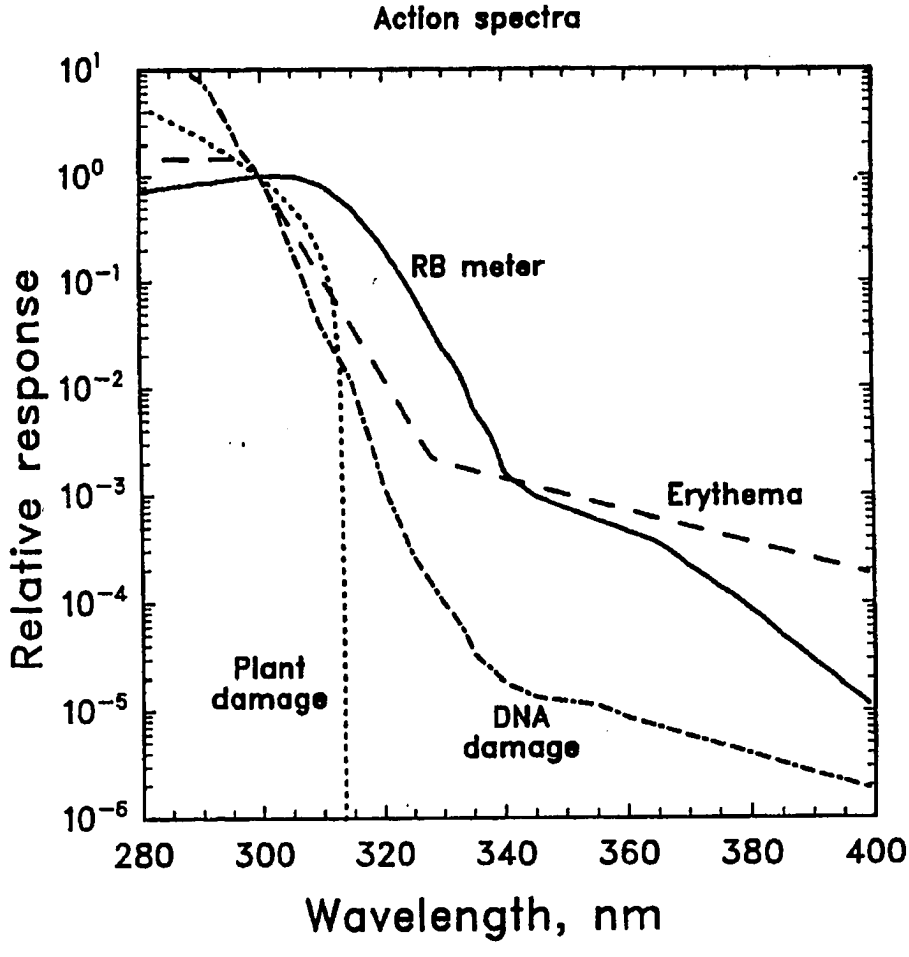

Figure 1.1 Action spectra used in computations of effective UV doses. All spectra are normalized to unity at 300 nm. From *Madronich* (1992).

the particular biological response studied, and $F(\lambda)$ is the irradiance per unit wavelength interval reaching the biosphere. For different biological responses, UV irradiance $[F(\lambda)]$ varies with atmospheric conditions. Therefore, we will focus in this study on investigations of the changes in UV radiation reaching the biosphere in response to ozone depletion.

The radiative transfer equation (*cf. e.g. Thomas and Stamnes, 1995*), which includes both scattering and absorption of the medium, may be written as

$$\frac{dI(\tau_s,\hat{\Omega})}{d\tau_s} = -I(\tau_s,\hat{\Omega}) + (1-a)B(T) + \frac{a}{4\pi}\int_{4\pi} d\omega' p(\hat{\Omega}',\hat{\Omega})I(\tau_s,\hat{\Omega}') \qquad (1.3)$$

where the radiance (or intensity) $I(\tau_s,\hat{\Omega})$ and Plank function $B(T)$ at temperature T are the functions of the frequency of the photon. τ_s is the optical path of the medium along the ray, and it a dimensionless quantity, $d\tau_s$ = -$k\rho ds$, where k $[m^2 ky^{-1}]$ is the mass extinction coefficient, ρ $[kg\ m^{-3}]$ is the density of the medium, and ds $[m]$ is the medium thickness the photon traversed; a is the single-scattering albedo which can be interpreted as the probability that a photon will be scattered in a given extinction event, with a perfect scatterer having $a = 1$ and a perfect absorber $a = 0$. The second term on the right hand side is the thermal emission which increases the radiation along the ray. $p(\hat{\Omega}',\hat{\Omega})$ is the phase function which is the probability of scattering in the angle (Θ) between the incoming $(\hat{\Omega}')$and the outgoing $(\hat{\Omega})$ directions, and $d\omega'$ is a small solid angle around the incoming beam direction. So given that a scattering event has occurred, the probability that a photon is scattered from direction $\hat{\Omega}'$ within solid angle $d\omega'$ into the direction $\hat{\Omega}$ is $p(\hat{\Omega}',\hat{\Omega})d\omega'/4\pi$. Therefore, the third term on the right hand side represents the

multiple scattering from all incoming directions to the direction of propagation $\hat{\Omega}$.

In all atmospheres, the force of gravitation imposes a density stratification, so that the principal direction of variation of properties is in the vertical. This means that in most situations we can ignore the horizontal variability of the atmosphere, and take the variation to be only in the vertical direction. If we also ignore the spherical nature of the atmosphere, we call these assumptions plane-parallel, or slab, geometry. In this geometry it is convenient to measure the optical depth along the vertical rather than along the slant ray path. We choose to measure optical depth vertically downward from the 'top' of the atmosphere. Then we have

$$\tau = \int_z^\infty k\rho dz' = \frac{\tau_s}{\cos\theta} \tag{1.4}$$

where θ is the polar angle of the ray path. The following convention is adopted to express the zenith angle

$$u = \cos\theta \qquad : -1 \leq u \leq 1 \tag{1.5}$$

and

$$\mu = |u| \qquad : 0 \leq \mu \leq 1. \tag{1.6}$$

The radiative transfer equation 1.3 becomes

$$u\frac{dI(\tau,u,\phi)}{d\tau} = I(\tau,u,\phi) - (1-a)B(T) - \frac{a}{4\pi}\int_0^{2\pi} d\phi' \int_{-1}^{1} du' p(u',\phi';u,\phi) I(\tau,u',\phi') \tag{1.7}$$

where ϕ is the azimuthal angle. It is convenient to deal with half-range intensities in a slab geometry, such that

$$I^+(\tau,\theta,\phi) = I(\tau,\theta \leq \pi/2,\phi) \tag{1.8}$$

$$I^-(\tau,\theta,\phi) = I(\tau,\theta > \pi/2,\phi). \tag{1.9}$$

Substituting the above expression into equation 1.7 one obtain the half-range intensities

$$\mu\frac{dI^+(\tau,\mu,\phi)}{d\tau} = I^+(\tau,\mu,\phi) - S(\tau,\mu,\phi) \tag{1.10}$$

$$-\mu\frac{dI^-(\tau,\mu,\phi)}{d\tau} = I^-(\tau,\mu,\phi) - S(\tau,\mu,\phi) \tag{1.11}$$

where $S(\tau,\mu,\phi)$ called source function

$$S(\tau,\mu,\phi) = (1-a)B(T) + \frac{a}{4\pi}\int_0^{2\pi} d\phi' \int_{-1}^{1} du' p(u',\phi';u,\phi) I(\tau,u',\phi'). \tag{1.12}$$

Note that the independent variable is now the vertical optical depth, measured downwards from the 'top' of the medium. This accounts for the difference in sign of the left hand side of equation 1.11. We can also rewrite equations 1.10 and 1.11 as

$$\begin{aligned}\mu\frac{dI^+(\tau,\hat{\Omega})}{d\tau} &= I^+(\tau,\hat{\Omega}) - (1-a)B - \frac{a}{4\pi}\int_+ d\omega' p(\hat{\Omega}',\hat{\Omega}) I^+(\tau,\hat{\Omega}') \\ &\quad -\frac{a}{4\pi}\int_- d\omega' p(-\hat{\Omega}',\hat{\Omega}) I^-(\tau,\hat{\Omega}')\end{aligned} \tag{1.13}$$

$$\begin{aligned}-\mu\frac{dI^-(\tau,\hat{\Omega})}{d\tau} &= I^-(\tau,\hat{\Omega}) - (1-a)B - \frac{a}{4\pi}\int_+ d\omega' p(\hat{\Omega}',-\hat{\Omega}) I^+(\tau,\hat{\Omega}') \\ &\quad -\frac{a}{4\pi}\int_- d\omega' p(-\hat{\Omega}',-\hat{\Omega}) I^-(\tau,\hat{\Omega}').\end{aligned} \tag{1.14}$$

We have used the notation $I^-(\tau,\mu,\phi) = I^-(\tau,\hat{\Omega}) \equiv I(\tau,-\hat{\Omega})$, whereas the notation $p(-\hat{\Omega}',\hat{\Omega})$ (for example) indicates that a photon is moving downward before the scattering $(-\hat{\Omega})$, and upward $(\hat{\Omega})$ after the scattering.

There are two distinctly different components of the solar radiation field. The first one is the direct or solar component I_s which is that part of the solar radiation field which has survived extinction, *i.e.*

$$I_s^-(\tau,\hat{\Omega}) = F^s e^{-\tau/\mu_0}\delta(\hat{\Omega}-\hat{\Omega}_0) = F^s e^{-\tau/\mu_0}\delta(\mu-\mu_0)\delta(\phi-\phi_0). \tag{1.15}$$

The second part of the radiation is the diffuse component, I_d, which consists of light that has been scattered at least once. Therefore,

$$I^-(\tau,\hat{\Omega}) = I_d^-(\tau,\hat{\Omega}) + I_s^-(\tau,\hat{\Omega}) \tag{1.16}$$

$$I^+(\tau,\hat{\Omega}) = I_d^+(\tau,\hat{\Omega}) + I_s^+(\tau,\hat{\Omega}) \tag{1.17}$$

where we have ignored thermal radiation emitted from the surface. The intensity of attenuated direct (solar) radiation, that has been diffusely reflected at the surface in direction $\hat{\Omega}$ and subsequently propagated to level τ, is

$$I_s^+(\tau,\hat{\Omega}) = e^{-(\tau^*-\tau)/\mu}\mu_0\rho(-\hat{\Omega}_0,\hat{\Omega})F^s e^{-\tau^*/\mu_0} \tag{1.18}$$

where τ^* is the total optical depth of the medium from top to the lower boundary, μ_0 is the cosine of solar zenith angle, and $\rho(-\hat{\Omega}_0,\hat{\Omega}')$ is the bidirectional reflectance function, or in short the reflectance, of the lower boundary which is the ratio of the reflected intensity to the energy in the incident beam.

Now substituting for the total intensity field and using equation 1.15, we obtain

$$-\mu\frac{dI_d^-(\tau,\hat{\Omega})}{d\tau} = I_d^-(\tau,\hat{\Omega}) - (1-a)B - S^*(\tau,-\hat{\Omega}) - \frac{a}{4\pi}\int_+ d\omega' p(\hat{\Omega}',-\hat{\Omega})I_d^+(\tau,\hat{\Omega}') - \frac{a}{4\pi}\int_- d\omega' p(-\hat{\Omega}',-\hat{\Omega})I_d^-(\tau,\hat{\Omega}') \quad (1.19)$$

where

$$S^*(\tau,-\hat{\Omega}) = \frac{a}{4\pi}\int_- d\omega' p(-\hat{\Omega}',-\hat{\Omega})F^s e^{-\tau/\mu_0}\delta(\hat{\Omega}'-\hat{\Omega}_0) + \frac{a\mu_0 F^s e^{-\tau^*/\mu_0}}{4\pi}\int_+ d\omega' p(\hat{\Omega}',-\hat{\Omega})\rho(-\hat{\Omega}_0,\hat{\Omega}')e^{-(\tau^*-\tau)/\mu'} \quad (1.20)$$

$$= \frac{a}{4\pi}p(-\hat{\Omega}_0,-\hat{\Omega})F^s e^{-\tau/\mu_0} + \frac{a\mu_0 F^s e^{-\tau^*/\mu_0}}{4\pi}\int_+ d\omega' p(\hat{\Omega}',-\hat{\Omega})\rho(-\hat{\Omega}_0,\hat{\Omega}')e^{-(\tau^*-\tau)/\mu'} \quad (1.21)$$

and

$$\mu\frac{dI_d^+(\tau,\hat{\Omega})}{d\tau} = I_d^+(\tau,\hat{\Omega}) - (1-a)B - S^*(\tau,+\hat{\Omega}) - \frac{a}{4\pi}\int_+ d\omega' p(\hat{\Omega}',\hat{\Omega})I_d^+(\tau,\hat{\Omega}') - \frac{a}{4\pi}\int_- d\omega' p(-\hat{\Omega}',\hat{\Omega})I_d^-(\tau,\hat{\Omega}') \quad (1.22)$$

where

$$S^*(\tau,+\hat{\Omega}) = \frac{a}{4\pi}\int_- d\omega' p(-\hat{\Omega}',\hat{\Omega})F^s e^{-\tau/\mu_0}\delta(\hat{\Omega}'-\hat{\Omega}_0) + \frac{a\mu_0 F^s e^{-\tau^*/\mu_0}}{4\pi}\int_+ d\omega' p(\hat{\Omega}',+\hat{\Omega})\rho(-\hat{\Omega}_0,\hat{\Omega}')e^{-(\tau^*-\tau)/\mu'} \quad (1.23)$$

$$= \frac{a}{4\pi}p(-\hat{\Omega}_0,\hat{\Omega})F^s e^{-\tau/\mu_0} + \frac{a\mu_0 F^s e^{-\tau^*/\mu_0}}{4\pi}\int_+ d\omega' p(\hat{\Omega}',+\hat{\Omega})\rho(-\hat{\Omega}_0,\hat{\Omega}')e^{-(\tau^*-\tau)/\mu'} \quad (1.24)$$

The first term of $S^*(\tau,\pm\hat{\Omega})$ presents single-scattering source function which "drives" the diffuse radiation field. Without this term there would be no diffuse

radiation. Therefore, both the direct and the diffuse radiation are proportional to F^s, the solar flux incident at the top of the medium.

If the reflected intensity from a diffuse surface is completely uniform with angle of observation, it is called a Lambert surface. The reflectance of a Lambert surface is independent of both the direction of incidence and the direction of observation, but may depend upon frequency, *i.e.*,

$$\rho(\nu, -\hat{\Omega}', \hat{\Omega}) = \rho_L(\nu). \tag{1.25}$$

With this assumption the implementation of the lower boundary condition is somewhat simplified.

Downward and upward vertical fluxes (or irradiance) are defined as the normal component of the radiance integrated over the downward and upward hemisphere, respectively (*Liou*, 1980). The downward, upward, and net fluxes can be written as

$$F^-(\tau) = -\int_- d\omega \cos\theta I^-(\hat{\Omega}) = \int_0^{2\pi} d\phi \int_0^1 d\mu\mu I^-(\tau, \theta, \phi) \tag{1.26}$$

$$F^+(\tau) = \int_+ d\omega \cos\theta I^+(\hat{\Omega}) = \int_0^{2\pi} d\phi \int_0^1 d\mu\mu I^+(\tau, \theta, \phi) \tag{1.27}$$

$$F(\tau) = \int_- d\omega \cos\theta I^-(\hat{\Omega}) + \int_+ d\omega \cos\theta I^+(\hat{\Omega}) = F^+(\tau) - F^-(\tau). \tag{1.28}$$

From the equations 1.19 and 1.22, and boundary conditions

$$I_s^-(0, \hat{\Omega}) = F^s \delta(\mu - \mu_0)\delta(\phi - \phi_0) \qquad (equation\ 1.15\ \ when\ \ \tau = 0) \tag{1.29}$$

$$I_d^+(\tau^*, \hat{\Omega}) = \int_- d\omega' \cos\theta' \rho(-\hat{\Omega}', \hat{\Omega}) I_d^-(\tau^*, \hat{\Omega}') \tag{1.30}$$

and

$$I_d^-(0, -\hat{\Omega}) = 0 \qquad (all\hat{\Omega}) \tag{1.31}$$

combined with definition 1.26 to 1.28, we can solve for downward solar, downward diffuse, upward solar, and upward diffuse irradiances. For the biologically effective radiation, we are interested in downward irradiance which is the summation of downward solar and downward diffuse fluxes.

Equation 1.15, which is the source driving diffuse radiation, shows that decreases in optical depth which could be caused by ozone depletion will increase radiative transmission. Research has indicated that reduction in stratospheric ozone will increase UVB radiation penetration through the atmosphere and into the ocean. Such radiation can affect the growth and reproduction of land-based plants as well as phytoplankton, which constitutes the base of the marine food chain, and may be detrimental to various forms of marine life in the upper layers of the ocean. In humans, excessive ultraviolet exposure has been implicated as a cause in skin cancers, cataracts and immune deficiencies.

The spectral distribution of solar radiation reaching the earth's surface depends on the irradiance emitted by the sun, the earth-sun distance and the transmission properties of the atmosphere. The modification of UVB by known changes in stratospheric ozone is, in principle, well understood, because the ozone absorption spectrum has been measured with sufficient accuracy (*DeMore et al.*, 1990). Geometric parameters, such as variations in the earth-sun distance and the angle of incidence of solar radiation at the top of the atmosphere (a function of time of day, year, and latitude) are easily calculated. Due to the changing earth-sun distance, the irradiance received at the top of the atmosphere varies with an annual cycle, being 3.3% above and below the yearly mean in January and July, respectively (*Nicolet*, 1975; *Frederick et al.*, 1989). Other environmental factors

known to affect the UVB levels include surface reflections, clouds, aerosols, and various tropospheric gases. These factors tend to be highly variable in both space and time, and may account for some of the conflicting trends in the few available long-term observational records of UVB radiation. It is likely that, in areas remote from anthropogenic sources of aerosols and other precursors of tropospheric ozone, the calculated UVB changes due to stratospheric ozone decreases would be only partially compensated by the possible effect of clouds (*UNEP*, 1991).

Unfortunately, we presently lack a coordinated, world-wide program to measure the corresponding changes in UVB surface radiation that would be implied by the observed ozone layer depletion. Only a few measurement sites around the world have indicated the UVB change that would be expected. In the absence of an organized world-wide measurement program, the changes occurring in UVB radiation may currently be best evaluated through the calculations using theoretical radiation models that account for all other factors that affect UV penetration besides total ozone abundance.

The purpose of this work is to investigate the effects of ozone depletion on UV penetration through the atmosphere and into the underlying aquatic system. In Chapter 2 a discrete ordinate method radiative transfer model (DISORT) for the atmosphere is used to explore the effects of atmospheric ozone, aerosol loading, solar zenith angle, surface albedo, and atmospheric pressure on the penetration of UV radiation arriving to the earth surface, and the model results are compared with ground-based measurements made in Lauder, New Zealand. Next, in Chapter 3 ground-based UV spectrometer measurements made in Antarctica and in the Arctic, and satellite data on ozone abundance are utilized in conjunction

with radiative transfer modeling to investigate the UV radiation budget in the polar regions. In Chapter 4 a coupled atmosphere-ocean radiative transfer model is used to calculate UV radiation into the aquatic system for comparison with *in situ* underwater UV light measurements. The impacts of ozone depletion on the submarine UV light field are presented and discussed. Chapter 5 discusses the sensitivity of two apparent optical properties, the irradiance reflectance and diffuse attenuation coefficients, in the water body to environmental parameters such as solar zenith angle, sky condition, and chlorophyll concentration. Finally, in Chapter 6 a summary of this work and suggestions for future research are provided.

Chapter 2

Measured UV Spectra Compared with Discrete Ordinate Method Simulations

2.1 Introduction

Ozone depletion, which was initially confined to the Antarctic region, is now apparent over much of the globe. Further depletion is expected, as atmospheric chlorine levels continue to rise (*WMO*, 1992), and even with full compliance to the Montreal Protocol and its amendments, ozone levels will remain below unperturbed levels

[0] This chapter is based on material previously published as Jun Zeng, Richard McKenzie, Knut Stamnes, Mary Wineland, and James Rosen, Measured UV spectra compared with discrete ordinate method simulations, *J. Geophys. Res.*, *99*, 23019-23030, 1994.

(pre 1970) until the middle of the next century. These ozone reductions are expected to lead to increases in biologically damaging UV irradiance, and changes in important photochemical reaction rates in the biosphere. Measurements as well as modeling studies have already investigated the increases in biologically damaging UV irradiance at the surface that results from these reductions in ozone (*WMO*, 1992; *UNEP*, 1991).

UV irradiance is also affected by clouds, aerosols, and tropospheric trace gases (*e.g.* SO_2, O_3). The spectral measurements required to evaluate the reasons for changes are available only at a small number of sites. Even with the best instruments available, it will be difficult to detect changes in UV of less than the 5-10% level because of difficulties with measurement calibration and instrument stability. Such changes, however, could have serious implications for the biosphere, including human health. Future changes in UV may also result from changes in aerosol and cloud patterns.

Therefore, we need to improve our understanding of the factors that affect UV irradiance, through the use of radiative transfer models. Earlier parametric models that have been used to calculate UV irradiances, such as the "Green" model (*Schippnick and Green*, 1982), do not explicitly solve the radiative transfer equation. The values of the free parameters are determined by constraining them to give agreement with available UV measurements (*e.g.* measurements by *Bener*'s (1972)). Consequently, good agreement between model and measurement can be achieved with such models for clear-sky conditions. However, because the physics in the models is incomplete, they are inadequate for modeling UV during cloudy conditions.

Since multiply-scattered light forms a large percentage of UV radiation at the surface, a more rigorous treatment of scattering processes is required. One such model, which explicitly solves the radiative transfer equation, is the Discrete Ordinate Method. This model has already been used to study effects of ozone and clouds on UV irradiance (*Tsay and Stamnes*, 1992). Ozone column amounts derived from it using spectral data as an input are in good agreement with those measured using Dobson spectrometers (*Stamnes et al.*, 1991; 1992). Here we investigate the performance of the model by comparing calculated results from it with clear sky spectral UV irradiances measured at Lauder, New Zealand.

2.2 UV Measurement Data

UV spectral irradiance measurements have been made from Lauder, New Zealand (45^0 S, 170^0 E, altitude 370 m), since December 1989 (*McKenzie et al.*, 1992). The spectral range covered is from 290 to 450 nm, and the spectral resolution is 1.15 nm. During clear days, a shadow band can be used to block direct radiation from the sun, so that the scattered component can be measured separately. The small correction which is applied to account for scattered radiation blocked by the shadow band is determined experimentally by measuring the reduction in signal when a region of the sky in the vicinity of the solar direction is obscured. Sequences of measurements made with the shadow band near local solar noon on several days during 1990 and 1991 were used to deduce the direct beam component as well as the scattered component. In these sequences, the shadow band measurement was interposed between two global measurements. The total time for the three

scans was approximately ten minutes, and it was assumed that the signal changed linearly with time. Near solar noon, when the solar zenith angle changes only slowly, this is a good approximation. Instrument details, including calibration procedures and an analysis of uncertainties have been described in *McKenzie et al.* (1992). For the spectral measurements presented here, the absolute accuracy is better than 10%, and relative errors are better than 5%.

The value of the Lauder data is increased by the availability of ancillary data such as ozone measurements. In addition, cloud cover is routinely logged. It is important that cloud conditions are known in comparisons with models, because one cannot assume that the highest irradiances are from cloud-free conditions. Generally, the highest irradiances are measured during partly cloudy conditions when the sun is not obscured.

For the comparison, spectral data were provided, giving cosine-weighted irradiances, output in 0.2 nm intervals, from 290 to 450 nm. Output variables included (1) the direct sun component, (2) the diffuse skylight component, and (3) the global irradiance (direct + diffuse). Excluding possible errors in the calibration standard used (a 1000 W lamp traceable to NIST), the estimated absolute uncertainty in calibrations is $\pm$ 5% (larger for $\lambda < 300$ nm).

Details of the set of measured spectra selected for this investigation are listed in Table 2.1. Ozone column measurements were available from the Dobson spectrometer at Lauder, and from the UV global irradiance ratio of 340 to 305 nm (*Stamnes et al.*, 1991). Ozone profiles measured by balloon sondes launched on the dates shown in Table 2.1 were also used. The spectra were selected to investigate sensitivities of the UV irradiance to the following parameters: (i) solar zenith

Table 2.1 Observing conditions of spectral irradiances investigated in this study. In the column labelled 'Tot Ozone (DU)', the label 'Dobs' means the total ozone abundance measured by Dobson spectrometer, and 'Deriv' means the ozone column derived from the ratio of 305 nm to 340 nm irradiance measured by the UV spectroradiometer. The column labelled 'Balloon Flight-dates' gives the closest dates of available balloon sounding data, which were used to calculate the corresponding spectra.

No	Year	Day	Date	Solar Zenith Angle (sza)	Tot Ozone(DU)		Surface Albedo	Balloon Flight-dates
					Dobs	Deriv		
1	1990	087	MAR. 28	48.0	277	260.5	0.05	MAR. 27
2	1990	182	JUL. 01	68.2	—	325.0	0.05	JUL. 02
3	1990	301	OCT. 28	32.1	341	322.5	0.05	NOV. 01
4	1990	336	DEC. 02	23.2	306	301.0	0.05	DEC. 07
5	1991	012	JAN. 12	23.3	268	270.0	0.05	JAN. 16
6	1991	069	MAR. 10	40.7	258	254.0	0.05	MAR. 11
7	1991	144	MAY. 24	65.7	291	294.5	0.05	MAY. 27
8*	1991	177	JUN. 26	68.4	343	342.5	0.90	JUN. 24
9**	1991	338	DEC. 04	22.9	310	307.0	0.05	DEC. 05

* 100% fresh snow cover on ground.

** Post-Pinatubo aerosol near 23 km.

angle (*sza*), (*ii*) ozone abundance, (*iii*) surface albedo (*e.g.* fresh snow compared with grass), (*iv*) aerosol (pre-Pinatubo versus post-Pinatubo conditions).

2.3 Model Description

In this study we have used the discrete-ordinates radiative transfer model which has been shown to be computationally efficient and reliable (*Stamnes et al.*, 1988). The model includes all orders of multiple scattering and is valid for vertically inhomogeneous media. Since the earth's atmosphere consists of a mixture of various radiatively active gases and cloud/aerosol particles that have variable mixing ratios, the optical properties (*i.e.*, single scattering albedo and phase function) vary with altitude or optical depth. To account for this inhomogeneity, we divide the atmosphere into a series of adjacent, homogeneous layers in which the scattering and absorbing properties are taken to be constant within each layer but are allowed to vary from layer to layer.

The model allows the use of an even number of discrete angular quadrature points (streams), and choices of asymmetry factor and single scattering albedo for aerosol particles. In the calculations reported here we used an asymmetry factor of 0.75 and a single scattering albedo of 0.99, and employed 8 streams which yield an accuracy in computed irradiances better than 1%. Plane-parallel geometry is assumed, which is adequate for the solar zenith angles considered. The spectral resolution of the model is 1 nm.

The extra-terrestrial solar spectrum adopted is shown in Figure 2.1a (*Nicolet*, 1989). Recent modifications to the model include corrections to the extra-

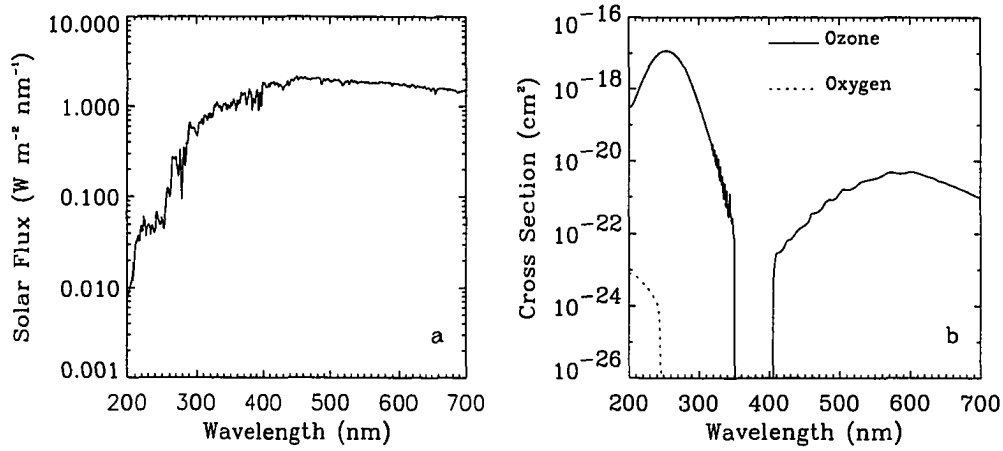

Figure 2.1 (a) Solar flux at the top of the atmosphere. (b) absorption cross section for molecular oxygen (dotted line) and ozone (solid line).

terrestrial solar spectrum in which the ellipticity of the earth's orbit about the sun is considered. In this study, we focus on cloud-free conditions for which Rayleigh scattering, gaseous absorption by ozone and oxygen, and aerosol extinction dominate the radiative transfer. The absorption cross sections for oxygen (*WMO*, 1985) and for ozone (*Molina and Molina*, 1986) are shown in Figure 2.1b.

The optical depth for ozone, for various column abundances, is shown in Figure 2.2a. Rayleigh extinction by air molecules follows a well-known analytic function (*Nicolet*, 1984). The Rayleigh optical depth is compared with aerosol optical depths in Figure 2.2b. Both ozone and Rayleigh optical depths, derived from *US Standard Atmosphere* (1976), increase rapidly towards the UV end of the spectral range. Below 320 nm, the optical depth is influenced by ozone absorption, whereas above this wavelength Rayleigh scattering dominates. The effect of aerosols is relatively small.

The specification of aerosol extinction is possible from balloon flights of backscat-

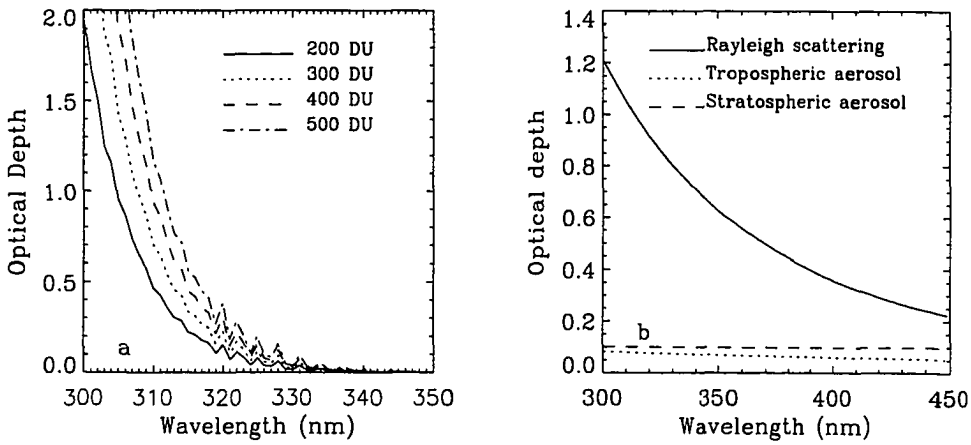

Figure 2.2 Optical depth for (a) ozone (for different column ozone abundances as indicated), (b) Rayleigh scattering, tropospheric aerosol, and stratospheric aerosol.

tersondes (*Rosen and Kjome*, 1991). Although these have been flown regularly at Lauder since February 1992, there were no flights during the period of this study. Figure 2.2b shows the estimates of aerosol optical depths (tropospheric and stratospheric) derived from a balloon flight on October 29, 1992 (day 303). The predicted stratospheric optical depth from Pinatubo aerosols present at this time is only weakly dependent on wavelength, a feature also seen in the Northern Hemisphere (*Russell et al.*, 1993) and after the El Chichon eruption (*DeLuisi et al.*, 1983). An alternative estimate of the optical depth of Pinatubo aerosol can be obtained by comparing spectral data obtained at similar *sza* and ozone amounts before and after the eruption, assuming that the tropospheric optical depth remains constant. The results of this analysis gave optical depths that were similar to those given here below 390 nm, but were 40% higher above 400 nm (*McKenzie*, 1994). Given the range of uncertainty in the wavelength dependence of Rayleigh optical depth (*Teillet*, 1990) and tropospheric aerosols, it is reasonable to assume that the relatively

small contribution of stratospheric aerosol scattering is independent of wavelength. Data from the SAGE II instrument indicate that the aerosol optical depths over Lauder on October 29, 1992 were similar to those on December 4, 1991 when spectrum 9 was obtained (*L. Thomason*, Private communication, 1993). Although the height distribution of aerosol was much lower at the later date, this would have only a minor effect. From our limited experience, the tropospheric aerosol optical depth shown in Figure 2.2b is typical. To a good approximation, this measured extinction varies with wavelength as λ^{-1}. In the following model calculations we use this tropospheric aerosol optical depth, and include the stratospheric aerosol optical depth to model the situation after the Pinatubo eruption.

2.4 Sensitivity Tests of the Model

2.4.1 Comparison of irradiances and ratios

Inputs to the model allow for specification of the atmospheric density profile, solar zenith angle, total ozone abundance and profile, cloud and aerosol layers, and surface albedo. Relevant optical scattering parameters (optical depth, single scattering albedo, and asymmetry factor) are computed layer by layer from these inputs. Although extinctions due to aerosols are uncertain, they are minimized at clean air sites such as Lauder. The measurements covered the range 290 to 450 nm, but because signal levels were generally small and the data noisy below 300 nm (except for smaller *sza*), the comparison was restricted to the range 300 to 450 nm. In the sensitivity tests that follow, we first compare calculations with the measurements

in spectrum 5 (Table 2.1). This measurement was obtained at a small *sza* before the Pinatubo eruption, on a day in which the surface albedo was low.

Figure 2.3 shows the comparison of (a) global, (b) direct, (c) diffuse, and (d) the ratio of diffuse/direct irradiance between measurement and model calculation. A surface albedo of 0.05 was used in the calculations. There is reasonable agreement between model and measurement for the diffuse and direct components. However, in the wavelength range 310 to 370 nm, the measured values are smaller than the modeled values. Although other trace gases, including NO_2 and SO_2, have absorption bands in this region, their absorptions for these observing conditions are less than 1%. The discrepancy may be due to calibration errors in the measurements or in the extra-terrestrial reference spectrum. Measurements of the solar UVA spectrum from SUSIM instrument (*Van Hoosier et al.*, 1988) also show discrepancies of this order compared with earlier ground-based estimates of solar UV (*e.g. Nicolet*, 1989). In Figure 2.3d the ratio of diffuse/direct irradiance shows very good agreement between measurement and calculation. Because the direct and the diffuse irradiance are both proportional to the extraterrestrial solar irradiance, the model calculated ratio of diffuse to direct irradiance is independent of the input solar spectrum at the top of the atmosphere. Therefore, we focus our attention on comparing ratios of diffuse to direct irradiance, which eliminates systematic error associated with the adoption of a particular solar spectrum at the top of the atmosphere, or calibration errors in the measured spectra at the surface. In these ratios, random measurement errors are more apparent. For example, a spike in the data at 306 nm is a measurement artefact, arising from noise when the gain was switched during the scan.

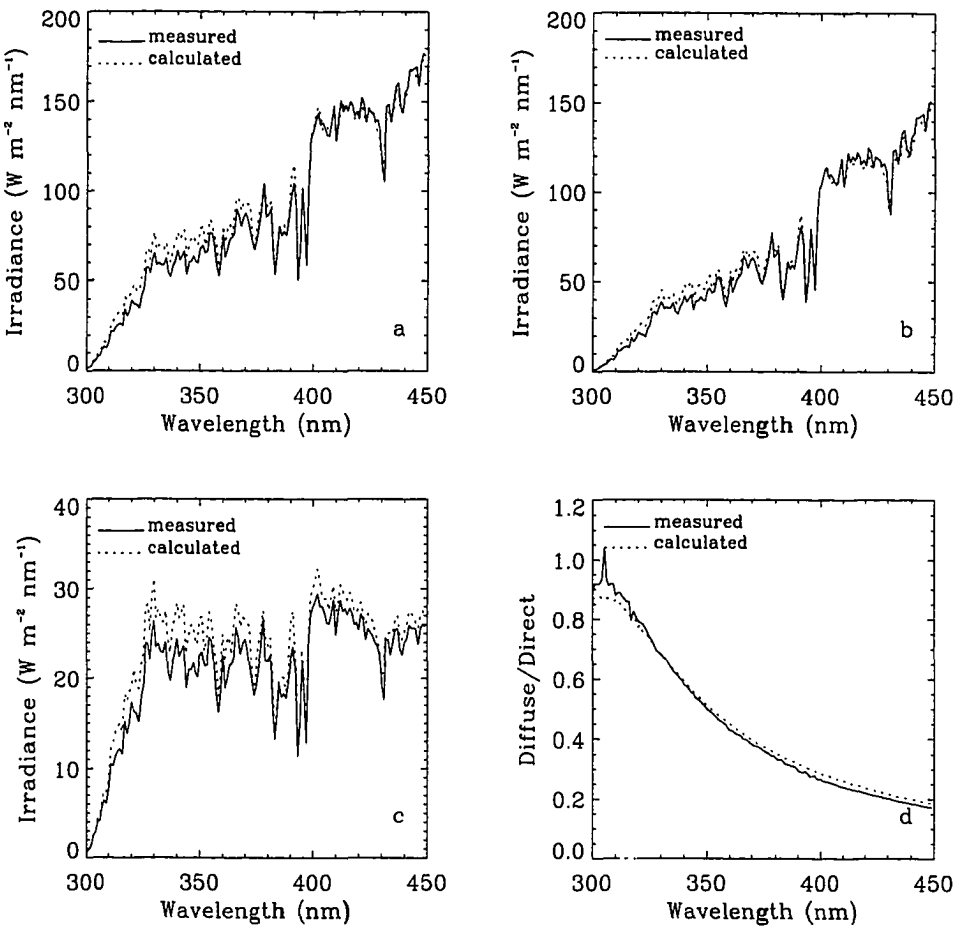

Figure 2.3 Irradiance comparison for spectrum 5 (Jan. 12, 1991): (a) global irradiance, (b) direct beam irradiance, (c) diffuse irradiance, and (d) ratio of diffuse to direct.

2.4.2 Sensitivity to solar elevation, aerosol loading, and surface albedo

Figure 2.4 shows the sensitivity of surface diffuse/direct ratios of spectrum 5 (Jan. 12, 1991) to changes in solar zenith angle, aerosol optical depth, and surface albedo (with cloud-free conditions in the three panels). In the calculations, we allowed only one parameter to vary in each panel and used the measured density profile from the balloon sounding on January 16, 1991 and a total ozone abundance of 270 DU. Although there are sometimes significant differences in total ozone abundance measured by the Dobson instrument compared with that derived from the spectroradiometer data (Table 2.1), the two methods agree well for spectrum 5. The ratio is particularly sensitive to changes in solar zenith angle (Figure 2.4a), a point previously noted in a modeling study by *Frederick et al.* (1989). For small *sza* (high sun) the ratio is smallest, but has a local maximum near 310 nm. For larger *sza* (low sun) the ratios increase, especially at shorter wavelengths.

The sensitivity of the diffuse/direct ratios to changes in tropospheric aerosol loading is shown in Figure 2.4b, where the tropospheric aerosol optical depths in Figure 2.2b have been scaled and used as inputs to the model. The surface albedo was set to 0.05. Aerosols scatter the solar UV radiation entering into the atmosphere so that they decrease the direct radiation and increase the diffuse component reaching the surface. When realistic aerosol optical depths are included, the calculated and measured diffuse/direct ratios are in good agreement.

The sensitivity of the diffuse/direct ratios to changes in the surface albedo is shown in Figure 2.4c. Surface albedo does not impact the direct beam component,

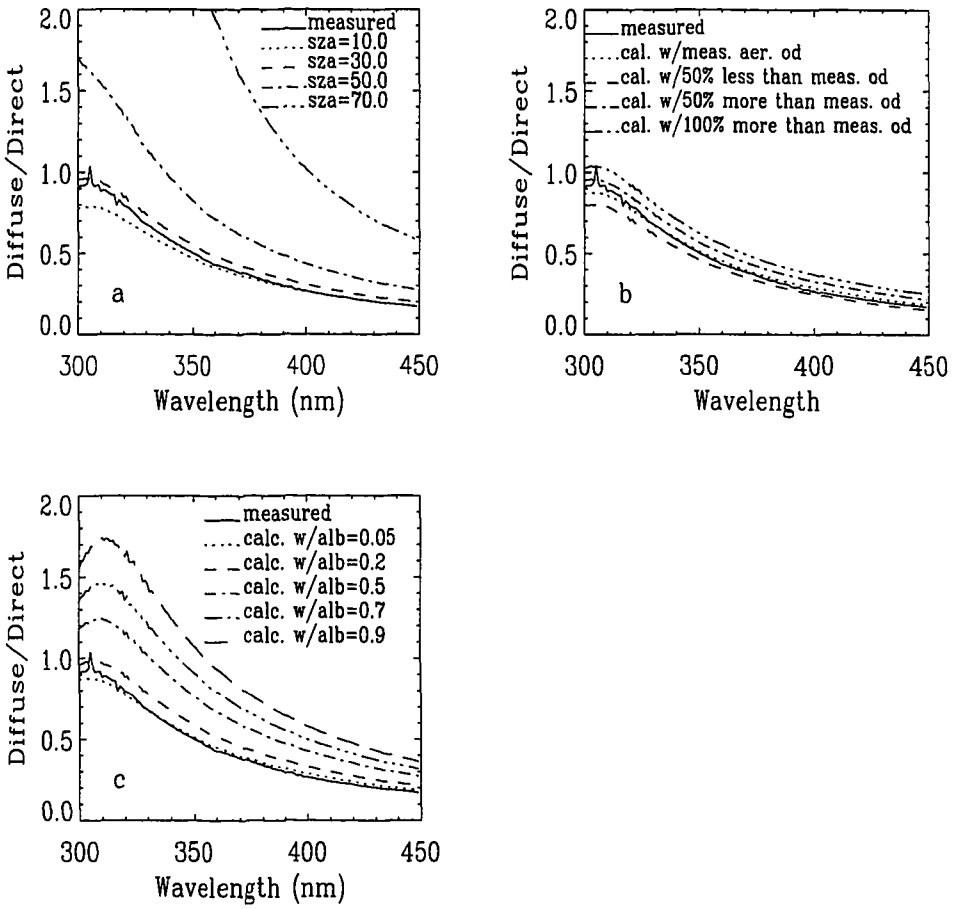

Figure 2.4 Spectrum 5 ($sza = 23.3^0$): sensitivity of diffuse/direct irradiance ratios to (a) solar zenith angle, (b) aerosol optical depth, and (c) surface albedo.

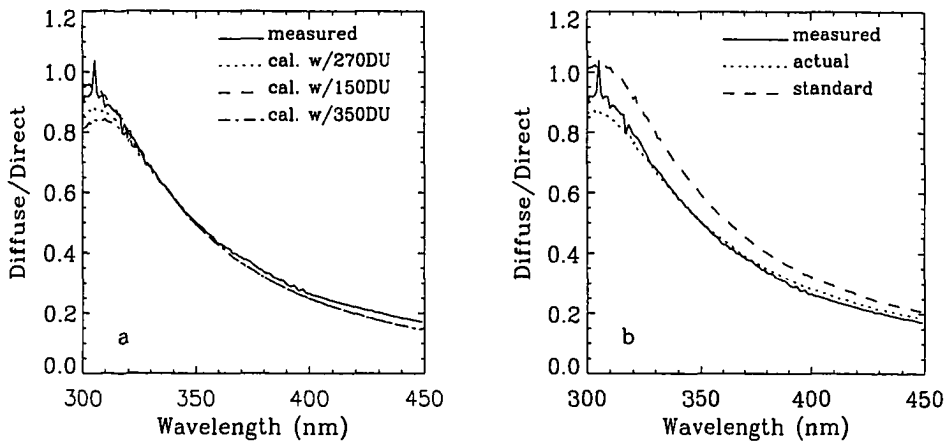

Figure 2.5 Spectrum 5: (a) sensitivity of diffuse/direct to ozone abundance (clear sky). (b) effects of density profile changes on computed spectra for aerosol loaded atmosphere and total ozone amount of 270 DU. 'Standard' refers to computation using U.S. standard atmosphere with ozone amount scaled to 270 DU, and 'actual' to computation using density profile from balloon sounding (270 DU).

but the diffuse component is increased when the surface albedo is high. The effect of surface albedo on the diffuse/direct ratios is wavelength-dependent, with maximum effects here in the range 310 to 320 nm. For the same surface albedo, the diffuse/direct ratio increases markedly at shorter wavelengths. The best agreement between model and measurement is achieved when a surface albedo of 0.05 is used. In reality, the albedo is probably wavelength-dependent, with lower albedos at shorter wavelengths.

2.4.3 Sensitivity to model atmosphere used

Changes in the penetration of solar UV-B radiation through the atmosphere are determined primarily by changes in stratospheric ozone. A reduction in ozone abundance will result in an increase of both the direct and diffuse components.

Calculated impacts of changes in ozone on diffuse/direct ratios are shown in Figure 2.5a. The effects are most apparent at wavelengths shorter than 330 nm, where ozone absorptions are largest (Figure 2.2a). The effect on diffuse/direct ratios depends on the solar zenith angle. At small *sza*, the path length through ozone is greater for the diffuse beam than for the direct beam, while the opposite is true at large *sza*. Thus, increasing the ozone column should decrease the diffuse/direct ratio at small *sza* (as in Figure 2.5a), and increase the ratio at large *sza*.

Figure 2.5b compares the measured diffuse/direct ratio for spectrum 5 (Jan. 12, 1991), with those calculated for two different assumed air density profiles. In this calculation we used the measured tropospheric optical depth shown in Figure 2.2b, and a surface albedo of 0.05. The 'actual' air density profile used data from the balloon-sounding on Jan. 16, 1991 (270 DU ozone), whereas the 'standard' air density profile used was the *US Standard Atmosphere* (1976) with the ozone abundance scaled to 270 DU. The computations show that use of the density profile from the standard atmosphere over-estimates the computed ratios. This shows that even for observation sites as low as 370 meters it is necessary to use correctly truncated air density profiles in the model calculations.

Although the profile of ozone can impact the UV irradiance at the surface (*Bruhl and Crutzen*, 1989; *Tsay and Stamnes*, 1992) the above sensitivity tests (Figure 2.5a) have shown that changes in ozone amount have only a small impact on the diffuse/direct ratios. Day-to-day changes in the density profile can impact the Rayleigh scattering optical depth significantly. At the Lauder measurement site, natural variations in atmospheric density lead to day-to-day differences in Rayleigh optical depth of $\pm$ 3%. This corresponds to an uncertainty of $\pm$ 6% in

the diffuse/direct ratios. Therefore it is necessary to use actual measured profiles of air density in these comparisons.

Uncertainty in the correct choice of asymmetry factor of the phase function used in the computation is another source of error. The diffuse/direct ratio changes by approximately 1% in the UV range for realistic changes in the asymmetry factor. Therefore, to make a rigorous comparison accurate to within a few percent, between measurements and model computations, we need to know the molecular density profile and ozone abundance, the aerosol scattering and absorption coefficients, the correct surface albedo, and the asymmetry factor of the phase function. The density profile, ozone abundance, and the aerosol optical depth can be obtained from balloon soundings, but the other factors (asymmetry factor, surface albedo, *etc*) are unknown. Differences between the measurement and the computation may therefore be caused by measurement errors, or by model errors arising from inadequate knowledge of input parameters such as the asymmetry factor and surface albedo.

Additionally, there are fundamental differences between model and measurement in the way that light scattered from the vicinity of the sun direction is interpreted. The direct-sun measurements inevitably include a contribution from forward scattered light within the effective field of view of the direct sun measurements, whereas the model calculation does not. Although this field of view is small, it may lead to important differences particularly for large air masses and for turbid conditions. The proper treatment of this error requires inputs which are not generally available.

2.5 Application of the Model to Other Spectra

In Section 2.4 we investigated the sensitivity of the model to variations in solar zenith angle, aerosol loading, surface albedo, ozone, and atmospheric profiles. We found that despite the limitations discussed at the end of Section 2.4.3, we could obtain good agreement between model and measurement using the best available input parameters.

In this section we assess the ability of the model to simulate actual measurements made over a range of different conditions, as listed in Table 2.1. For all of these spectra, atmospheric profiles of temperature, pressure, and ozone were available, within a few days of the measurement. These profiles were used in the calculations that follow.

The measurements in Table 2.1 were selected so that the model could be tested by changing only one variable at a time, while leaving all others constant.

(1) Spectrum 4 (December 2, 1990) and spectrum 5 (January 12, 1991) with similar *sza* but different ozone abundances,

(2) Spectrum 2 (July 1, 1990) and spectrum 3 (October 28, 1990) with similar ozone abundances but different *sza*.

(3) Spectrum 2 (July 1, 1990) and spectrum 8 (June 26, 1991) with similar *sza* and ozone abundances, but the latter spectrum was obtained on a day with fresh snow cover.

(4) Spectrum 4 (December 2, 1990) and spectrum 9 (December 4, 1991) with similar *sza* and ozone abundances, but the latter spectrum is after the Pinatubo eruption.

The effects of these changes are discussed in the following subsections.

2.5.1 Impact of changes in ozone abundance

Figure 2.6 illustrates the sensitivity of the diffuse/direct ratio, and the sensitivity of total irradiance (direct + diffuse), to changes in ozone abundance, by comparing spectrum 4 (Dec. 2, 1990, ozone 301 DU, $sza = 23.2^0$) with spectrum 5 (Jan. 12, 1991, 270 DU, $sza = 23.3^0$). Figure 2.6 a and c are from measurement, and Figure 2.6 b and d are from model calculation. Although the calculated ratio is not strongly dependent on ozone amount, the measured ratios do not overlap even at wavelengths longer than 330 nm. This may be caused by unmeasured differences in surface albedo and aerosol amount. The largest difference between the two measured ratios occurs for wavelengths shorter than 330 nm, where ozone influences are largest. The relative increase in total irradiance caused by the decrease of ozone abundance from 301 DU to 270 DU is 28% at 300 nm both in measurement and calculation.

2.5.2 Impact of changes in solar zenith angle

Figure 2.7 shows the effects of changes in solar zenith angle, using spectrum 2 (July 1, 1990; $sza = 68.2^0$) and spectrum 3 (Oct. 28, 1990, $sza = 32.1^0$). The two panels in this figure are similar except for measurement noise in spectrum 2 for wavelengths smaller than 360 nm, where the direct beam component is small. In the calculation of Figure 2.7b we used the same total ozone abundance of 325 DU, the same surface albedo, and the same tropospheric aerosol loading (Figure 2.2b)

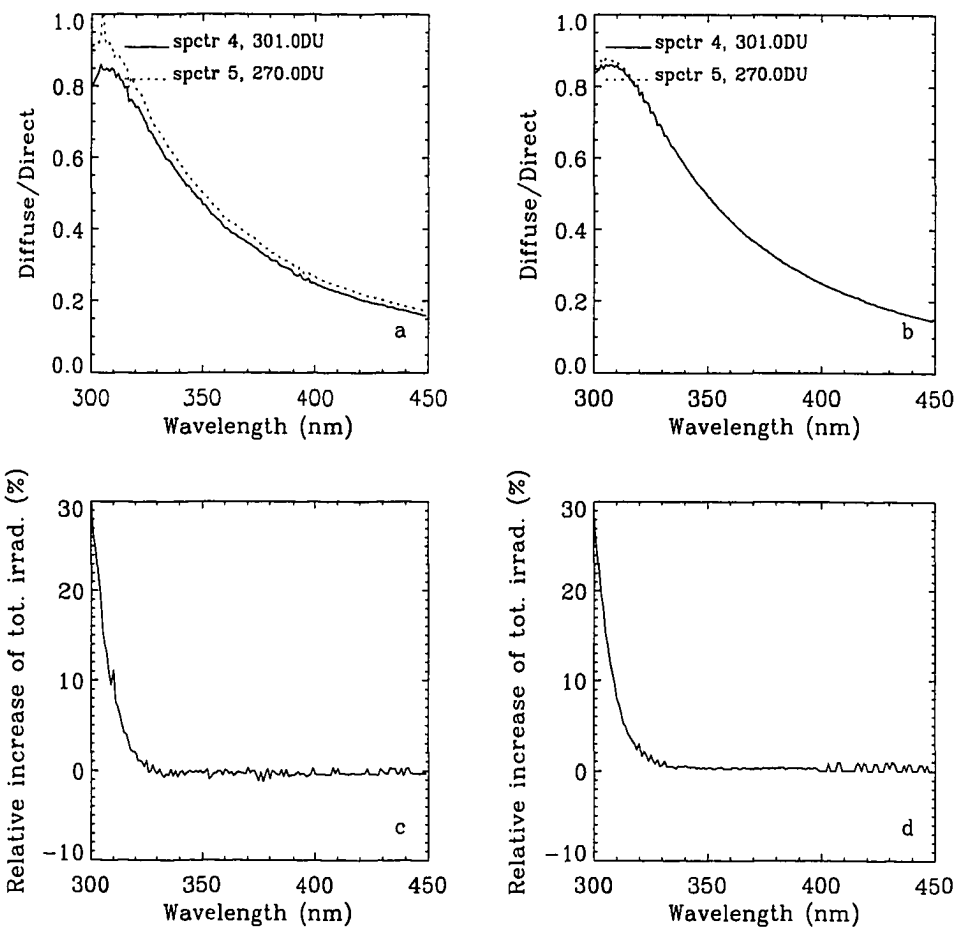

Figure 2.6 Sensitivity to changes in ozone and relative increase of total irradiance (direct + diffuse) from 301 DU to 270 DU (all other parameters are the same). Spectrum 4 (Dec. 2, 1990): $sza = 23.2^0$, total ozone content of 301 DU; spectrum 5 (Jan. 12, 1991): $sza = 23.3^0$, total ozone content of 270 DU. (a) and (c): measured. (b) and (d): calculated.

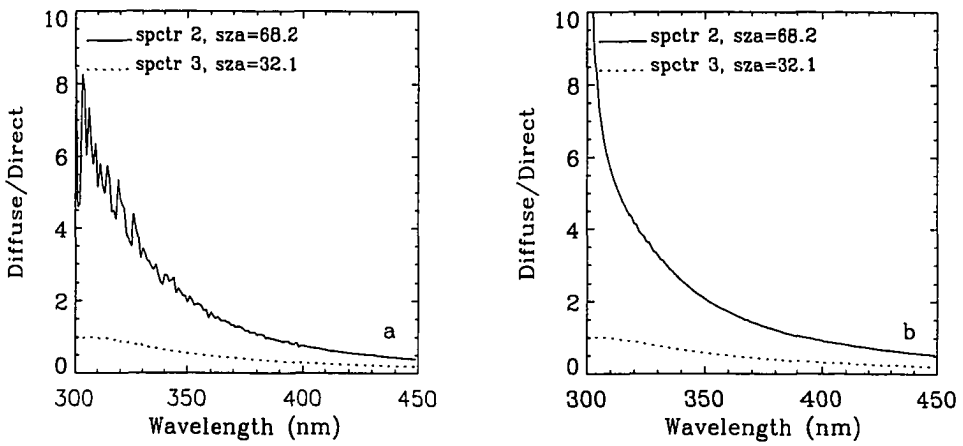

Figure 2.7 Sensitivity to changes in solar zenith angle (all other parameters are the same). Spectrum 2 (Jul. 1, 1990): $sza = 68.2^0$, total ozone content of 325 DU; spectrum 3 (Oct. 28, 1990): $sza = 32.1^0$, total ozone content of 322.5 DU. (a) measured. (b) calculated.

in both spectra. The ratio of diffuse to direct irradiance increases rapidly towards shorter wavelength for larger *sza*. We have seen in Figure 2.4a that the diffuse/direct ratio is very sensitive to solar zenith angle. The direct beam attenuated radiation and hence the source of additional diffuse radiation are proportional to $\exp(-\tau/\mu)$, where τ is the optical depth of the atmosphere and μ is the cosine of *sza*. We assumed that τ is the same on both days, so the smaller the *sza*, the greater the direct, diffuse, and hence the global irradiance through the atmosphere. The higher the sun, the more direct as compared to diffuse UV radiation will penetrate through the atmosphere. However, if the solar elevation is low enough, the radiation reaching the surface in the UVB range will be mostly diffuse (Figure 2.4a and Figure 2.7). The modeled and measured differences due to changes in solar zenith angle are in reasonable agreement, though the modeled diffuse/direct ratios are larger than those measured in spectrum 2 at the shortest wavelengths .

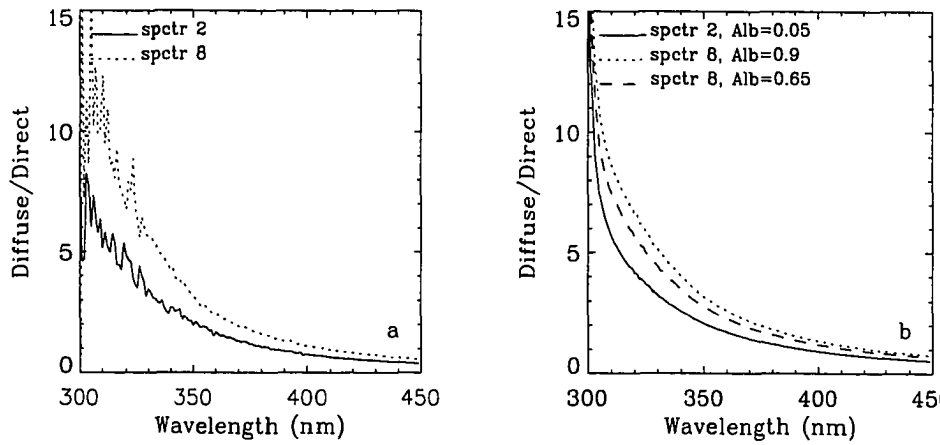

Figure 2.8 Sensitivity to changes in surface albedo (all other parameters are the same). Spectrum 2 (Jul. 1, 1990): $sza = 68.2^0$, total ozone content of 325 DU; spectrum 8 (Oct. 28, 1990): $sza = 68.4^0$, total ozone content of 342.5 DU. (a) measured. (b) calculated.

2.5.3 Impact of changes in surface albedo

Figure 2.8 illustrates the effects of changes in surface albedo for spectra obtained with similar solar zenith angle and ozone abundance. Spectrum 2 (July 1, 1990, $sza = 68.2^0$, 325 DU ozone), and spectrum 8 (June 26, 1991, $sza = 68.4^0$, 342.5 DU ozone) were obtained under similar conditions, except that there was 100% fresh snow cover when spectrum 8 was obtained. Since the surface albedo was not measured, we may use the model to find the albedo that gives the best consistency between model and measurement. We used the parameters of spectrum 8 listed in Table 2.1 and assumed a constant (wavelength-independent) surface albedo to calculate the ratio of diffuse to direct irradiance for comparison with the measurement. The best agreement between model and measurement for snow cover occurs when a large surface albedo (approximately 0.9) is used, as shown in Figure 2.10. We used a surface albedo of 0.05 for spectrum 2, and the same sza (68.2^0) and

same total ozone amount (325 DU) for both spectra, in the computation of Figure 2.8b. In both spectra the diffuse component dominates. Although the direct beam component of the solar radiation reaching the surface is similar for these two spectra, the fresh snow leads to significant increases in diffuse and thus in global UV irradiance both in measurement and calculation. For these conditions the impact of surface albedo on the diffuse component is largest at wavelengths between 310 and 370 nm (Figure 2.8). Below 340 nm, the measured ratios of diffuse to direct irradiance due to albedo changes seem larger than those calculated, while above this wavelength the opposite is true, for this choice of albedo. However, the data are noisy below this wavelength. Also shown in Figure 2.8b is the calculation for spectrum 8 with surface albedo of 0.65. The sensitivity to changing albedo for smaller *sza* has been shown in Figure 2.4c. It may be possible to obtain better agreement between measurement and model calculation by using a wavelength-dependent surface albedo.

2.5.4 Impact of changes in aerosol loading

Volcanic eruptions may inject large amounts of gases and aerosols into the stratosphere. These aerosols can modulate UV penetration through the atmosphere. Simple theory suggests that non-absorbing stratospheric aerosols will tend to decrease UV irradiances at small solar zenith angles, and increase it at large solar zenith angles (*Stamnes*, 1993). However, *Michelangeli et al.* (1992) showed that the shortest wavelength radiation reaching the surface can be increased even at small solar zenith angle by volcanic aerosol. They invoked a multiple scattering

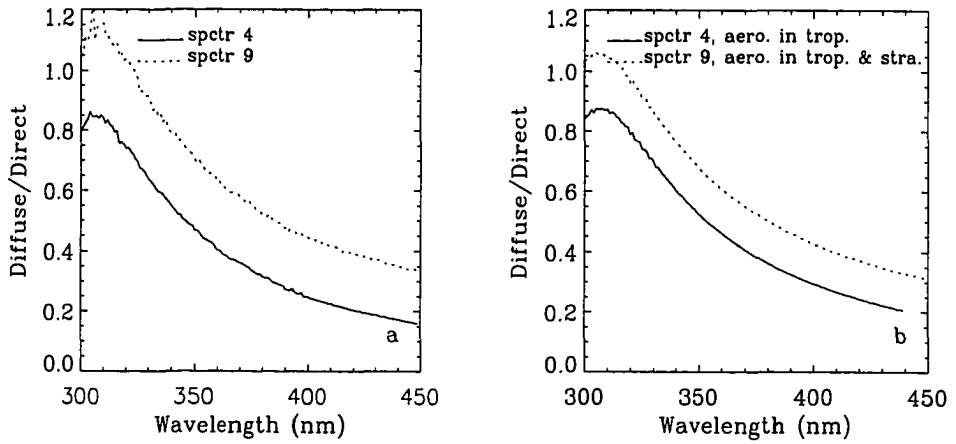

Figure 2.9 Sensitivity to changes in aerosol extinction (all other parameters are the same). Spectrum 4 (Dec. 2, 1990): $sza = 23.2^0$, total ozone content of 301 DU; spectrum 9 (Dec. 4, 1991): $sza = 22.9^0$, total ozone content of 307 DU. (a) measured. (b) calculated with tropospheric aerosols in spectrum 4 and both tropospheric and stratospheric aerosols in spectrum 9.

"photon trapping" mechanism to explain this increase, but it was later shown (*Davies*, 1993) that the relative enhancement of UV radiation reaching the surface due to scattering by stratospheric aerosols is consistent with single-scattering theory.

No changes in global irradiances due to Pinatubo aerosols have been detected in the UV measurements from Lauder. However, large changes in diffuse/direct ratios have been observed (*McKenzie*, 1994). Figure 2.9 shows the effects of Pinatubo aerosols on diffuse/direct ratios from spectra with similar solar zenith angle and ozone abundance. Spectrum 4 (Dec. 2, 1990, $sza = 23.2^0$, 301 DU ozone) is pre-Pinatubo and spectrum 9 (Dec. 4, 1991, $sza = 22.9^0$, 307 DU ozone) is post-Pinatubo. In the calculation, only tropospheric aerosols was included in spectrum 4, but both tropospheric and stratospheric aerosols were included in spectrum 9. The optical depths of aerosol are adopted from Figure 2.2b. A single scattering

albedo for stratospheric aerosol of 0.99 was used in the model calculations. Stratospheric aerosols scatter the UV, resulting in a decrease in the direct component and an increase in the diffuse component arriving at the earth surface. Measured and calculated spectra show similar sensitivities, and are consistent with our assumption that the scattering due to these stratospheric aerosols is independent of wavelength.

The good agreement between measurement and model for an assumed single-scattering albedo of 0.99 also supports other evidence that scattering by the volcanic aerosols dominates over absorption, and that its optical depth was close to 0.1 (*McKenzie*, 1994). The net change in global irradiance due to the aerosols was small, and their main effect was to redistribute energy out of the direct beam into the diffuse component.

2.6 Model versus Measurement Comparisons for All Spectra

Here we show comparisons between the model calculations and measurements for all spectra listed in Table 2.1. A surface albedo of 0.05 was used in the calculations of all spectra in Figure 2.10 except for spectrum 8 in which 0.9 was used. Tropospherical aerosol optical depths shown in Figure 2.2b were used in the calculations of all spectra. Real day-to-day differences in albedo and optical depth are expected, and further improvements in the agreement between measurement and computation could be achieved by scaling these parameters. The effect of

stratospheric aerosol (Figure 2.2b) was also included for spectrum 9. The measured and calculated diffuse/direct ratios are compared in Figure 2.10. The solar zenith angle, total ozone abundance, surface albedo, and the corresponding balloon sounding profiles used in the calculations are listed Table 2.1.

There is generally good agreement between measurement and models. A persistent feature is the tendency for steeper slopes in the measurements at short wavelengths.

Major uncertainties in the comparisons of model and measurement arise from lack of detailed information about day-to-day changes of surface albedo and aerosol loading in the atmosphere. Accurate parameterizations of aerosol optical properties (including asymmetry factor) and surface albedo are required to adequately model UV irradiances.

We note that by using ozone columns derived from the spectral measurements rather than from Dobson measurements, the modeled irradiances are not totally independent of the measured irradiances. Although there are sometimes significant differences (*e.g.* spectrum 1), Dobson data are not always available. In Section 2.5.1 it was demonstrated that although ozone changes modulate the UV reaching the surface, the impact on diffuse/direct ratios is minor.

Figure 2.11 presents a more detailed optimal comparison between measurements and model computations for spectrum 5 (Jan. 12 1991, before Pinatubo) and spectrum 9 (Dec. 4, 1991, post Pinatubo), in which deviations between measured and computed results are also shown. A surface albedo of 0.05 was used in the calculation of spectrum 5 and 0.06 in spectrum 9 to obtain best agreement between modeled and measured spectrum, and the aerosol optical depths are adopted from

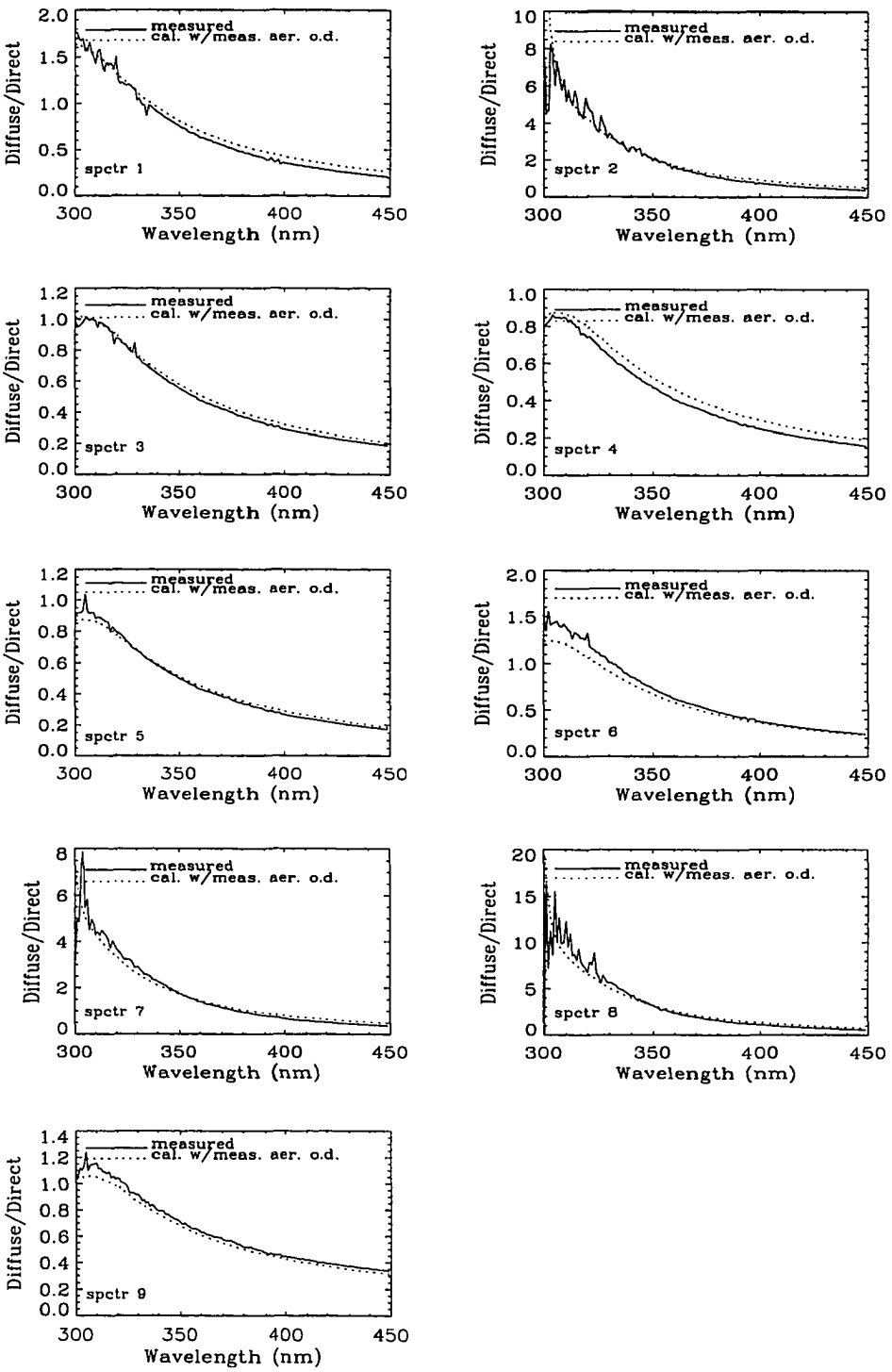

Figure 2.10 Comparison between measured diffuse/direct ratios and calculated ratios given the ozone column, solar zenith angles, surface albedo, and realistic aerosol for all spectra. Note the changes of scale in the y-axes between panels.

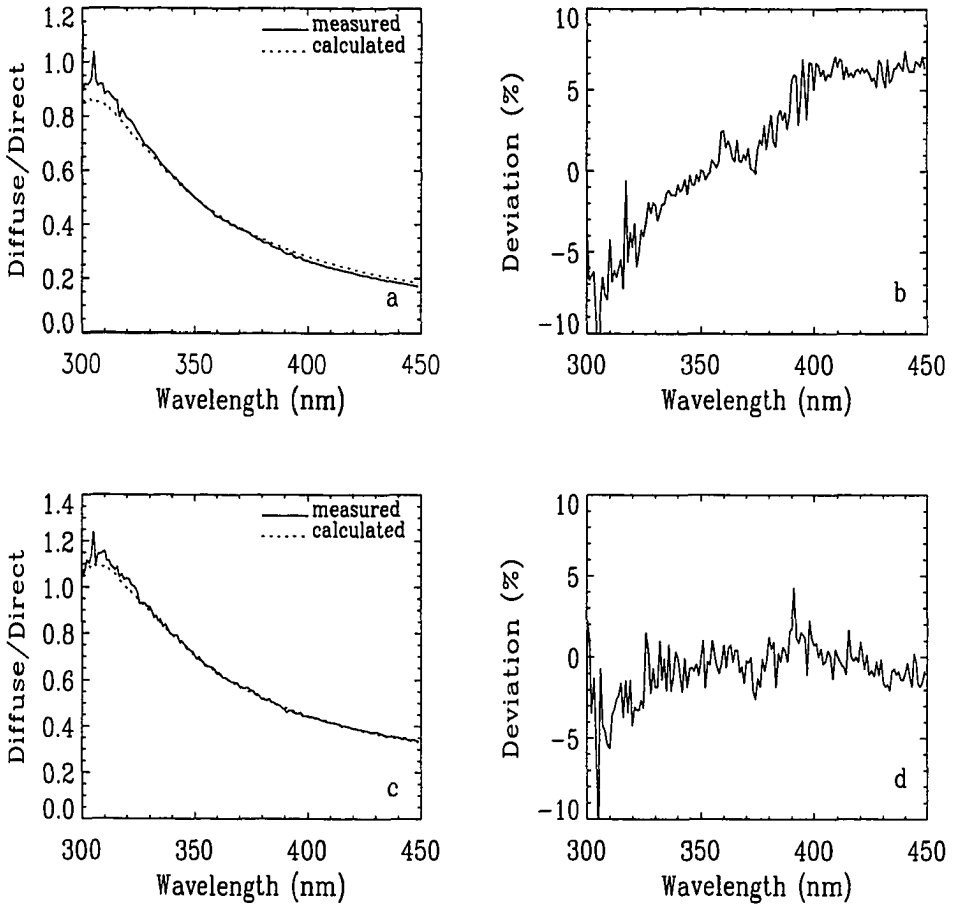

Figure 2.11 Comparison of measurements and model calculations. Tropospheric aerosols are involved in the calculation of spectrum 5; both tropospheric and stratospheric aerosols in spectrum 9. (a) diffuse/direct (spectrum 5), (b) deviation between model and measurement (spectrum 5), (c) diffuse/direct (spectrum 9), and (d) deviation between model and measurement (spectrum 9).

Figure 2.2b. Both stratospheric and tropospheric aerosols are considered in the calculation for spectrum 9 which is after the eruption of Pinatubo, and only tropospheric aerosols for spectrum 5. The deviation of diffuse/direct ratio between measurement and model calculation is less than 8% in the UVB range between 300 and 320 nm if obvious noise in the measurement data is ignored. For longer wavelengths from 320 to 450 nm the deviation is even smaller. These differences are comparable with, but slightly larger than the estimated measurement errors for individual measurements. Since the ratios are formed from combinations of measurements, the difference is reasonable.

2.7 Summary of the Chapter

In this chapter we used an accurate radiative transfer model for a vertically inhomogeneous atmospheres with all orders of multiple scattering to compare the computed UV irradiances with clear-sky measurements made in Lauder, New Zealand. These comparisons included sensitivity tests to changes in solar zenith angle, ozone abundance, aerosol loading, and ground albedo.

There is reasonable agreement between model and measurement for the global, diffuse and direct components of UV irradiance. However, in the wavelength range 330 to 370 nm, the measured values are smaller than the modeled values. This discrepancy maybe due to calibration errors either in the measurements or in the extraterrestrial reference spectrum. Better accuracy in measurements is required, including measurements of the extraterrestrial solar spectrum.

Diffuse/direct ratios are insensitive to these calibration errors, but still provide

a sensitive method of evaluating model performance. The ratios are relatively insensitive to ozone changes, but depend critically on solar zenith angle, surface albedo and aerosol extinction.

It is important to use actual profiles of temperature, pressure, and ozone rather than standard profiles in these comparisons. When this was done, we found good agreement between measured and calculated ratios over a wide range of observing conditions.

The poorer agreement in some spectra (*e.g.* spectra 4 and 6) probably results from uncertainties in parameterizing aerosol and surface albedo effects. The choice of molecular density profiles, and the asymmetry factor for the aerosol phase function can also cause discrepancies between model results and measurements. This highlights a need for a wide range of ancillary measurements before models can be validated effectively against measurements.

When the model is optimized to the measurements, with reasonable choices of free input parameters, and using measured profiles, the deviation between calculated and measured diffuse/direct ratios can be as small as 8% in the UVB region, and approximately 4% at longer wavelengths. This difference is comparable with, but slightly larger than the uncertainty in the measurements.

The Pinatubo study gave results consistent with the assumption that aerosols present in December 1991 had a high single scattering albedo, and had an optical depth of approximately 0.1, which was independent of wavelength over the range considered.

Increases in surface albedo due to fresh snow led to significant increases in the diffuse UV and global UV irradiances both in the measurements and in the

model calculations. Best agreement between model and measurement for the snow-covered surface was obtained for a surface albedo of 0.9. However, the surface albedo in the wavelength range of 300-450 nm is probably wavelength-dependent, with lower albedos at shorter wavelengths.

Chapter 3

Comparative Study of the Antarctic and Arctic UV Radiation Environment and the Impact of Clouds

3.1 Introduction

Radiative transfer of ultraviolet light in the polar regions is characterized by (1) low sun elevations and long optical paths through the absorbing ozone layer; (2) snow and ice coverage that characterizes the surface albedo; (3) unique cloud climatology, specifically the extensive low-level stratiform clouds; (4) occurrence of widespread, removal-resistant aerosols (especially in the Arctic) which scatter and absorb sunlight; and (5) large seasonal variability in the incident radiation.

The combined role of clouds and surface reflection is particularly important at high latitudes where the radiative effects are enhanced by multiple reflections of photons between the highly reflecting surface and the cloud base. In the Arctic the presence of haze in the spring may significantly modify UV penetration.

The United States National Science Foundation established an ultraviolet monitoring system in Antarctica beginning in 1988, responding to the serious ozone depletion reported in Antarctica (*Farman et al.*, 1985). In December 1990, a fifth instrument was installed at Barrow, Alaska. The network is the first automated, high resolution UV scanning spectroradiometer network installed in the world. The purpose of this program is to make hourly measurements of spectral ultraviolet radiation when the sun is above the horizon at five measurement sites: South Pole, McMurdo, and Palmer Station (in Antarctica); Ushuaia (at the southern tip of Argentina); and Barrow (in Alaska). Table 3.1 shows their latitude, longitude, and installation time. This effort provides a unique data base on ultraviolet radiation levels in Antarctica and the Arctic. These data allow us to investigate the temporal and spatial evolution of ultraviolet radiation in the polar regions.

We analyzed the data at each measurement site since it was established to investigate the time evolution and latitudinal changes of the UV radiation environments in the northern and southern polar regions.

3.2 Total Ozone Abundance

We utilized ground-based measured global (direct + diffuse) irradiances at two near UV wavelengths, one that is appreciably absorbed by ozone (we used 305 nm here),

Table 3.1 Longitude and latitude of the five measurement sites and their installation time. 'Noon (GMT)' is the approximated local noon in Greenwich Mean Time for each site that used in the comparison.

No	Site	Longitude	Latitude	Noon (GMT)	Eatablished
1	Barrow, Alaska	156.47 W	71.18 N	22	Dec. 1990
2	Ushuaia, Argentina	68.19 W	54.49 S	17	Nov. 1988
3	Palmer, Antarctica	64.03 W	64.46 S	16	May 1988
4	McMurdo, Antarctica	166.40 E	77.51 S	1	Mar. 1988
5	South Pole, Antarctica	0	90.00 S	12	Feb. 1988

the other that is not (we used 340 nm here), to derive column ozone abundance by comparison with synthetic values of this ratio generated by the radiative transfer model described in Section 2.3, which includes the multiple scattering and ground reflection, for a variety of ozone abundances. This method is insensitive to cloud cover and surface albedo used in the model calculations. The detailed procedure for the derivation was described by *Stamnes et al.* (1991).

Figure 3.1 to 3.5 present the derived column ozone abundance at local noon compared with the Total Ozone Mapping Spectrometer (TOMS) for Barrow, Ushuaia, Palmer, McMurdo, and South Pole Station from the year the measurement site was established. We found that there was an ozone 'hole' in Antarctica each spring in the data. It was most obviously seen at South Pole Station. Ozone depletion was not clear at Ushuaia. In contrast to the ozone 'hole' in Antarctica, total ozone abundance was consistently high in the spring at Barrow; the low value of total column ozone occurred in the summer.

The total ozone abundances given by the two methods are similar but not iden-

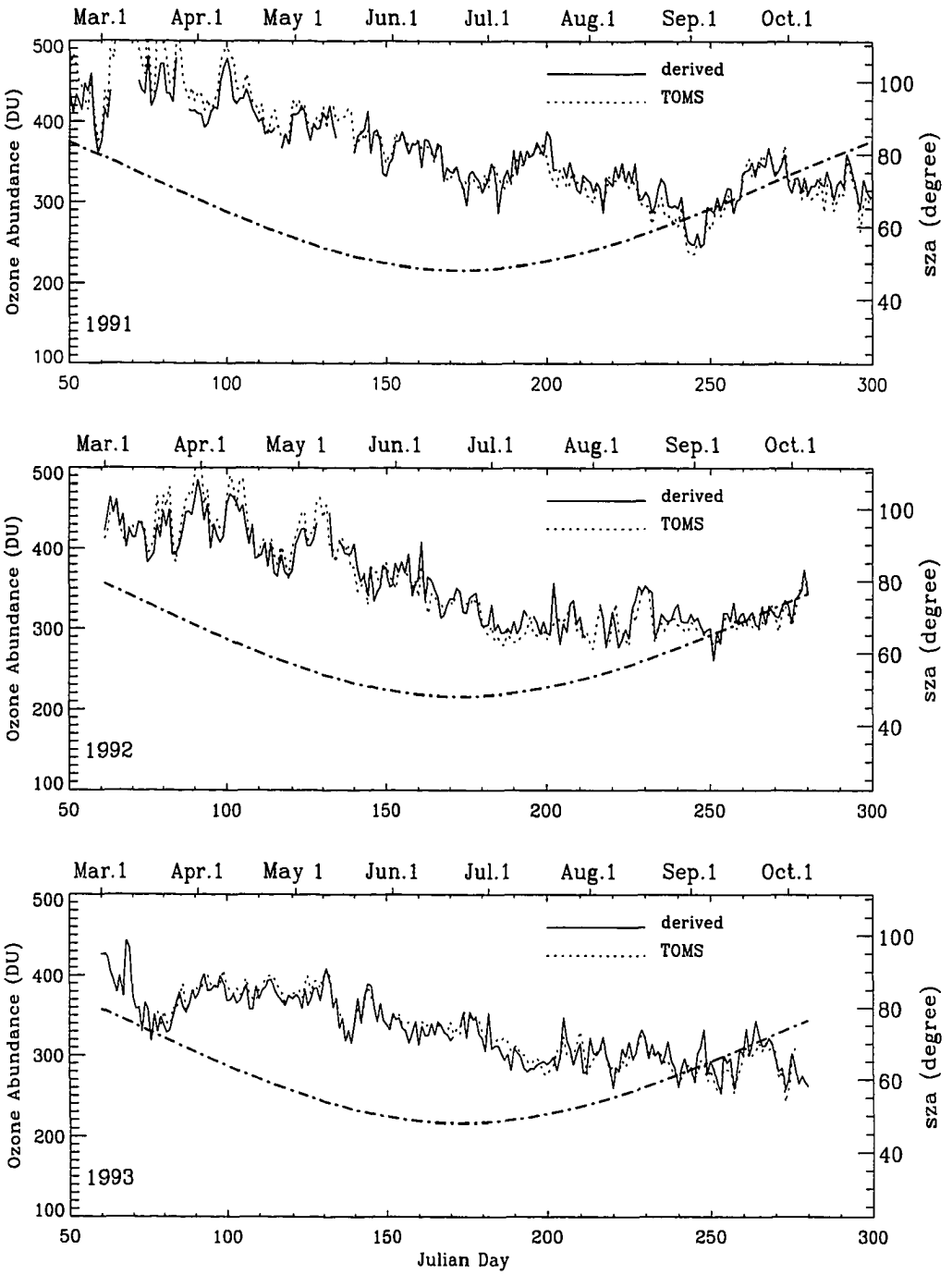

Figure 3.1 Time history of total ozone abundance derived from ground-based measurement (solid lines) compared with TOMS (dotted lines) at Barrow, Alaska in (a) 1991, (b) 1992, and (c) 1993. The breaks appear in these curves when data are unavailable. Dash-dotted lines are the corresponding solar zenith angles (*sza*).

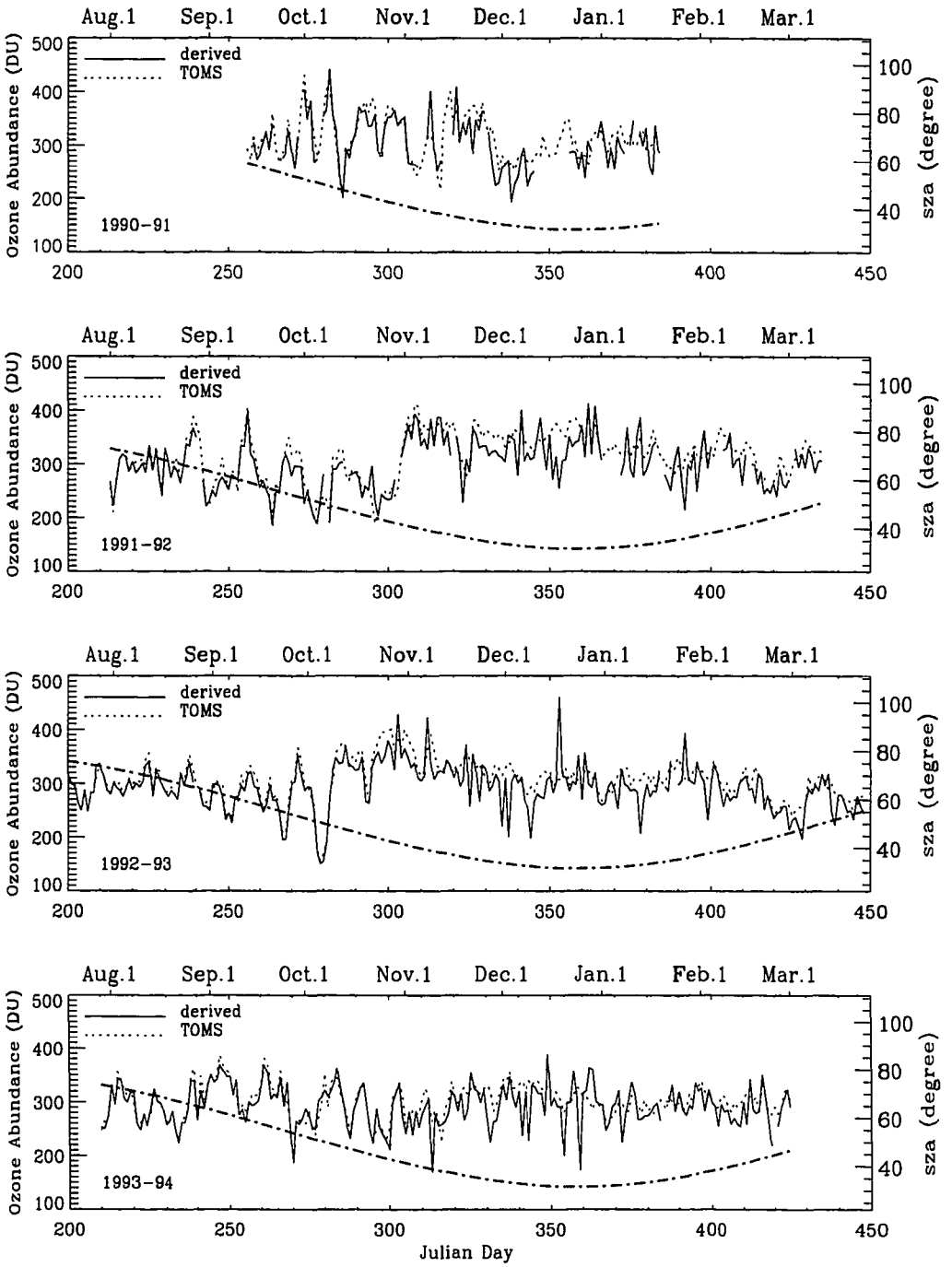

Figure 3.2 As Figure 3.1 but for Ushuaia, Argentina in (a) 1990-91, (b) 1991-92, (c) 1992-93, and (d) 1993-94.

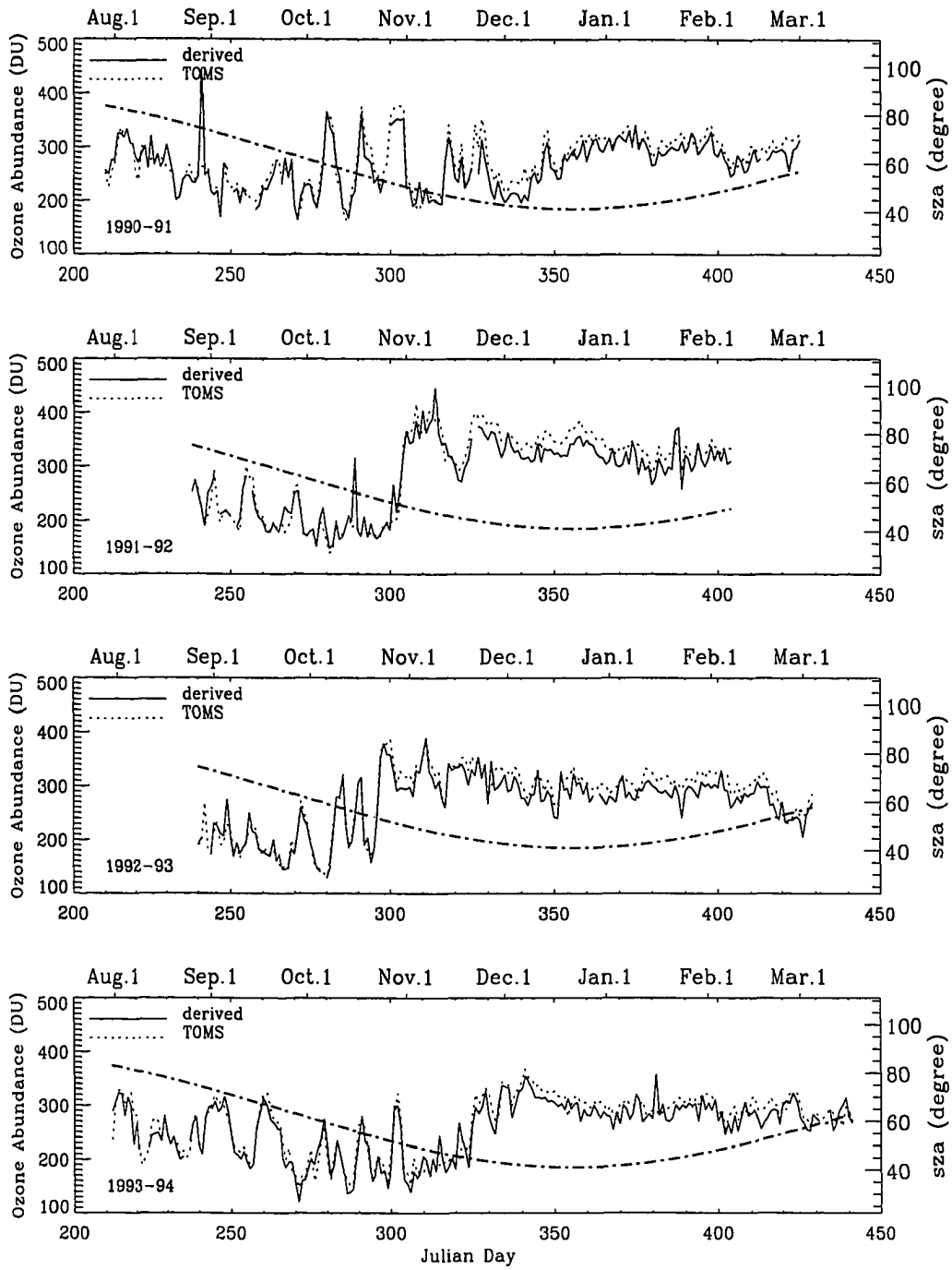

Figure 3.3 As Figure 3.1 but for Palmer Station in (a) 1990-91, (b) 1991-92, (c) 1992-93, and (d) 1993-94.

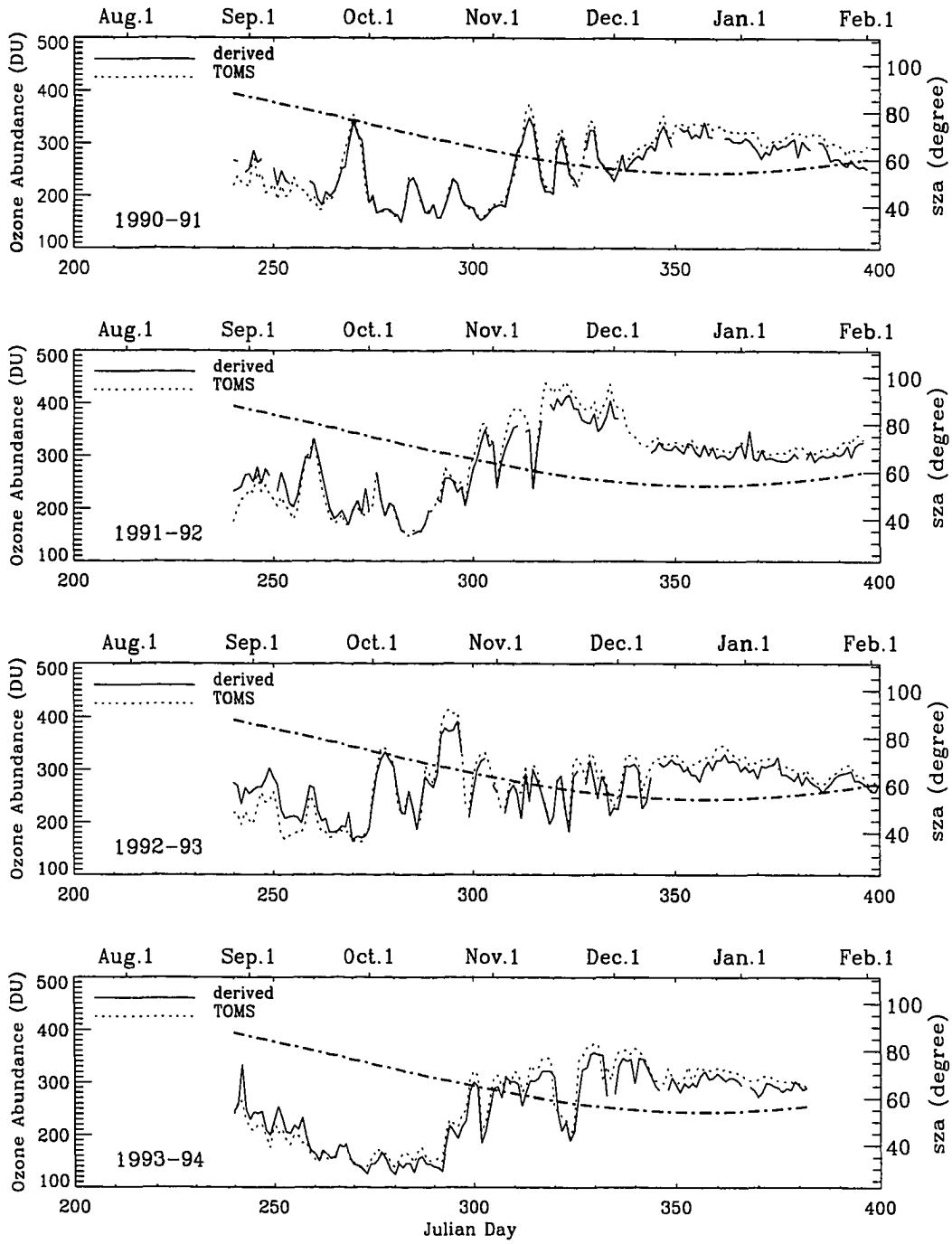

Figure 3.4 As Figure 3.1 but for McMurdo Station in (a) 1990-91, (b) 1991-92, (c) 1992-93, and (d) 1993-94.

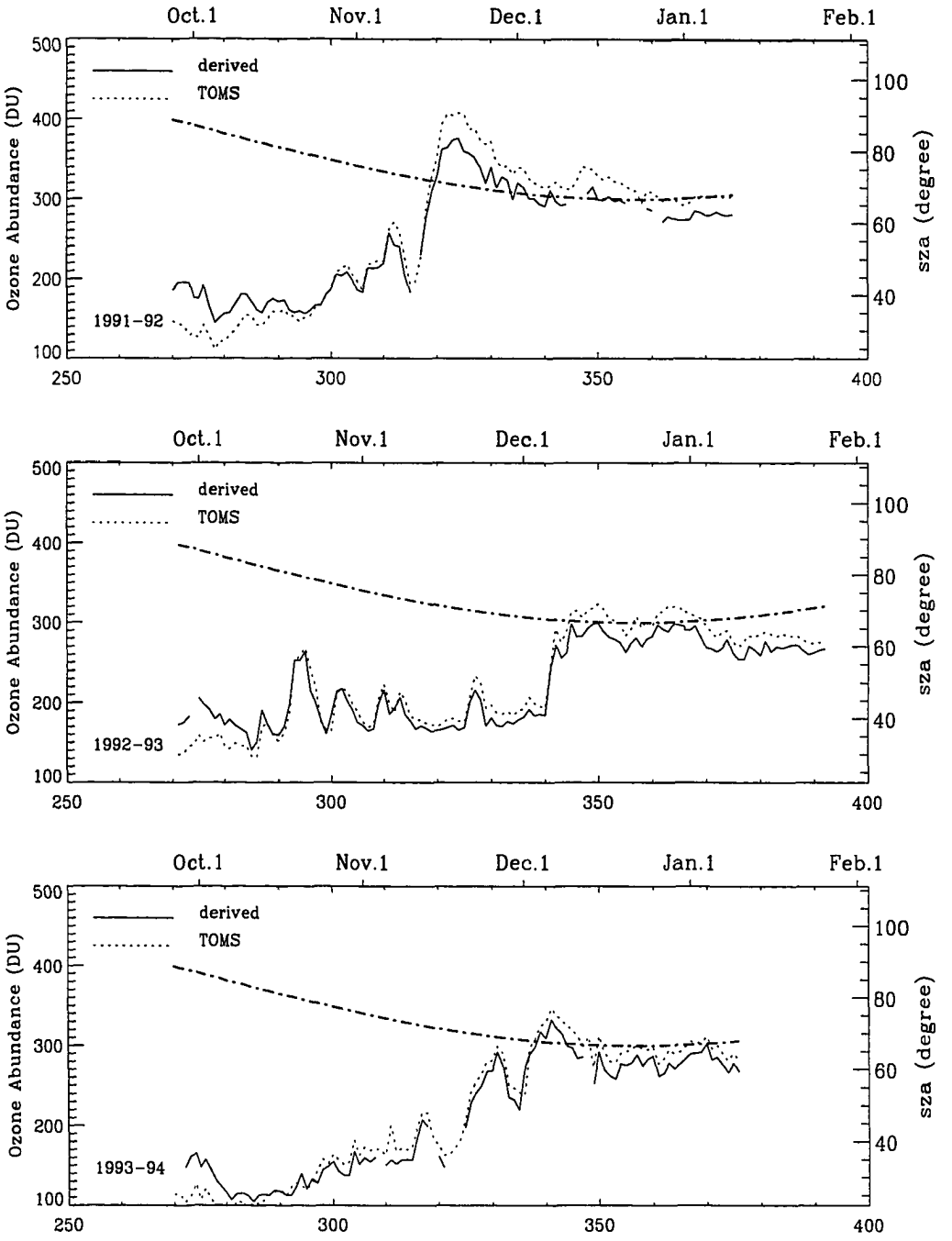

Figure 3.5 As Figure 3.1 but for South Pole Station in (a) 1991-92, (b) 1992-93, and (c) 1993-94.

tical except for some limited periods. We note that there is a systematic difference between the two results in each plot, which depends on latitude. In Antarctica (South Pole, McMurdo, and Palmer Station), the ozone abundance is relatively low and steady during austral spring; the amount derived from our method agrees well with TOMS during this period. In the winter our method overestimates ozone, but underestimates it in the summer. At Ushuaia, our estimation agrees reasonably with TOMS in late austral winter, but tends to underestimate ozone abundance in the spring and summer. In the Arctic (Barrow), our method underestimates total ozone abundance before summer solstice, but overestimates it hereafter.

The daily total column ozone tends to be more stable (not as many spikes) closer to South Pole because of dynamical stability of the atmosphere. Examining Figure 3.1 to 3.5 more closely, it can be seen the derived column ozone contains more spikes than TOMS data, especially at Ushuaia, Palmer, and Barrow. We should note that the TOMS data represent a daily average over an area of 22,500 km^2, while the column ozones from our method were derived from measurements made at local noon. However, there are some possibilities that may give rise to spikes and the systematic differences.

3.2.1 Effects of random variability on cloud thickness

A more likely cause for the spikes is that the UV spectrometer measurements we used at these two wavelengths, were collected at two different times and thus the solar zenith angle and cloud optical thickness might have changed during the course of the scans. The maximum duration of scan time for the wavelength range

280 to 315 nm (spectral range 1, hereafter referred to as *SR 1*) was 2 minutes and 15 seconds with resolution of 0.2 nm, whereas the maximum scan time for the wavelength range 280 to 380 nm (spectral range 2, hereafter referred to as *SR 2*) was 2 minutes and 45 seconds with resolution of 0.5 nm. The time between the 305 nm measurement during the *SR 1* highest resolution scan and the 340 nm measurements during the *SR 2* medium resolution scan would be about 4.5 minutes. The maximum change in solar zenith angle for the time interval between the 305 and 340 nm observations for noontime data at Palmer Station is less than 0.1^0. Changes of solar zenith angle on the order of 0.03 may be frequent and will be of different sign depending upon when during the year it occurred. However, this may be considered to be in the noise level (*C. R. Booth*, private communication, 1994). It was usually cloudy at Ushuaia, Palmer, and Barrow, and there were relatively fewer cloudy sky conditions at South Pole and McMurdo Station, as we will see in the next section. The cloud thickness over the measurement sites might have changed during the 4.5 minute period between scans. It may be worthwhile to use two measurements from the same scan to minimize the effect of cloud as follows.

To examine the effects of random variability of cloud optical thickness during the highest spectral resolution scan (*SR 1*) and the medium resolution scan (*SR 2*), we use the ratio of global irradiance measurements at 313.5 nm and 300 nm, both extracted from *SR 1*, and the ratio of 340 nm to 320 nm, both extracted from *SR 2*, to derive ozone content at Palmer Station in 1992-93 season. For comparison we also show the derived total ozone from the ratio of measurements at 320 nm (from *SR 2*) and 305 nm (from *SR 1*) and that at 340 nm (*SR 2*) and 305 nm (*SR 1*).

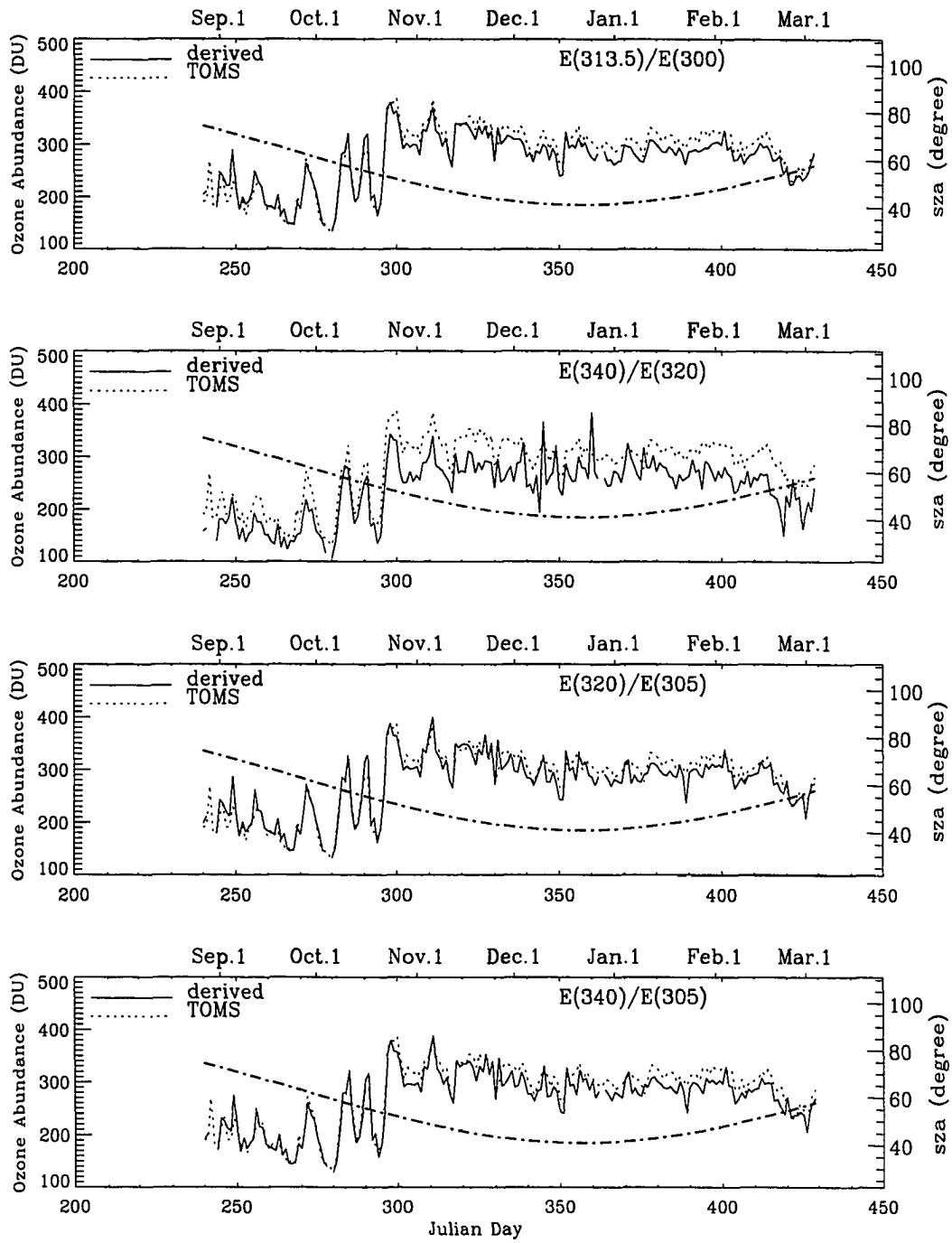

Figure 3.6 Derived total ozone abundance (solid lines) by using different pairs of measured global irradiance ratio at selected wavelengths compared with TOMS (dotted lines) at Palmer Station in 1992-93 season. (a) for the ratio at 313.5 nm and 300 nm, (b) for the ratio at 340 nm and 320 nm, (c) for the ratio at 320 nm and 305 nm, and (d) for the ratio at 340 nm and 305 nm.

Figure 3.6 shows the derived column ozone by using different pairs of measured irradiance ratios compared with TOMS. *Lubin and Frederick* (1990) have used the irradiance ratio at 300 nm and 313.5 nm to estimate ozone abundance. Because the finest resolution of our model is 1 nm in an integer interval, we calculated the irradiance at 313 nm in place of the irradiance at 313.5 nm, which is provided by the NSF/UV data, for comparison as an approximation. From this plot (Figure 3.6a) we can see that the strong spikes in the derived column ozone have been greatly reduced when the irradiance ratio of 313.5 nm to 300 nm was used. However, errors may have been introduced by using the modeled irradiance of 313 nm instead of 313.5 nm to derive the column ozone. On the other hand, the agreement between TOMS and derived column ozone from the irradiance ratio of 340 nm to 320 nm (Figure 3.6b) is worse even though both the irradiance measurements are from the same scan. There is better agreement between TOMS and derived column ozone using the measured irradiance ratio of 320 nm to 305 nm (Figure 3.6c), if the small spikes in the derived ozone can be ignored which may be caused by the random variability of cloud optical thickness during the two different resolution scans. In summary, we may use the measured irradiances at two wavelengths shorter than 340 nm with a narrow interval between them, but they should preferably come from the same spectral scan, to derive reliable column ozone abundance. This requires reprocessing of the original measurement data; we have asked for such data from Biospherical Instruments, Inc.

3.2.2 Effects of errors during measurements

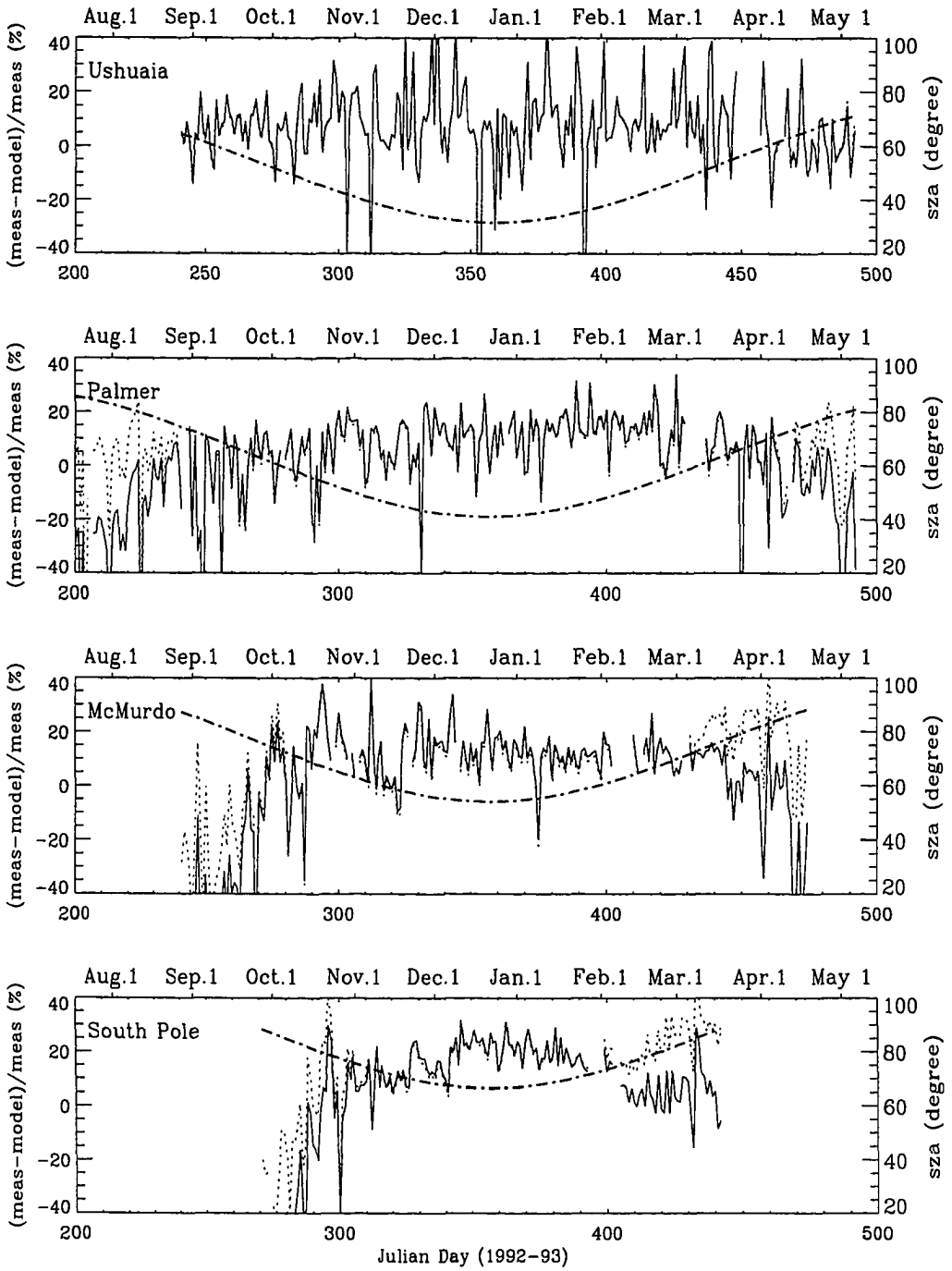

Figure 3.7 Percentage changes of measured irradiance at 305 nm required to achieve correct derivation of total ozone abundance relative to the measured irradiance at 340 nm at the four measurement sites in Antarctica from 1992 to 1993. The solid lines were calculated by the assumption of plane-parallel atmosphere, the dotted lines including the effects of spherical geometry. The dash-dotted lines are the corresponding solar zenith angles.

Although the agreement between derived column ozone and TOMS is better when the irradiance measurements at two different wavelengths are properly chosen, our method underestimates ozone in the summer and overestimates it in the winter in Antarctica as compared to the TOMS inferences producing a systematic difference. *Smith et al.* (1992a) indicated that varying the irradiance ratio by 10% would lead to a difference in column ozone as large as 16 DU because of possible errors in the measurement data. It is useful to see the level of changes required in measured irradiance at 305 nm relative to that at 340 nm to align the derived column ozone with the TOMS data. Figure 3.7 shows the percentage changes of measured irradiance at 305 nm required to correctly derive column ozone (*i.e.* the same as TOMS), assuming that the 340 nm irradiance measurement was reasonably accurate at the four measurement sites in Antarctica at local noon during 1992 to 1993, when we had the sun above horizon. The solid lines were calculated by assuming plane-parallel approximation; the dotted lines include a correction for the effects of spherical geometry (*Kylling and Stamnes*, 1992; *Dahlback and Stamnes*, 1991) in the model computations. The dash-dotted lines are the corresponding solar zenith angles. In general, we must account for the effects of spherical geometry when solar zenith angles are greater than 70 degrees. The calculations clearly show that the low values of 305 nm irradiance (solid lines) required for alignment with TOMS at high solar zenith angles (greater than 70 degree) are caused by the assumption of plane-parallel geometry. These errors can be improved by the use of spherical corrections (dotted lines).

There is a persistent bias of around 5 - 15% higher readings in 305 nm irradiance at Ushuaia, Palmer, and McMurdo Station, and 5 - 25% higher at South Pole Sta-

tion than expected. This bias may be partly introduced during the measurement. As the solar spectra increases in steepness as shorter wavelengths are approached (below 305 nm), a measurement with finite bandwidth will produce higher readings than are actually present. Although the bandwidth of the measurements 0.7 nm has been reported, some evidence indicates that it is actually wider, perhaps 1 nm (*C.R. Booth*, private communication, 1995). However, the bias introduced by this mechanism should be the same on a site-by-site basis. There must be some other reasons for the disagreement.

3.2.3 Effects of spherical geometry

The small differences between the plane-parallel model (solid lines) and spherical geometry model (dotted lines) run at low solar zenith angles (Figure 3.7) are due to the usage of different precisions and model atmospheres in the model computations. We used single precision and 33 layers of subarctic summer US Standard Atmosphere (1976) in the plane-parallel assumption model run, and double precision and 100 layers of subarctic summer atmosphere (*Anderson et al.*, 1987) in the spherical geometry model.

We note that the signs and values of the required 305 nm irradiance readings at McMurdo and South Pole Station are not symmetrical about antarctic summer solstice even after the inclusion of the effect of spherical geometry.

We used a more precise radiative transfer model which properly treats the effects of spherical geometry to derive again the column ozone and compared it with TOMS at McMurdo Station in 1992-93 season (Figure 3.8). The differences of

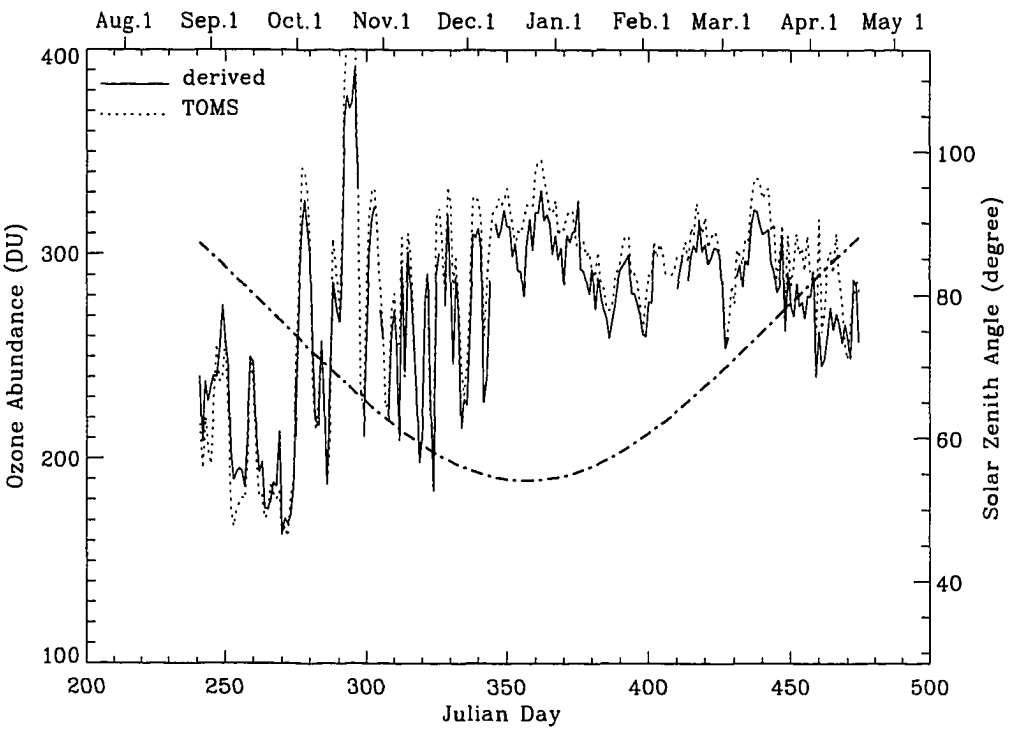

Figure 3.8 Total ozone abundance derived from ground-based irradiance measurements at 305 and 340 nm by using a radiative transfer model including the effect of spherical geometry (solid line) compared with TOMS (dotted line) at McMurdo Station in 1992-93. Dash-dotted line is the corresponding solar zenith angle.

total ozone between the two methods decrease when solar zenith angle greater than 70^0 compared with Figure 3.4 in the corresponding year. However, our method still overestimates total ozone in the winter and underestimates it in the summer. Hence, the atmosphere spherical effect does not appear to be the reason for the systematic difference.

3.2.4 Effects of other uncertainties

It is known that the ozone absorption is temperature-dependent, and therefore any model used for ozone estimation will give an error whenever the actual temperature profile significantly differs from the temperature profile used in algorithm development. Simultaneous measurements with TOVS/HIRS2 and ozonesonde at Palmer Station during the formation of the 1987 'ozone hole' showed that the TOMS algorithm tends to underestimate the ozone content in late winter because of low stratospheric temperatures (*Fefèvre et al.*, 1991). *Smith et al.* (1992a) claimed that the variations of derived column ozone using the ground-based irradiance measurements ratio at 308 and 332 nm are within 5 DU if the atmospheric temperature changes are less than $30^0 K$.

We have used the subarctic summer climatological vertical profile in all the derivations of column ozone. In reality the temperature profiles in Antarctica may significantly differ from the subarctic summer climatology and also change from site to site. We may use more reasonable temperature estimates in the derivations, at least similar to those used in the TOMS algorithm, if we assume TOMS are correct. We say reasonable estimates because to date there have been no operational

simultaneous data with respect to atmospheric temperature profiles when the solar irradiance measurements were taken.

On the other hand, the reliability of TOMS data must be checked. The TOMS sensors may have solar angle biases (*C.R. Booth*, private communications, 1995). Intercomparison must be made among NIMBUS 7 TOMS, Meteor 3 TOMS, *in situ* Dobson readings, and derivations by using ground-based measurements to see why there is a systematic difference. In any case, the causes for the discrepancy are unknown at present.

3.3 Cloud Effect and Equivalent Cloud Optical Depth

In addition to total ozone abundance which is generally expected to have the most important effect on the penetration of UV solar radiation through the atmosphere, temporal and spatial variations in cloud cover are also important parameters affecting UV penetration.

Clouds have a strong influence on UV attenuation. To examine cloud effects on UV penetration, we used the UV radiation model described in Section 2.3 to compute UVB irradiance integrated over the 290 - 320 nm spectral band (instead of 280 - 320 nm in order to compare with the available spectrometer measurement data) under clear sky conditions for comparison with ground-based measurements. The measured column ozone abundances from TOMS were also included in the model calculations. Thus the differences between the modeled and measured UVB

irradiances are the result of the effects of cloud combined with surface albedo used in the model computations.

Grenfell et al. (1994) indicated that the surface albedo in the interior of Antarctica is nearly independent of solar zenith angles. They also show that the albedo has a uniformly high value of 0.96 - 0.98 in the UV and visible region at South Pole Station in the summer, and that this value probably applies throughout the interior of Antarctica. The surface albedos at Barrow, Ushuaia, Palmer, and McMurdo are expected to change throughout the season. The monthly mean observed surface albedo at Barrow from March to May in 1988 changed from 0.92 to 0.84, and dropped to 0.39 to 0.5 in June, 0.18 to 0.20 in July (*Leontyeva and Stamnes*, 1994). Lacking precise knowledge of the surface albedo, which should preferably be measured simultaneously with the downward irradiance for our purpose, we assumed that the surface albedo remains unchanged at the spring time period at each measurement site. The surface albedo was chosen by comparing the measured UVB with computed UVB which never was less than and at least equal to the measured value during the measurement period at each site. We may therefore assume that the sky was clear when there was close agreement between the observed irradiance and the model-predicted clear sky value and that the discrepancies are due to cloud effects. Possible aerosol effects, expected to be small in the pristine polar atmosphere, are thus included in our definition of cloud. Therefore, in our computations, 0.97 was chosen as the surface albedo for South Pole Station, 0.75 for McMurdo Station, 0.65 for Palmer Station, 0.05 for Ushuaia, and 0.85 for Barrow in the model predictions. The Ushuaia installation is near the southern port city of Ushuaia, Argentina. It is surrounded with mountains in the east, north, and

west. In the south lies the ocean. This location is in the foothills of the Andes and it is frequently cloud-covered. The surface albedo may be very low (*C.R. Booth, private communication*, 1994).

Figure 3.9 to 3.13 show comparisons between the computed UVB with clear sky conditions and measured UVB at local noon in spring time (left panels). The comparisons show that clouds blocked in average 10 - 15 % of UVB compared with clear sky at South Pole in the spring period, 10 - 25 % at McMurdo Station, 20 - 60 % at Palmer, 15 - 60 % at Ushuaia, and 10 - 40 % at Barrow.

Comparison of model-predicted and observed irradiance allows inference of the equivalent stratified cloud optical depth (*Stamnes et al.*, 1991). To infer the equivalent cloud optical depth we compared the measured irradiance with the predicted value for a variety of stratified cloud optical thicknesses at a wavelength where ozone absorption is minimum (we chose 349 nm here). The right panels of Figure 3.9 to 3.13 are the derived equivalent cloud optical depths in the spring for the corresponding years at Barrow, Ushuaia, Palmer, McMurdo, and South Pole Station. It was optically clear on most days at South Pole in spring and the clouds were relatively thinner at the South Pole than those at the other four sites. The closer to the south pole, the thinner the clouds become in Antarctica. The equivalent cloud optical depths in spring time at South Pole are usually about 8, at McMurdo about 10, and at Palmer about 40. As for Ushuaia and Barrow, the equivalent cloud optical depths are about 10. We also noted that there were optically thicker clouds in late spring at each site. This may be caused by increasing cloud cover in late spring, but a possibility may be that the surface albedo used in the model prediction was too high, and hence caused the inferred equivalent

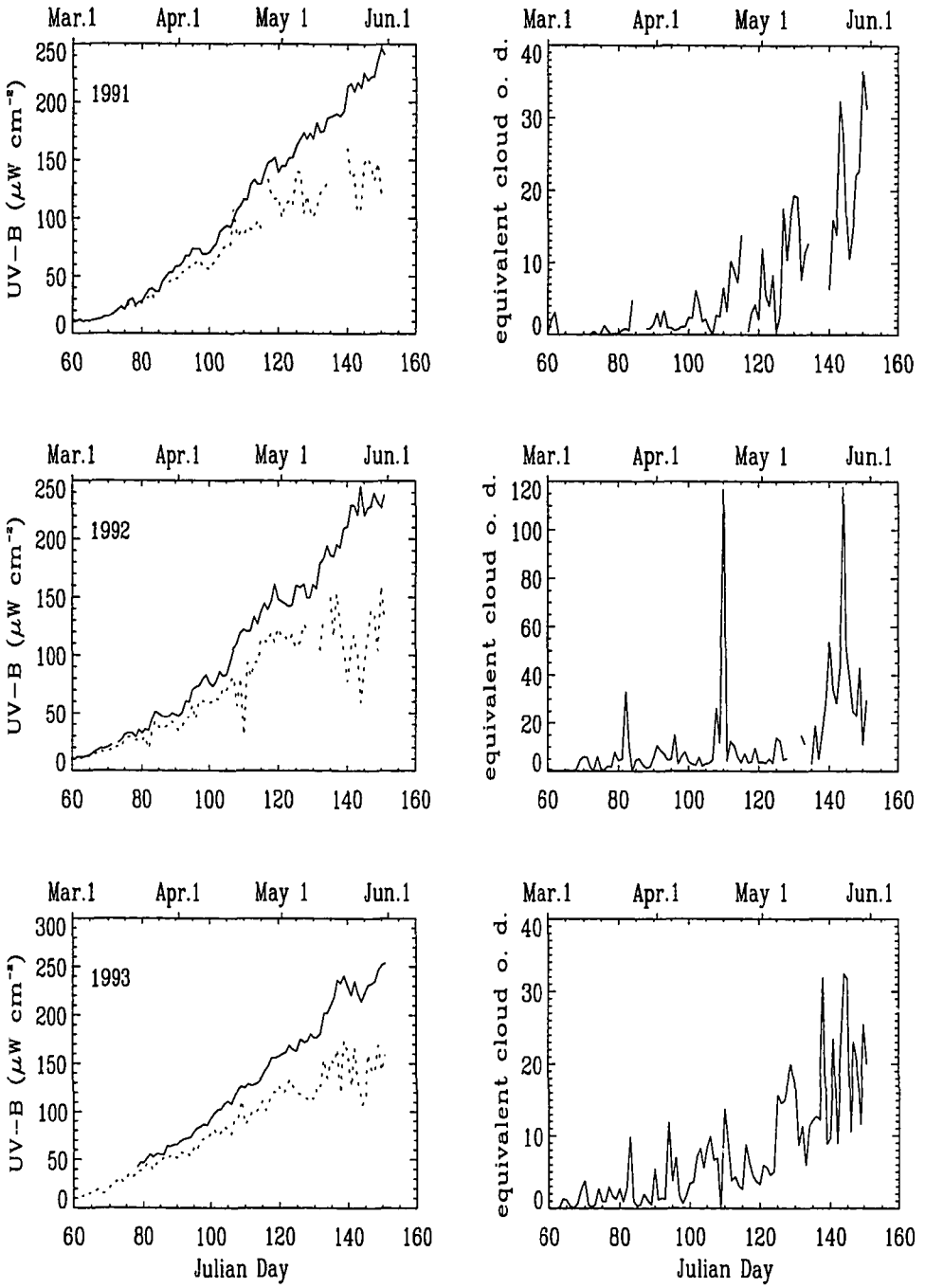

Figure 3.9 Calculated UVB with clear sky conditions (solid lines) (left panels) compared with ground-based measurements (dotted lines) (left panels) and the corresponding equivalent cloud optical depth (right panels) at Barrow in three spring months, March, April, and May, from 1991 to 1993. The surface albedo used in the model calculations was 0.85.

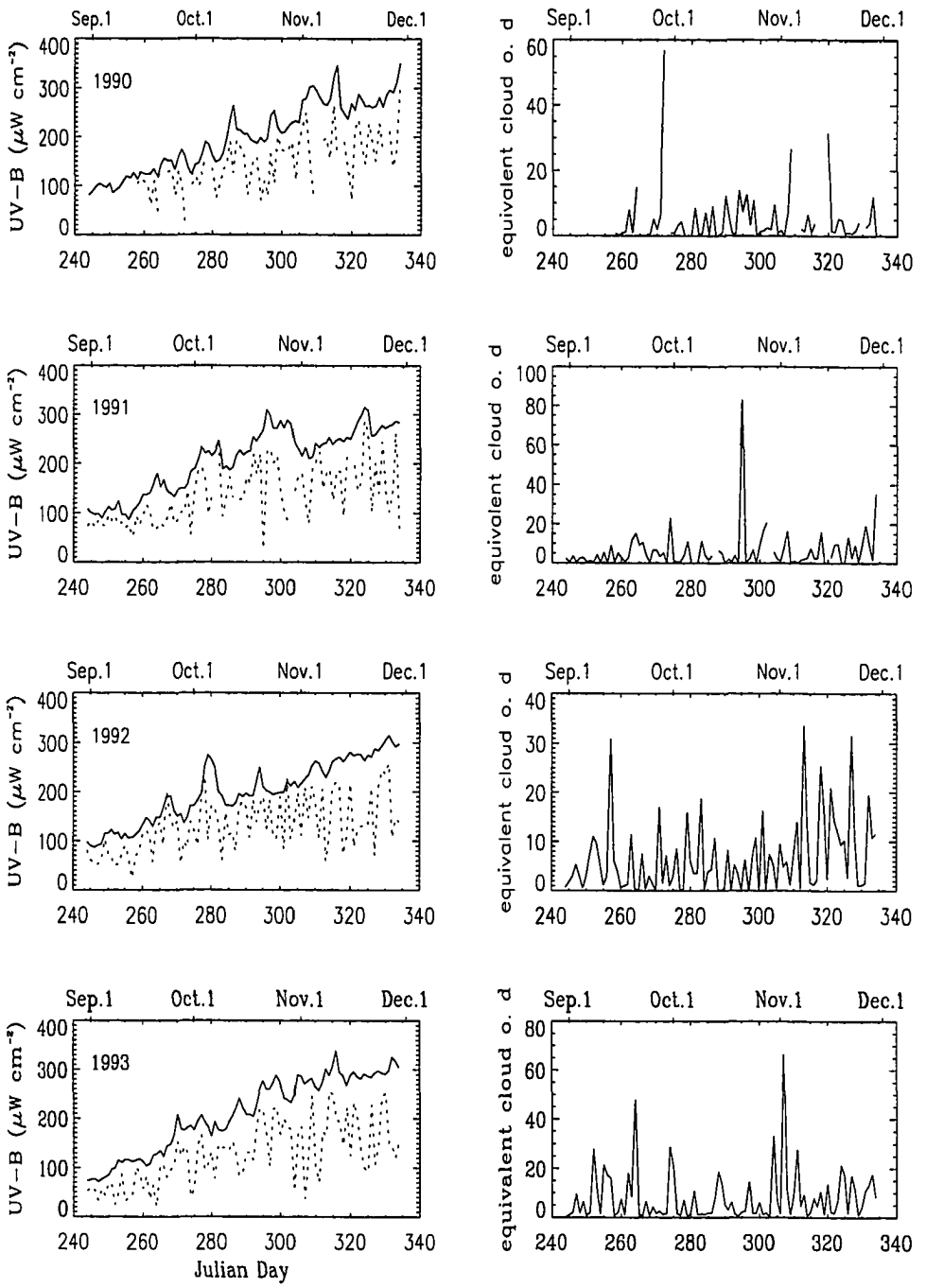

Figure 3.10 As Figure 3.9 but for Ushuaia in three austral spring months, September, October, and November, from 1990 to 1993. The surface albedo used was 0.05.

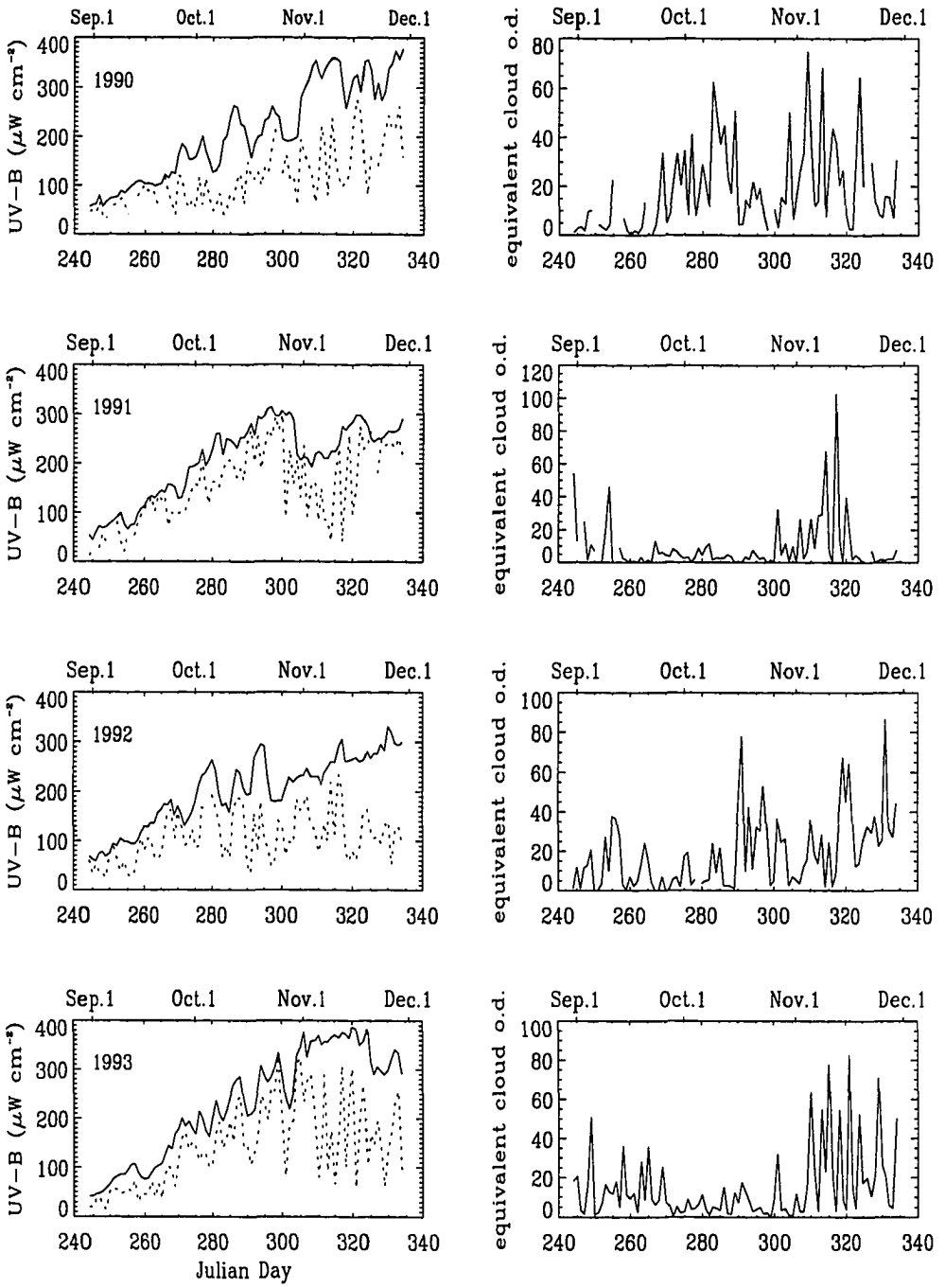

Figure 3.11 As Figure 3.9 but for Palmer in three austral spring months, September, October, and November, from 1990 to 1993. The surface albedo used was 0.65.

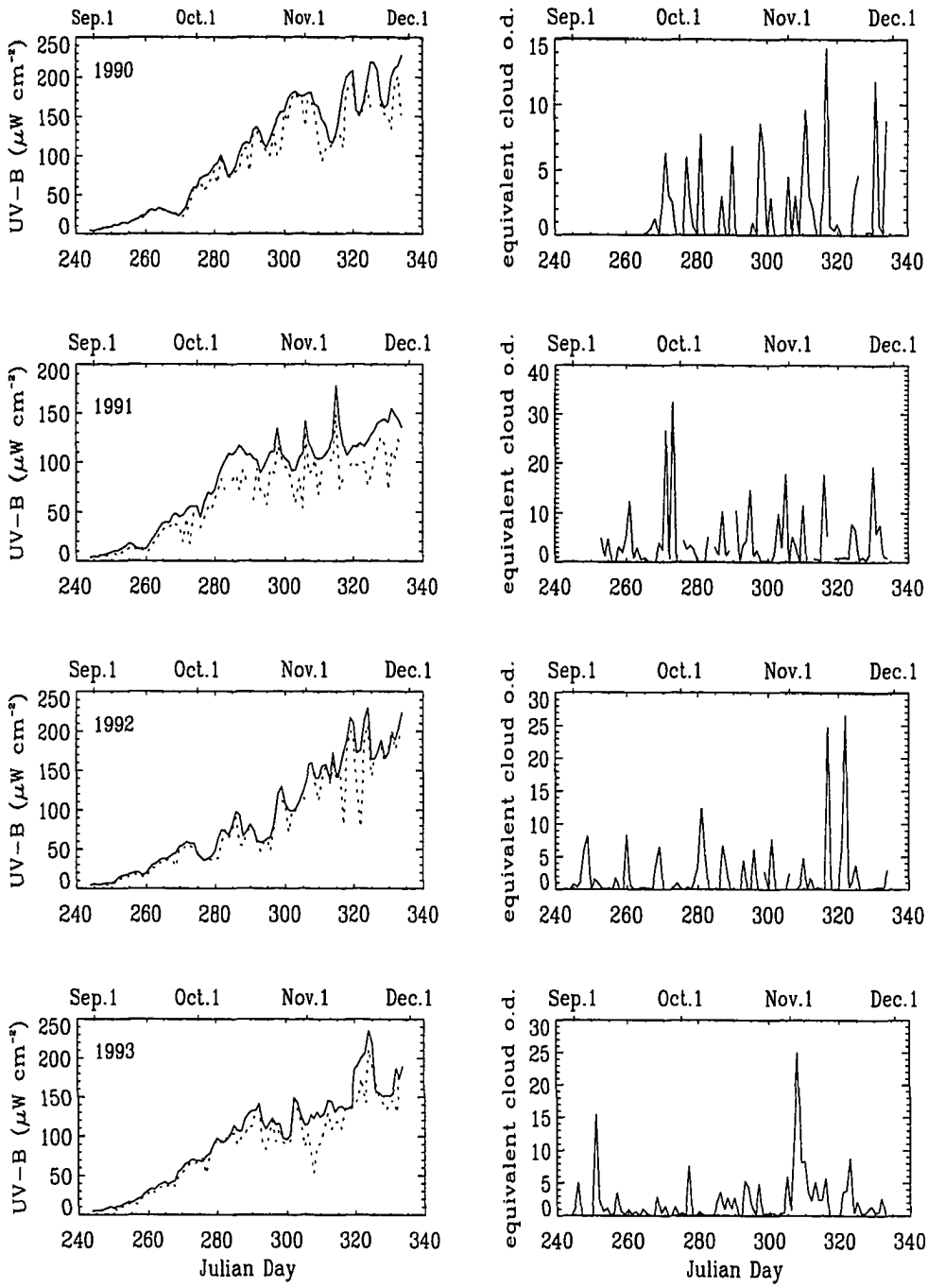

Figure 3.12 As Figure 3.9 but for McMurdo in three austral spring months, September, October, and November, from 1990 to 1993. The surface albedo used was 0.75.

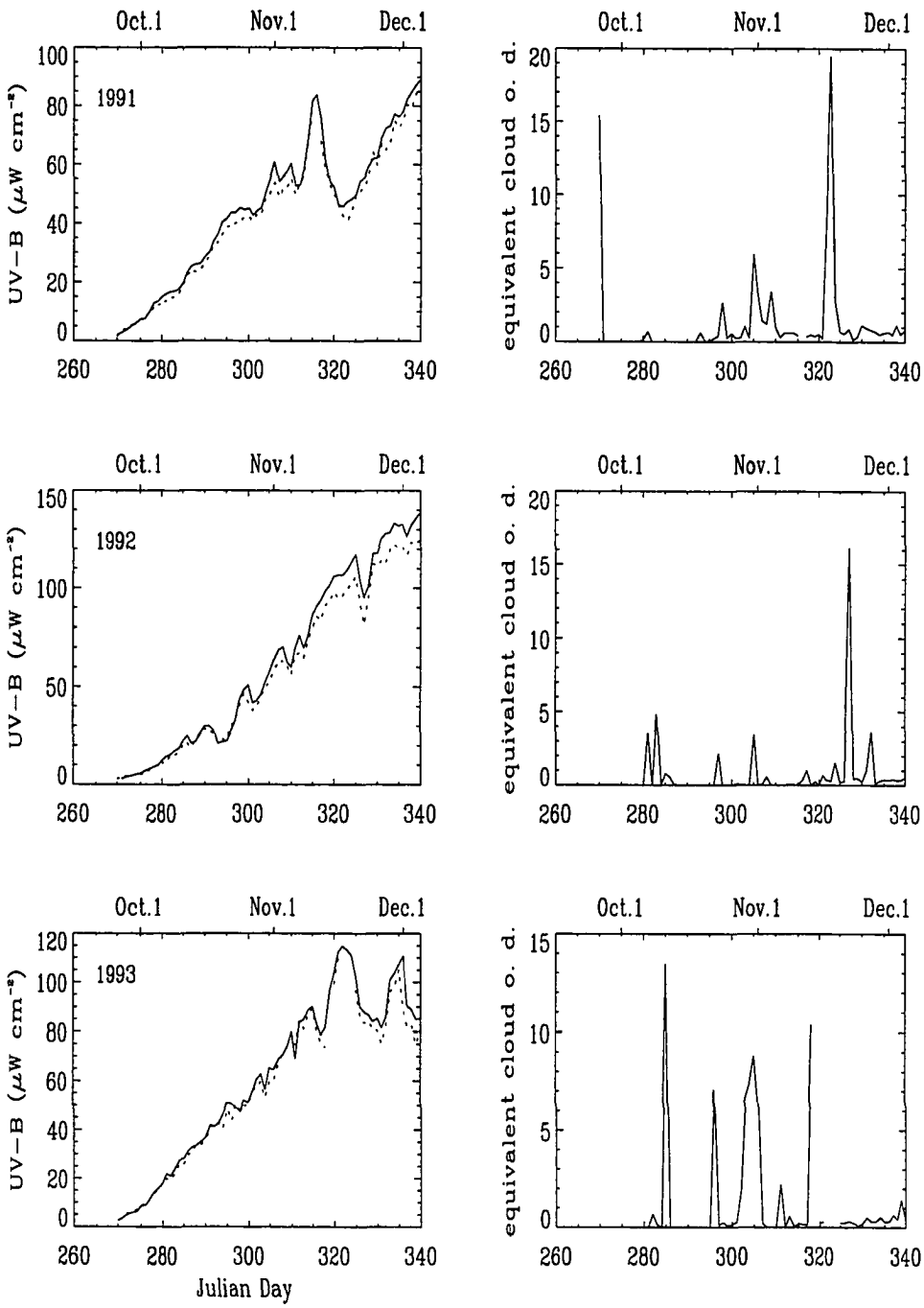

Figure 3.13 As Figure 3.9 but for South Pole in three austral spring months, September, October, and November, from 1991 to 1993. The surface albedo used was 0.97.

cloud optical depth to be too high. The surface albedo changes very rapidly in the transitional period in late spring. The surface albedo must be chosen very carefully in order to predict the cloud optical depth correctly.

3.4 Summary of the Chapter

• The total ozone abundance derived from ground-based measurements of irradiance is in good agreement with TOMS measurement in the spring time in Antarctica, but is higher in the winter and lower in the summer. At Barrow, our method underestimates ozone abundance before summer solstice and overestimates it after summer solstice in comparison with TOMS data.

• This systematic difference may be caused by (a) the inconsistency of temperature profiles used in the derivations with those used in the TOMS algorithm, (b) errors introduced from uncertainties in the ground-based solar irradiance measurements.

• The agreement between surface-derived column ozone and TOMS can be improved by using two solar irradiance measurements at narrow wavelength intervals below 340 nm taken from the same resolution spectral scan to remove the effects of rapid and random variability of cloud optical thickness.

• There is no obvious ozone depletion at Barrow, Alaska during the last 3 years (before 1994).

• The closer to the South Pole, the smaller the cloud optical depth becomes in Antarctica.

• The clouds were relatively thick in late spring both in Antarctica and in the

Arctic.

Chapter 4

Ozone Depletion and UV Penetration to the Earth's Surface and into the Underlying Water

4.1 Introduction

With depletion of the ozone layer the atmosphere becomes more transparent at shorter wavelengths, thereby increasing the amount of biologically harmful ultraviolet radiation (UVB, 280 to 320 nm) reaching the surface of the earth (*Stamnes et al.*, 1992) and penetrating to ecologically significant depths in the ocean (*Smith and Baker,* 1979, 1980, 1981; *Smith et al.*, 1992b). There is considerable and increasing evidence that UVB radiation, resulting from depletion of the ozone layer,

may be detrimental to various forms of marine life in the upper layers of the ocean. For example, increased UVB may decrease phytoplankton productivity by 1 - 12 % (*Arrigo*, 1994; *Holm-Hansen et al.*, 1993; *Smith et al.*, 1992b; *Cullen et al.*, 1992) in the Southern ocean. The highly productive surface waters of the oceans at higher latitudes provide important feedbacks with global climate through their exchange of radiatively active organic gases. If the impacts of the changes in UVB on biodiversity are significant, then the altered release of CO_2, dimethyl sulfide, and other gases will be important in determining potential feedbacks in radiation and energy exchange. It is likely that we do not yet understand all of the potential effects of enhanced UV radiation on the biosphere.

UVB measurements in aquatic systems require specialized instrumentation. Only a few measurements of UV penetration into the ocean have been made. Therefore, it is worthwhile to use theoretical radiation models that account for ozone absorption and other factors that can affect UVB to evaluate the changes in UVB surface and underwater radiation.

There are a number of models which have approached the radiative transfer problem in the atmosphere ocean system developed with different methods (*Jin and Stamnes*, 1994; *Morel and Gentili*, 1991; *Kattawar and Adams*, 1989; *Mobley*, 1989; *Kirk*, 1981). The discrete ordinate method has been satisfactorily used to solve the radiative transfer problem in vertically inhomogeneous media, such as the atmosphere. *Jin and Stamnes* [1994] developed a coupled atmosphere-ocean model using the discrete ordinate radiative transfer method, which provides a solution of the coupled radiative transfer equations pertinent for two strata with different indices of refraction separated by a plane interface, such as the atmosphere

overlying a calm ocean surface. The model has been compared with six other models in current use and has been found to be both reliable and efficient (*Mobley et al.*, 1993). We will use this model to investigate the impact of decreased ozone levels on aquatic systems.

4.2 Coupled Radiative Transfer Model for UV and Visible Radiation

The underwater spectral irradiance depends on the spectral and angular distribution of the solar radiation arriving at the earth's surface, and on the optical properties of the water body, which in turn are determined by Rayleigh scattering and absorption by water molecules (pure water) as well as scattering and absorption by suspended particles of organic and inorganic origin.

The atmosphere and ocean are each divided into a sufficient number of layers to resolve the optical properties in each medium. The model uses inputs of optical properties, such as optical depth, single scattering albedo and phase function for each layer of both the atmosphere and the ocean, and it computes the direct and diffuse upward and downward irradiances at arbitrary levels. The spectral distribution of the solar irradiance at the top of the atmosphere is needed. Vertical profiles of atmospheric ozone, density, cloud, aerosol, and suspended particles and dissolved organic materials in the ocean are also required. These are used to generate optical properties for each layer in the atmosphere and the underlying ocean.

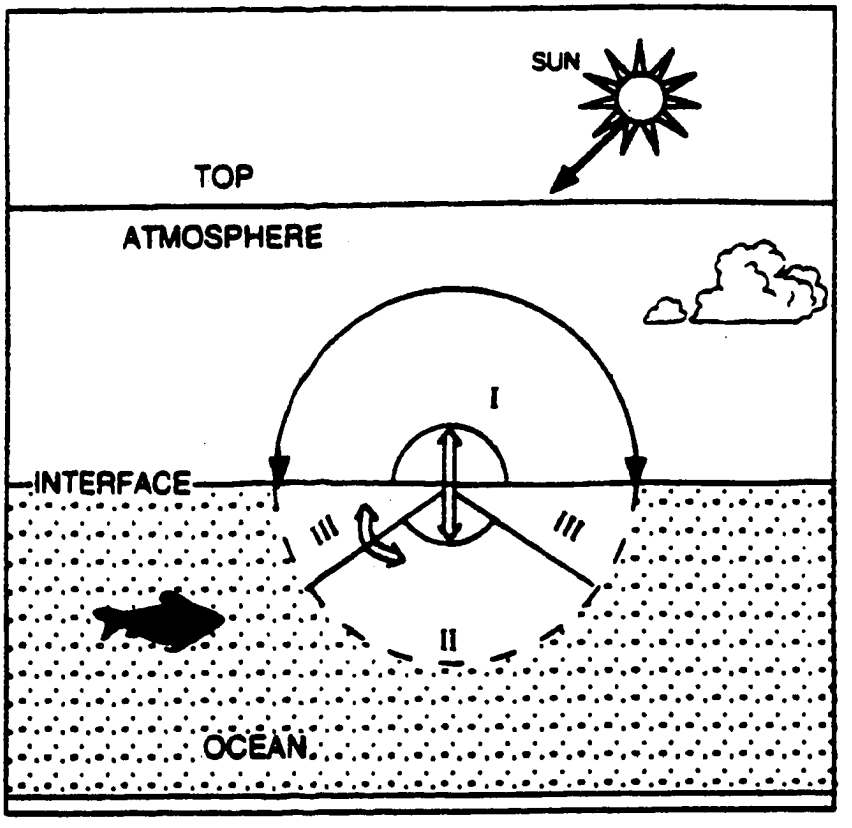

Figure 4.1 Schematic illustration of the atmosphere-ocean interface indicating the region of total reflection in the ocean and the region which 'communicates' with the atmosphere. Refraction at the interface allows photons to move from region *I* (the atmosphere) into region *II* in the ocean and vice versa. Photons in region *III* are totally reflected at the interface; scattering processes allow these photons to move back and forth between regions *II* and *III* as indicated.

In order to describe the transfer of radiation in the coupled atmosphere-ocean system it is important to take into account the change in index of refraction occurring at the interface between the atmosphere and the ocean. The relative refractive index for the atmosphere is taken to be unity and that for the ocean is assigned a constant value of 1.3 (neglecting for simplicity the slight wavelength dependence).

The model rigorously includes the effects of multiple scattering. The angular dependence of the radiation is divided into a suitable number of quadrature points

('streams'). Appropriate 'streams' and weights are chosen for the interface continuity relations. The refraction and total reflection at the interface of the two strata have been taken into account by assigning different numbers of 'streams' in the atmosphere and in the water. The same number of streams is used in the atmosphere and in the refractive part of the ocean which connects directly with the atmosphere, while additional streams are used to describe the radiation in the total reflection region as schematically illustrated in Figure 4.1. The accuracy will be enhanced with an increase in the number of streams, but convergence depends strongly on the change in refractive index across the interface. Using 8 'streams' in the atmosphere and refractive part of the ocean (region I and II in the Figure 4.1), and 6 additional 'streams' in the total reflective region (region III in the Figure 4.1) (i. e. 14 'streams' total in the ocean) yields an accuracy of about 1% (*Zeng et al.*, 1993).

As already stated, to compute the transfer of ultraviolet and visible radiation throughout the coupled atmosphere-ocean system we must know the spectral distribution of the radiation incident at the top of the atmosphere as well as the optical properties of the atmosphere and water media.

a. Extraterrestrial Solar Spectrum

The solar irradiance in the range between 280 and 700 nm represents about half of the total solar energy output incident at the top of of the earth's atmosphere. There are several extraterrestrial solar spectra in current use. The spectrum used here is adopted from *Nicolet* (1989)(Figure 2.1a).

b. Atmospheric Ozone

Ozone is the most important absorber of solar UV radiation through the at-

mosphere. Since ozone scatters very small amounts of radiation (*Paur and Bass*, 1983), ozone scattering is ignored here. The absorption cross sections for ozone are adopted from *Molina and Molina* (1986)(Figure 2.1b) because they were measured at three different temperatures and had higher resolution. Other gases (the two most important being nitrogen dioxide and sulphur dioxide) absorb in 280-400 nm region, but these gases are not included in the radiation scheme as their effect on integrated UV surface irradiances is small.

c. Rayleigh Scattering

Rayleigh scattering in the atmosphere is very important in the UV, due to its scattering cross-section having a nearly $1/\lambda^4$ dependence. The use of different standard altitude profiles for atmospheric pressure and temperature causes a variation of 1% or less in Rayleigh optical depth (*Teillet*, 1990), and natural variations lead to day-to-day differences in Rayleigh optical depth of $\pm$ 3% (*Zeng et al.*, 1994). The Rayleigh scattering cross sections were calculated from the empirical formula deduced by *Nicolet* (1984), and the subarctic summer atmosphere developed by *McClatchey et al.* (1972) were adopted as the vertical atmospheric profiles.

d. Atmospheric Aerosols and Clouds

The effects of atmospheric aerosol and clouds are included in the model. The Henyey-Greenstein phase function is used and the delta-M transformation (*Wiscombe*, 1977) is adopted, which has been shown to optimize the performance of the model in solving practical radiative transfer problems involving sharply forward-peaked phase functions associated with scattering from cloud droplets and aerosol particles in the atmosphere.

For simplicity we considered only the combined effect of clouds and aerosols,

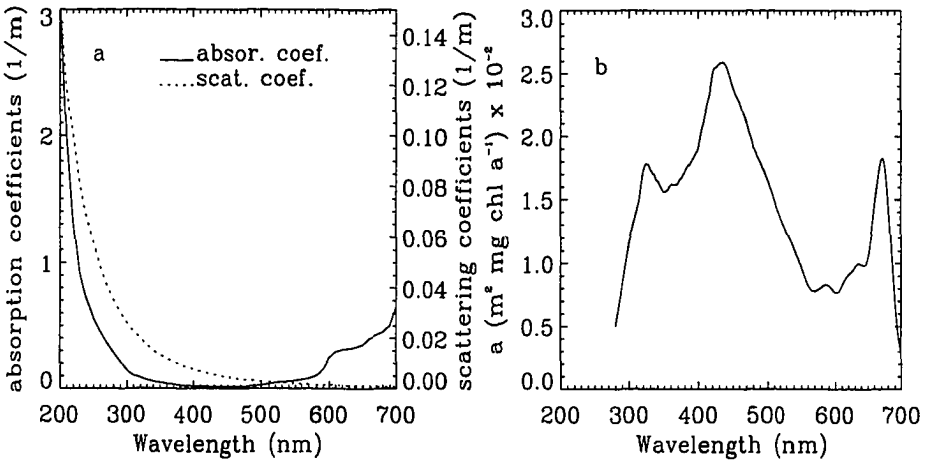

Figure 4.2 (a) The absorption and scattering coefficients for pure sea water; (b) Specific spectral absorption coefficients for phytoplankton.

and used an asymmetry factor of 0.9 for the Henyey-Greenstein phase function.

e. Extinction by Pure Sea Water

The extinction of the natural sea water includes the absorption and scattering of pure sea water, suspended particles, and dissolved organic or inorganic materials.

Water itself absorbs weakly at near-UV and blue wavelength. In pure water at wavelengths between 370 to 450 nm, molecular scattering provides 20-25% of the total beam attenuation (*Smith and Baker*, 1981). For the clearest ocean water the Rayleigh scattering phase function is applied. The absorption and scattering coefficients for pure sea water are adopted from *Smith and Baker* (1981) (Figure 4.2a). It should be noted that the spectral absorption coefficient of pure sea water provided by *Smith and Baker* (1981) represents an upper bound in the wavelength range of oceanographic interest, 200 to 800 nm. In fact, they commented that at wavelengths below 300 nm, their values are merely an educated guess. They also

estimated the accuracy of the absorption coefficients to be within +25% and -5% between 300 and 480 nm, and +10% to -15% between 480 and 800 nm. However, their values appear to be reasonably good and are widely used.

f. Extinction by Other Materials

From available evidence (*Smith and Baker,* 1978a, b; *Jerlov*, 1976), the absorption and scattering by chlorophyll and dissolved organic matter (DOM) are likely to be among the principal optical components contributing to the extinction in UVB region. But the concentration of DOM seems to be much more influenced by natural (or anthropogenic) land sources than by marine biological activity (*Bricaud et al.*, 1981). For simplicity we consider only the absorption and scattering by chlorophyllous pigment. As in the treatment of atmospheric aerosols and cloud droplets, we use the Henyey-Greenstein phase function and the delta-M approximation to represent phase functions for suspended particles and dissolved materials. We used 0.92 for the asymmetry factor, which is fitted from the phase function given by *Mobley et al.* (1993).

The scattering coefficients of chlorophyll $b(\lambda)$ may be calculated from the expression (*Gordon and Morel,* 1983):

$$b(\lambda) = (\frac{550}{\lambda})0.3(C)^{0.62} \tag{4.1}$$

where λ is wavelength and C is chlorophyll concentration. The above expression is deduced from measurements in the near-ultraviolet and visible part of the spectrum (above 350 nm). Lacking data in the UV spectral range, we assume that this expression can be used also below 350 nm, as a first approximation.

The specific absorption coefficients differ among phytoplankton species. *Sathyen-*

dranath et al. (1987) measured spectral absorption coefficients for eight species of cultured phytoplankton. Their measurements indicated that there are distinct absorption peaks at about 440 nm and 675 nm; the blue peak is one to three times as high as the red one (for a given species) due to the contribution of accessory pigments that absorb in the blue, and there is relatively little absorption between 550 and 650 nm, with the absorption minimum near 600 nm being 10% to 30% of the value at 400 nm.

The chlorophyll-specific spectral absorption coefficients we used in the model are shown in Figure 4.2b. The absorption coefficients will be the product of the chlorophyll concentration, C, and the specific absorption coefficient.

g. Model levels

As already mentioned the vertical inhomogeneity of the atmosphere and the water column can be accounted for by dividing each stratum into a sufficient number of layers to resolve the changes in optical properties with altitude in the atmosphere and depth in the ocean so that the optical properties are constant in each layer, but are allowed to vary from layer to layer. The distribution of model levels should be chosen so as to resolve adequately the predominantly scattering levels from the predominantly absorbing levels both in the atmosphere and ocean. We divided the atmosphere into 33 layers with dense layers in the lower troposphere, and the underlying water into 19 layers with compact layers in the upper water and assumed the ocean to be sufficiently deep that reflection from the ocean floor is of little consequence.

4.3 Comparison of Computed and Modeled Irradiance

It is worthwhile to use a well developed radiative transfer model to simulate the underwater UVB field for comparison with *in situ* measurements. Smith and coworkers (*Smith et al.*, 1992b) directly measured the increase in and penetration of UVB radiation into the Antarctic waters and provided the first conclusive evidence of a direct ozone related effect on a natural phytoplankton population. They measured the spectral irradiance between 300 and 700 nm and presented the ratio of UVB irradiance (Q_{UVB}) to total irradiance ($Q_{TOTAL} = Q_{UVB} + Q_{UVA} + Q_{PAR}$) as a function of depth, and found that this ratio is O_3-dependent in the Southern Ocean. Thus, as the ozone layer thinned, sea surface and depth-dependent ratios of Q_{UVB} to Q_{TOTAL} increased. The vertical attenuation coefficients for spectral irradiance are nearly the same under and outside of the ozone hole, as demonstrated in Fig. 2 of the paper by *Smith et al.* (1992b) (hereafter referred to as Smith's).

To mimic the downwelling spectral irradiance penetrating to selected depths within the water column and the impact of ozone depletion on the ratios of Q_{UVB} to Q_{TOTAL} we used the coupled atmosphere-ocean model described in Section 4.2 and compared the computed results with Smith's measurements.

4.3.1 Downwelling irradiance

In general, the downwelling irradiance is a function of solar zenith angle, cloud amount and aerosol loading, total ozone content and its vertical distribution, and

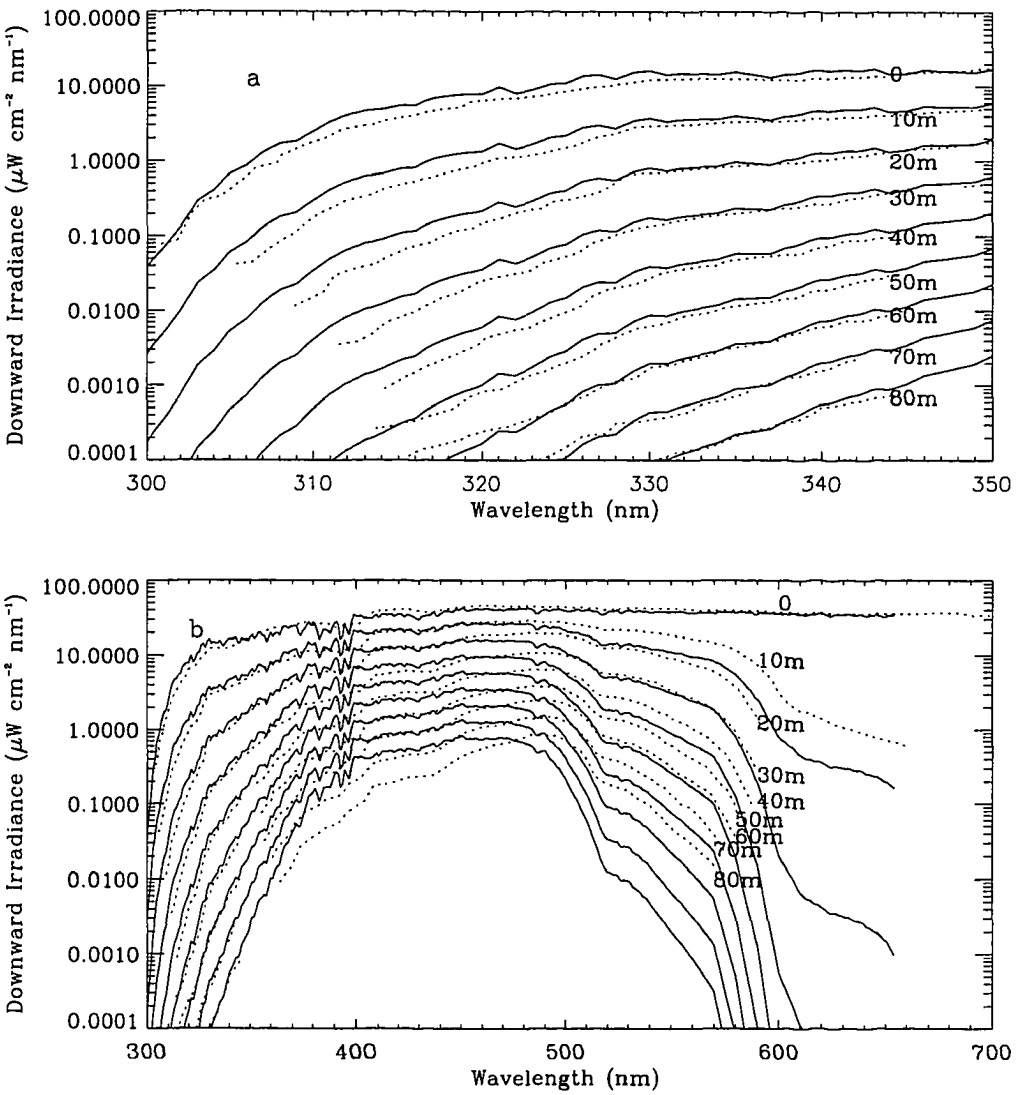

Figure 4.3 Comparison between model computations and measurements (*Smith et al.*, 1992b); solid lines are modeled and dotted lines are measured. (a) Downwelling spectral irradiance from 300 to 350 nm at selected depths of water at 65^0S at solar zenith angle of 50^0 with total ozone abundance of 320 DU. The chlorophyll concentration in the water was 0.4 $mg\ m^{-3}$. (b) Same as (a) but for spectral range from 300 to 700 nm.

optical properties in the water body. The optical properties of the water, in turn, should include single scattering albedo, and asymmetry factor of the phase function. The surface UVB radiation will be enhanced if total column ozone reduction is the only effect considered. Figure 4.3a presents the downwelling spectral UV irradiance from 300 to 350 nm and Figure 4.3b shows the irradiance for the whole spectrum (300 - 700 nm) at selected depths of water compared with measurements of Smith's, which were made at 65^0S at a solar zenith angle of 50^0 for an observed ozone abundance of 320 Dobson Units. Solid lines are from the model calculation, dotted lines represent the measurements. The sky was lightly overcast at the time of the measurements. We used an optical depth of 1 in the model calculation to simulate the combined impact of cloud cover and aerosol loading. This value was chosen to make the modeled surface irradiance agree with the measured surface irradiance. We used the measured chlorophyll concentration to calculate the optical properties in the ocean. The chlorophyll concentration was 0.4 $mg\ m^{-3}$ down to 30 meters from the surface and considered to be homogeneous vertically. There is reasonably good agreement between model calculation and measurement in the wavelength range from 300 nm to 350 nm (Figure 4.3a), but for wavelengths above 350 nm the agreement is poor (Figure 4.3b).

The computed spectral irradiance at the earth's surface is almost the same as the measured one between 300 and 700 nm. When the light penetrates into the ocean, however, the computed spectral distribution disagrees with the measured distribution. The agreement gets progressively worse between 470 to 700 nm. This discrepancy could not result from errors in phytoplankton absorption, because phytoplankton absorbs very little in the 550 - 600 nm region. Also it could not

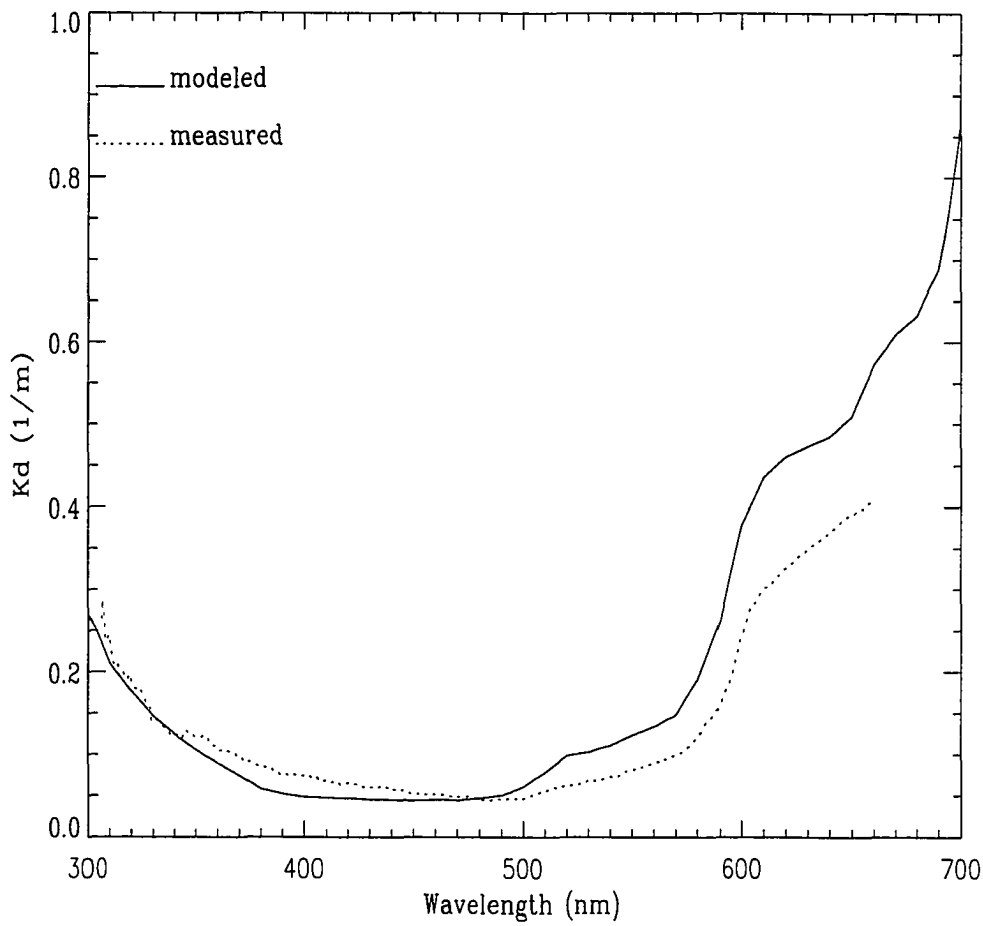

Figure 4.4 Comparison of diffuse attenuation coefficients K_d between model computation and measurement. Solid line presents modeled and dotted line measured.

be caused by ignoring DOM which absorbs very little in red, but its absorption increases rapidly with decreasing wavelength and can be significant at blue and ultraviolet wavelengths.

We inferred the apparent diffuse attenuation coefficient K_d which is shown in Figure 4.4 both from the model and measurements by taking the derivative of the irradiances:

$$K_d(z;\lambda) = -\frac{d \ln E_d(z;\lambda)}{dz} \tag{4.2}$$

where E_d is the downwelling irradiance. We used the difference between the inferred K_d's to determine the correction of the specific absorption coefficients which makes the modeled K_d agree with the measured K_d. Results obtained from the model using the specific absorption coefficients corrected in this manner shows that the difference between modeled and measured irradiances is not due to phytoplankton absorption. The differences suggest that a more likely possibility for the disagreement is that the attenuation coefficient used for pure sea water in the model was not consistent with the conditions prevailing during the measurements. It should be noted that the pure sea water absorption coefficients (*Smith and Baker*, 1981) are upper bounds; the true absorption of pure sea water is likely to be somewhat lower, at least at violet and blue wavelengths (*Songandares et al.*, 1991). This disagreement may also be caused by inaccuracies in the measurement itself. A spectroradiometer optimized for UV measurements may not be suitable for measurements in the visible spectral range.

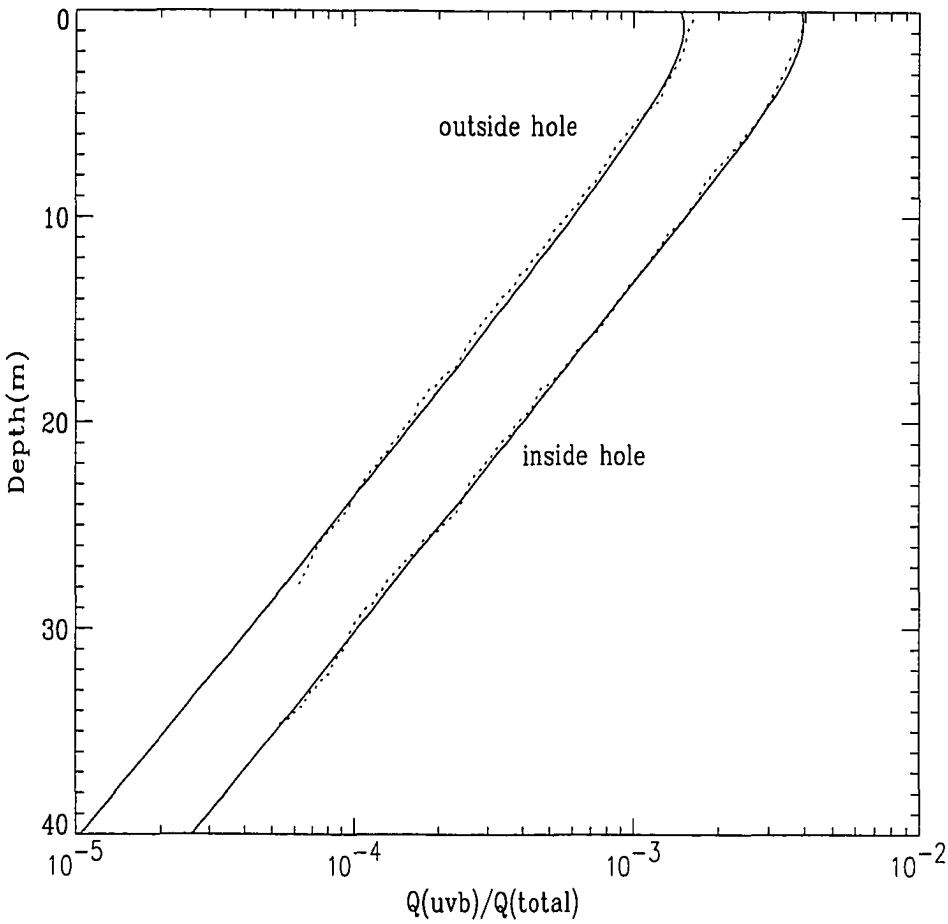

Figure 4.5 Comparison between model computations and measurements (*Smith et al.*, 1992b): depth versus Q_{UVB}:Q_{TOTAL}. Solid lines are modeled and dotted lines are measured. Inside the ozone hole, the ozone abundance is 150 DU, the solar zenith angle is 56^0, and the vertical distribution of chlorophyll concentration is: 0.57 $mg\ m^{-3}$ from the surface to 20 meters, 0.47 $mg\ m^{-3}$ below 20 meters. Outside the ozone hole, the ozone abundance is 350 DU, solar zenith angle is 57^0, and the vertical distribution of chlorophyll concentration is: 1.9 $mg\ m^{-3}$ from the surface to 10 meters, 1.6 $mg\ m^{-3}$ from 10 to 20 meters, and 1.5 $mg\ m^{-3}$ below 20 meters.

4.3.2 Underwater UVB distribution

Figure 4.5 illustrates the ratio of energy in UVB band (280 - 320 nm) to that in the full spectrum (280 - 700 nm) (Q_{UVB}:Q_{TOTAL}) versus depth at 65^0S inside and outside the ozone hole. We used the measured total ozone abundance, as well as the pertinent solar zenith angle, and vertical distribution of chlorophyll concentration in the model computations. Inside the hole, the total ozone abundance was 150 DU, the solar zenith angle was 56^0, and the vertical distribution of chlorophyll concentration was taken to be inhomogeneous: 0.57 $mg\ m^{-3}$ from the ocean surface to 20 meter depth, and 0.47 $mg\ m^{-3}$ below 20 meter in the ocean. Outside the hole, total ozone abundance was 350 DU, the solar zenith angle was 57^0, and the vertical distribution of chlorophyll concentration was: 1.9 $mg\ m^{-3}$ from the ocean surface to 10 meters below, 1.6 $mg\ m^{-3}$ from 10 meters to 20 meters below, and 1.5 $mg\ m^{-3}$ below 20 meters of water. We can see that there is very good agreement between modeled and measured ratios down below the surface. We also note that there is some curvature in the model results in the first couple of meters of water, that is absent in the measured results. This may be caused by ignoring the influence of surface waves in the model computations, but this point needs further investigation.

Solar elevation has a critical impact on the UV radiation reaching the earth's surface. It was overcast when the measurements were made, but the solar zenith angle inside and outside the ozone hole was almost the same. Since the optical properties of clouds and aerosols depend weakly on wavelength, the influence of clouds and aerosols on the ratio (Q_{UVB}:Q_{TOTAL}) is expected to be minor. This

circumstance allows us to investigate the impact of changes in ozone abundance on the surface and submarine irradiance ratio. The reduction of atmospheric ozone will increase the surface and underwater UV irradiance. Although the vertical chlorophyll distributions in the water are different under and outside the ozone hole, the impact of this difference on the vertical Q_{UVB}:Q_{TOTAL} attenuation coefficients is small and the vertical attenuation coefficients are nearly the same inside and outside the ozone hole (Figure 4.5). Therefore, if UVB exposure is doubled at the surface, it will be doubled at all depths, and the critical depth above which UVB damage may occur will be deeper in the water column.

4.3.3 Factors that affect submarine UV prediction

To calculate UV radiation through the atmosphere we need to know the extraterrestrial irradiance at the top of the atmosphere, total ozone abundance and its vertical distribution, cloud cover and aerosol loadings, and other factors (*e.g.* vertical profiles of air pressure and temperature, phase function, asymmetry factor, and single scattering albedo) that impact the penetration of UV radiation reaching the earth's surface (*Zeng et al.,* 1994). When the inputs of the atmospheric parameters to the model are known, the errors of surface UV prediction can be less than a few percent compared with measurements (*Zeng et al.*, 1994, *Wang and Lenoble*, 1994). The computation of UV radiation into the water body depends on the accurate calculation of UV radiation arriving at the ocean surface and the adoption of proper optical properties of the water system. The difficulty in modeling submarine UV radiation lies in the limited knowledge of the optical

properties of the medium which show large temporal and spatial variations and seldom resemble those of pure sea water. In our calculation here we considered only the extinction by chlorophyll pigment and pure sea water. Lacking sufficient data, we used scattering coefficients for chlorophyllous pigment deduced from measurements of the spectrum above 350 nm. The asymmetry factor in the water body is wavelength-dependent. Lacking proper data, we chose a constant asymmetry factor of 0.92 in the model calculations. Uncertainties in these parameters will certainly lead to inaccuracies in the predictions, whose magnitudes are unknown at present.

The above model calculations are very preliminary. Detailed comparisons and comprehensive tests of the model can only be done when the optical properties of water system are better known. However, we believe that the coupled atmosphere-ocean radiative transfer model is basically sound, and that it can be used to make estimates of seasonal and latitudinal variations of underwater UV exposure due to the depletion of atmospheric ozone, and to study the dependence of the underwater UV radiation field on chlorophyll concentration.

4.4 UV Penetration to the Earth Surface and into the Ocean

Although the UVB radiation environment depends on ozone column abundance, the relative increase of UVB exposure for a given ozone reduction is a function of solar elevation. UVB radiation arriving at the earth surface is enhanced as total

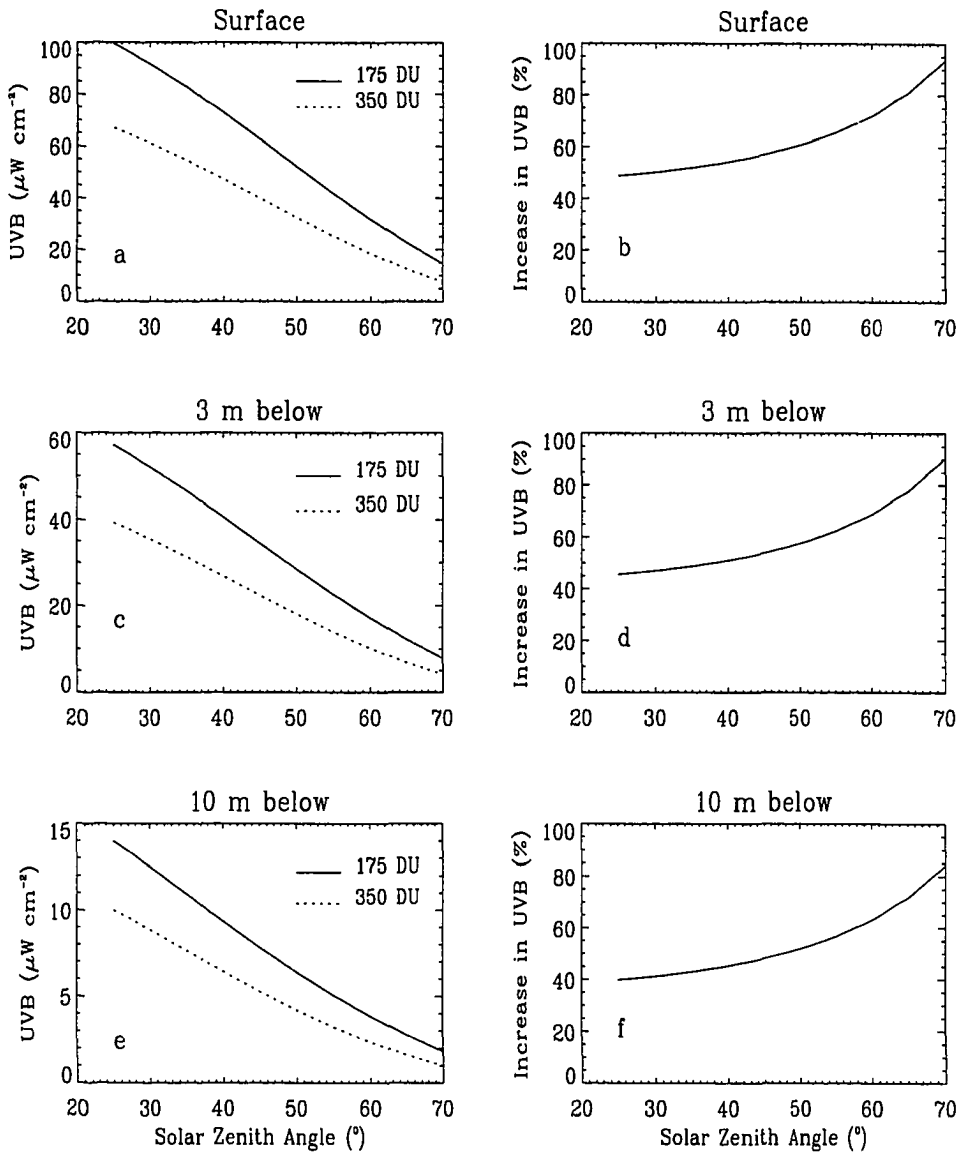

Figure 4.6 Changes of surface and underwater UVB irradiance with solar zenith angle in total ozone abundance of 350 DU and 175 DU (left panel) and the corresponding relative changes (right panel).

column ozone decreases, and so will the UVB exposure at all depths in the ocean. Figure 4.6 presents the surface UVB changes with solar zenith angle for 'normal' ozone abundance (350 DU) and 50% reduction in ozone abundance (175 DU) under clear sky conditions (left panel), and the corresponding relative changes (right panel) at selected depths. The chlorophyll distribution was taken to be vertically homogeneous with a concentration of 0.4 $mg\ m^{-3}$. The largest relative increase in UVB occurs at large solar zenith angles; a 50% reduction of ozone abundance from normal level leads to a 50% increase of UVB irradiance at solar zenith angle of 25^0 and 95% increase at 70^0. We also note that the largest enhancements due to O_3 reduction from 350 DU to 175 DU occur in the upper layers of the water column. Thus both the relative and absolute increase in UV exposure is highest close to the surface, therefore the UV increase due to ozone depletion is expected to be most harmful to the organisms living in the upper levels of the ocean.

Figure 4.7 shows the relative decrease in UVB irradiance at three depths in the water medium as compared to the irradiance incident at the sea surface. Solid lines are for a chlorophyll concentration of 0.5 $mg\ m^{-3}$ and dotted lines for 1.0 $mg\ m^{-3}$. Chlorophyll concentrations for various waters range from 0.01 $mg\ m^{-3}$ in the clearest open waters, to 10 $mg\ m^{-3}$ in productive coastal upwelling regions, to 100 $mg\ m^{-3}$ in eutrophic estuaries or lakes. The globally averaged, near-surface, open-ocean value is approximately 0.5 $mg\ m^{-3}$ (*Mobley,* 1994). We used only two typical values to test the sensitivity of UVB decrease within the water column to chlorophyll concentration. The more chlorophyll in the water, the more UVB is absorbed. Phytoplankton dwell in the upper layers of the water column (the photic zone) because of their requirement for solar radiation. We note that UVB

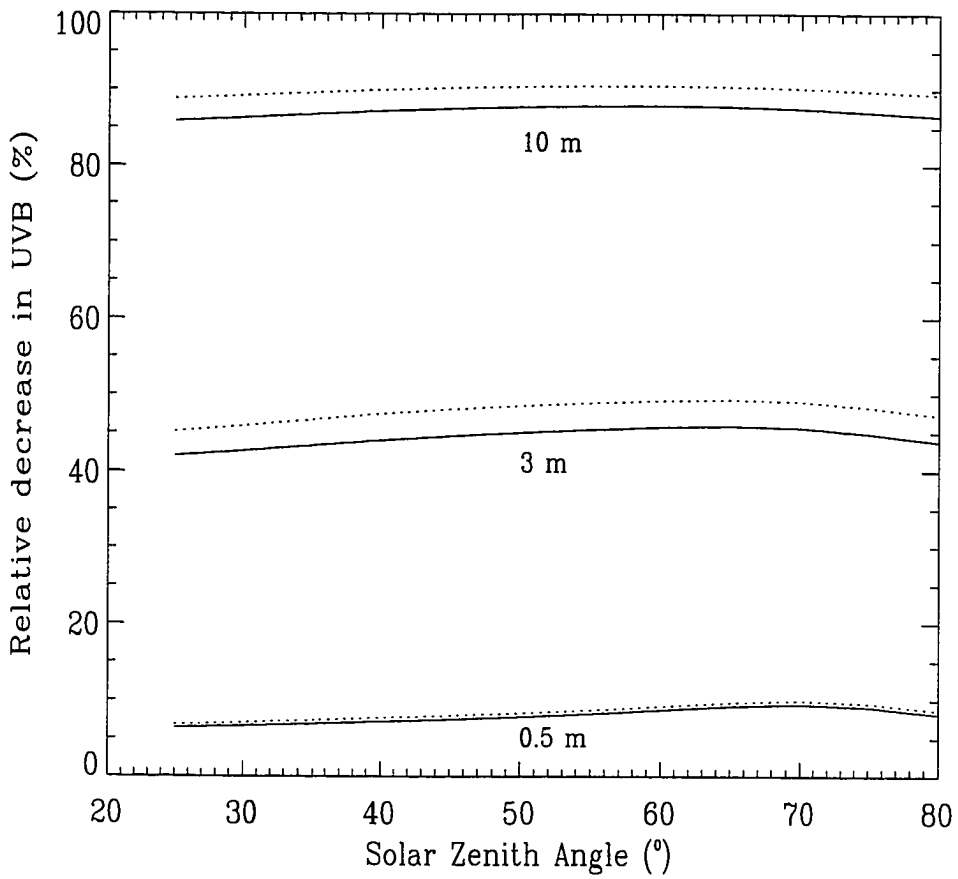

Figure 4.7 Relative decrease in UVB irradiance at selected depths as compared to that at the sea surface. Solid lines are for a chlorophyll concentration of 0.5 $mg\ m^{-3}$ and dotted lines for 1.0 $mg\ m^{-3}$.

irradiance is significantly absorbed in the uppermost layers of the ocean. About 45% of the incident UVB radiation is absorbed by the first 3 meters and up to 87% is absorbed by the time the radiation reaches 10 meters below for a chlorophyll concentration of 0.5 $mg\ m^{-3}$. The relative decrease in submarine UVB compared to the levels at the surface depends only slightly on solar zenith angle, with the largest depletion occurring just below the surface for a solar zenith angle of 70^0. There is less dependence on solar elevation when the light penetrates deeper into the ocean.

Figure 4.8 shows the temporal variation of surface and underwater (only two layers are shown, 3 meters and 10 meters below the sea surface) UVB irradiance for 'normal' ozone abundance (350 DU) and 50% decrease from normal (175 DU) at 65^0N, 45^0N, 25^0N, and 5^0N at local noon and the corresponding relative changes at the surface. The underwater irradiances were calculated for a homogeneous chlorophyll distribution with a concentration of 0.4 $mg\ m^{-3}$. Although a high absolute value of UVB irradiance occurs in the summer at lower latitudes, the highest relative increase of UVB radiation occurs when the sun is low in early spring at higher latitudes. In the equatorial region, the highest absolute value of UVB irradiance happens in the spring time, but the relative increase of UVB due to a 50% reduction of total ozone abundance remains almost constant at 47%. At 65^0N a 50% ozone depletion results in 70% increase in UVB on April 1 and about 54% increase in June and July. The largest relative increase happens to coincide with the time when ozone depletions are expected to be the most severe in the polar regions in early spring. Although the percent increase is greatest then, the actual flux of UV is low at that time because of the long pathlengths. It is so

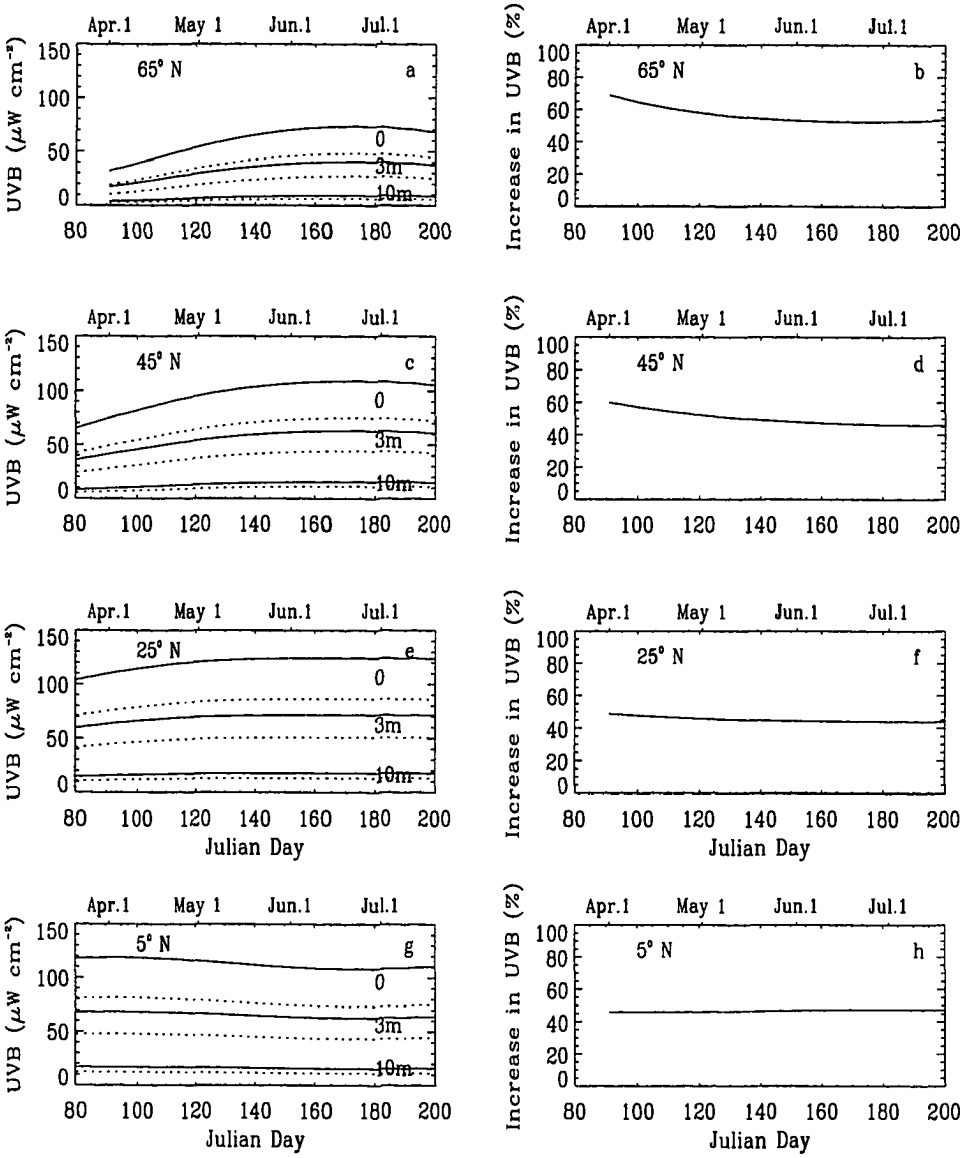

Figure 4.8 Temporal variations of surface and underwater UVB irradiance for total ozone abundance of 350 DU (dotted lines) and 175 DU (solid lines) (left panels) and the relative increases of UVB irradiance due to ozone reduction from 350 DU to 175 DU (right panels). (a) and (b) are for 65^0N, (c) and (d) for 45^0N, (e) and (f) for 25^0N, and (g) and (h) for 5^0N.

low, in fact, that there is little impact on phytoplankton until later in the season when solar elevation increases (*Arrigo*, 1994). There is little seasonal variation at 25^0N and almost no seasonal change at equatorial latitudes in the relative increase of UVB exposure due to ozone reduction, with variations ranging from 45 - 50% enhancement in UVB at 25^0N to 47% at the equator resulting from 50% ozone depletion. The actual biological damage incurred by an increase in UVB exposure will depend on to what extent the ecosystem (or individual species of concern) is already experiencing UVB levels close to the 'tolerance threshold' prior to the ozone depletion.

4.5 UV and Visible Radiation Penetration into the Ocean

The biological effects of the radiation depends sensitively on its spectral distributions. Deleterious biological effects are mainly associated with the shortest wavelengths (UVB, 280–320 nm); photorepair takes place in the UVA range (320–400 nm), while photosynthesis occurs in the photosynthetically active region (PAR) of the spectrum between 400 and 700 nm. Atmospheric ozone absorbs strongly and selectively. Changes in ozone abundance affect UVB strongly, UVA weakly and

[0] This section is based on material previously published as J. Zeng, Z. Jin, and K. Stamnes, Impact of Stratospheric Ozone Depletion on UV Penetration into the Ocean at High Latitudes, *Underwater Light Measurements*, H. Chr. Eilertsen (Editor), Proc. SPIE, Volume 2048, pp. 56-63, 1993.

PAR moderately.

The Sun returns to the Arctic in late March when the solar radiation begins to enter the biosphere. Figure 4.9 shows the temporal variation of surface UVB, UVA, and PAR radiation (left panels) for normal O_3 amount (350 DU) and 30% decrease from normal (250 DU) at 70^0 N at local noon. The right panels show the corresponding relative increases of UVB, UVA, and PAR from normal O_3 abundance and 30% less than normal. We can see that the increase in surface UVB radiation is relatively high when the sun is low (just as it returns to the arctic regions) in early spring . There is a 36% increase in surface UVB on April 1 and a 27% increase at summer solstice at 70^0 N (Figure 4.9b) when total O_3 abundance reduces 30% from normal. Although PAR is generally considered to be relatively insensitive to atmospheric O_3 concentrations, a close inspection of the O_3 cross sections (Figure 2.1b) reveals that PAR is absorbed between 450 and 700 nm, peaking at 610 nm. At low sun O_3 depletion affects the absorption of PAR and leads to a 1.4% increase on April 1 if O_3 concentration reduces to 30% of normal, as illustrated in Figure 4.9f. Ozone has little effect on the transmission of UVA, however, since O_3 absorption is weak in this range (Figure 2.1b and Figure 4.9d). (Note that the scales in Figure 4.9 are different in each panel).

Phytoplankton dwell in the upper layers of the water; they would, in the photic zone, be exposed to any increase in solar ultraviolet radiation. It is important to note that, all other factors remaining constant, ozone depletion will result in increased transmission of solar UVB radiation through the atmosphere and into the water column. Figure 4.10 shows seasonal UVB irradiance penetration to selected depths of water under normal ozone levels and 30% less than normal at

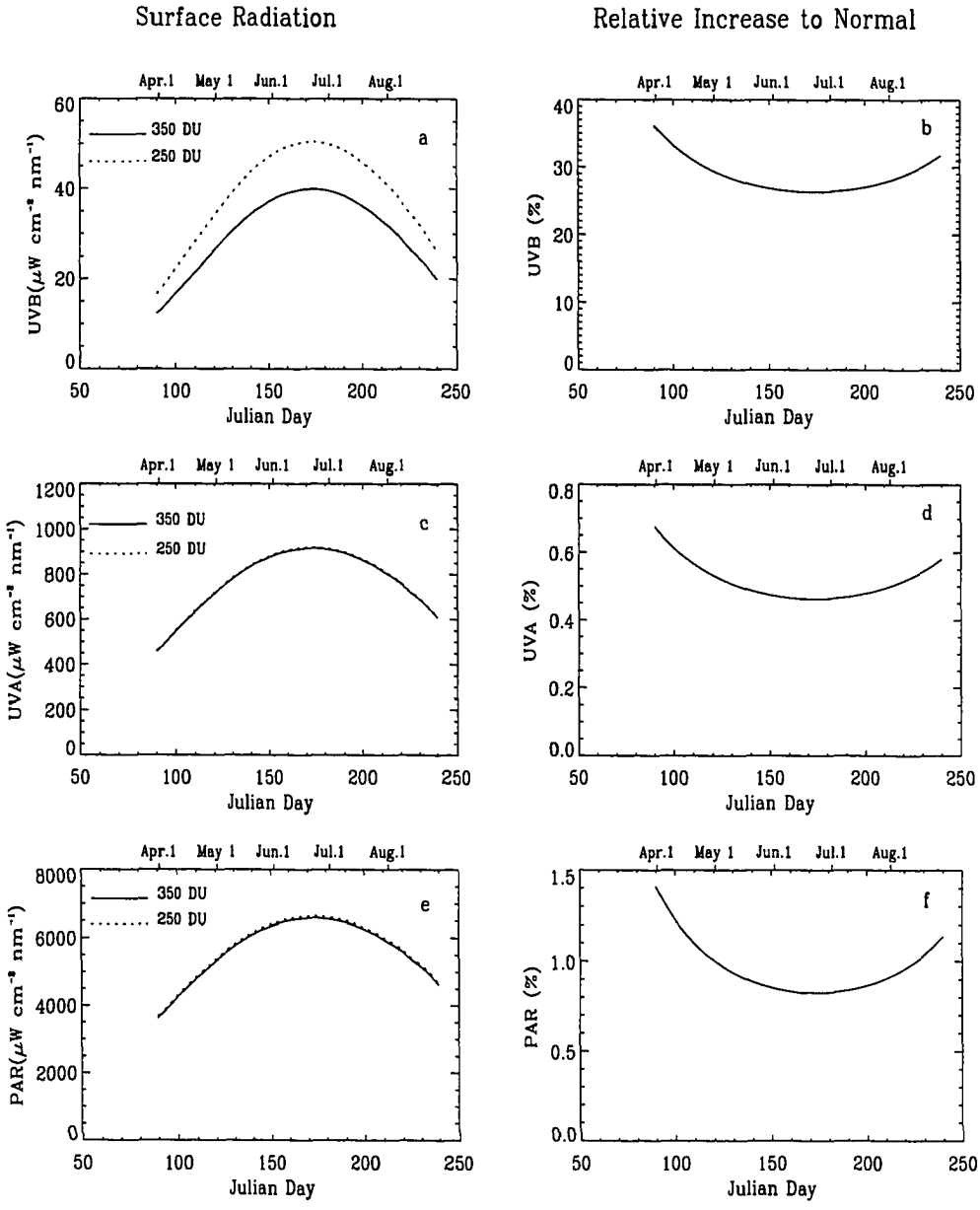

Figure 4.9 Temporal changes of UVB, UVA, and PAR surface irradiance at 70^0N at local noon in ozone abundance of 350 DU and 250 DU, and their corresponding relative changes from normal level (350 DU). (a) and (b) are for UVB, (c) and (d) for UVA, and (e) and (f) for PAR. Note the ordinate scales are different in each panel.

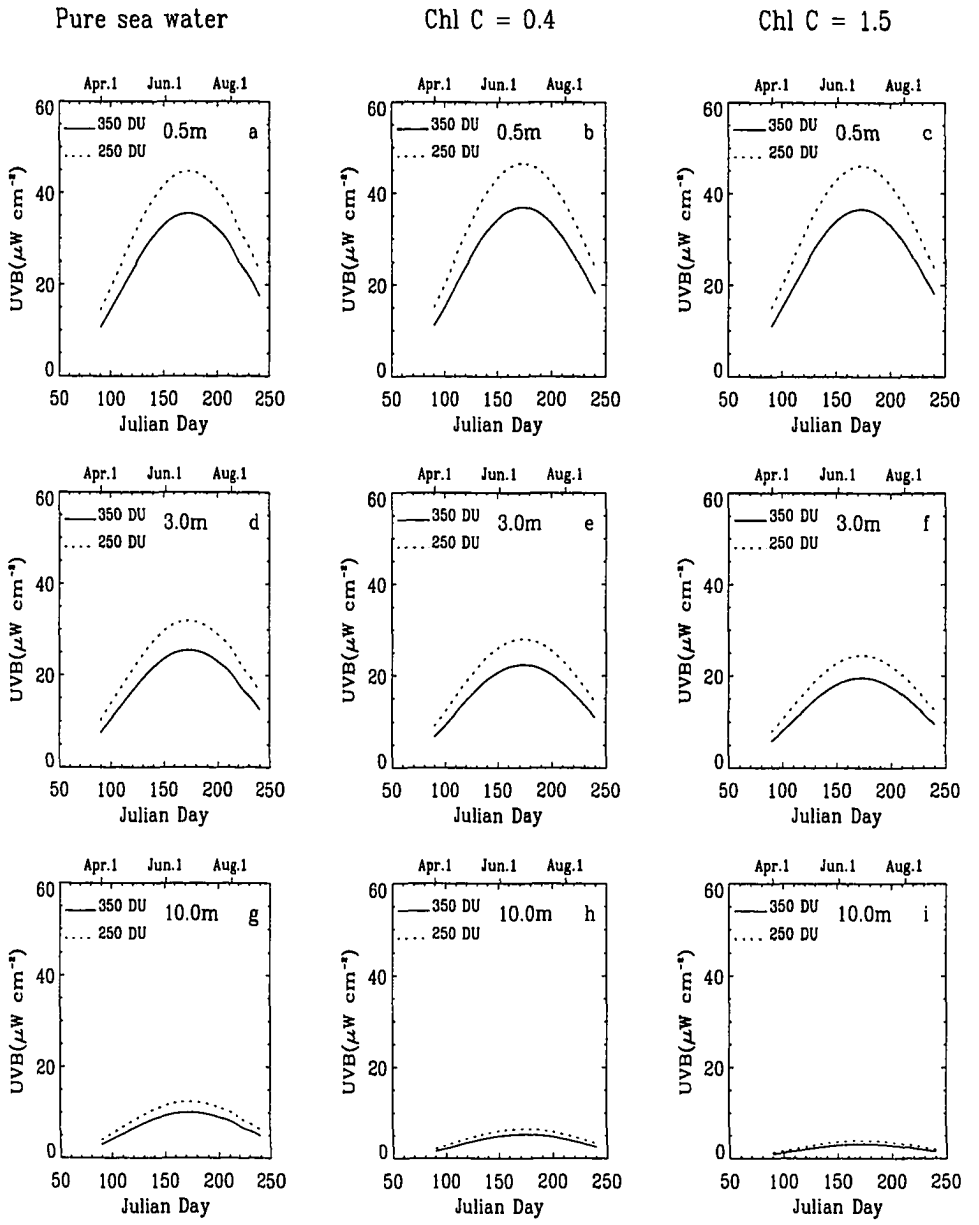

Figure 4.10 Temporal changes of downwelling UVB at 0.5 m (upper panels), 3.0 m (middle panels), and 10.0 m (lower panels) at $70^0 N$ at local noon in ozone abundance of 350 DU and 250 DU. First column is for pure sea water (a, d, and g); second column (b, e, and h) for chlorophyll concentration of 0.4 $mg\ m^{-3}$; and the third column (c, f, and i) for chlorophyll concentration of 1.5 $mg\ m^{-3}$.

70^0 N in different types of waters: pure sea water (Figure 4.10a, d, g), chlorophyll concentrations of 0.4 $mg\ m^{-3}$ (Figure 4.10b, e, h) and 1.5 $mg\ m^{-3}$ (Figure 4.10c, f, i). An ozone depletion of 30% compared to normal will increase UVB exposure 10 meters below the surface from as much as 33% on April 1 to 23% at summer solstice in the three types of water considered here.

Similar results for 35^0N shown in Figure 4.11 reveal that the relative increase of UVB exposure at each level due the same reduction of total ozone abundance is almost independent of the chlorophyll concentration in the water column. Chlorophyll pigment reduces the penetration of UVB radiation into the water. The more the chlorophyll pigment, the less is the UVB transmission. The absorption of solar radiation by phytoplankton is proportional to chlorophyll content.

The ratio of irradiance of UVB to PAR provides a measurement of the energy available for UVB damage to that available for photorepair and/or photosynthesis (*Smith and Baker*, 1989). Figure 4.12 and Figure 4.13 show the impact of ozone depletion on irradiance ratios of UVB to PAR at selected depths in three different types of water at 70^0N and 35^0N respectively. As the behavior of UVB irradiance, the ratio of UVB to PAR in the water column increases by the reduction of ozone abundance. The UVB/PAR ratio decreases with depth, but the reduction value with depth is not as much as that of UVB alone. We note that the UVB/PAR ratio is relatively unaffected by the chlorophyll concentration at both high and low latitudes implying that species that depend on a certain level of PAR for photosynthesis and will be exposed to a similar level of UVB regardless of chlorophyll content.

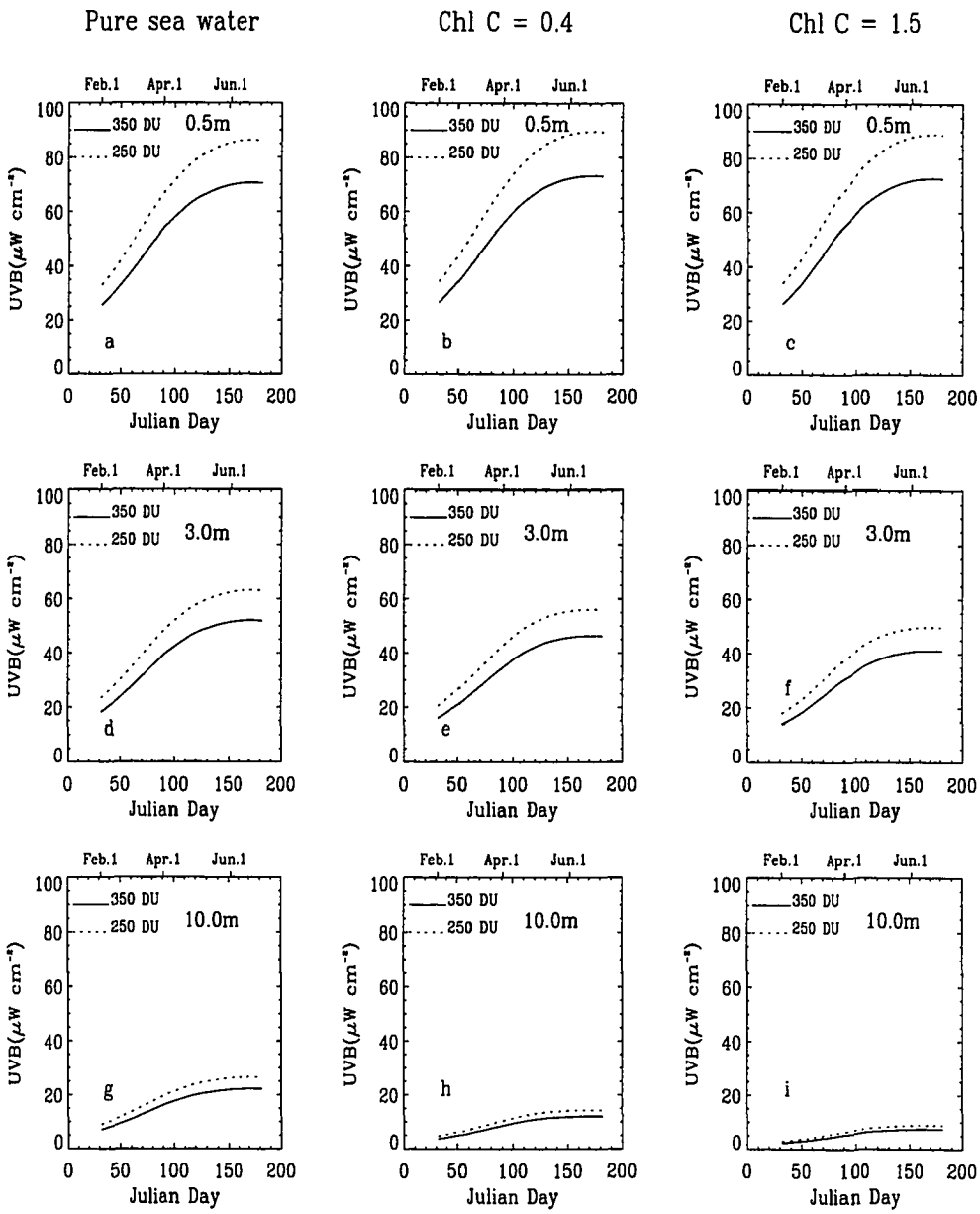

Figure 4.11 As in Figure 4.10 but for 35^0N.

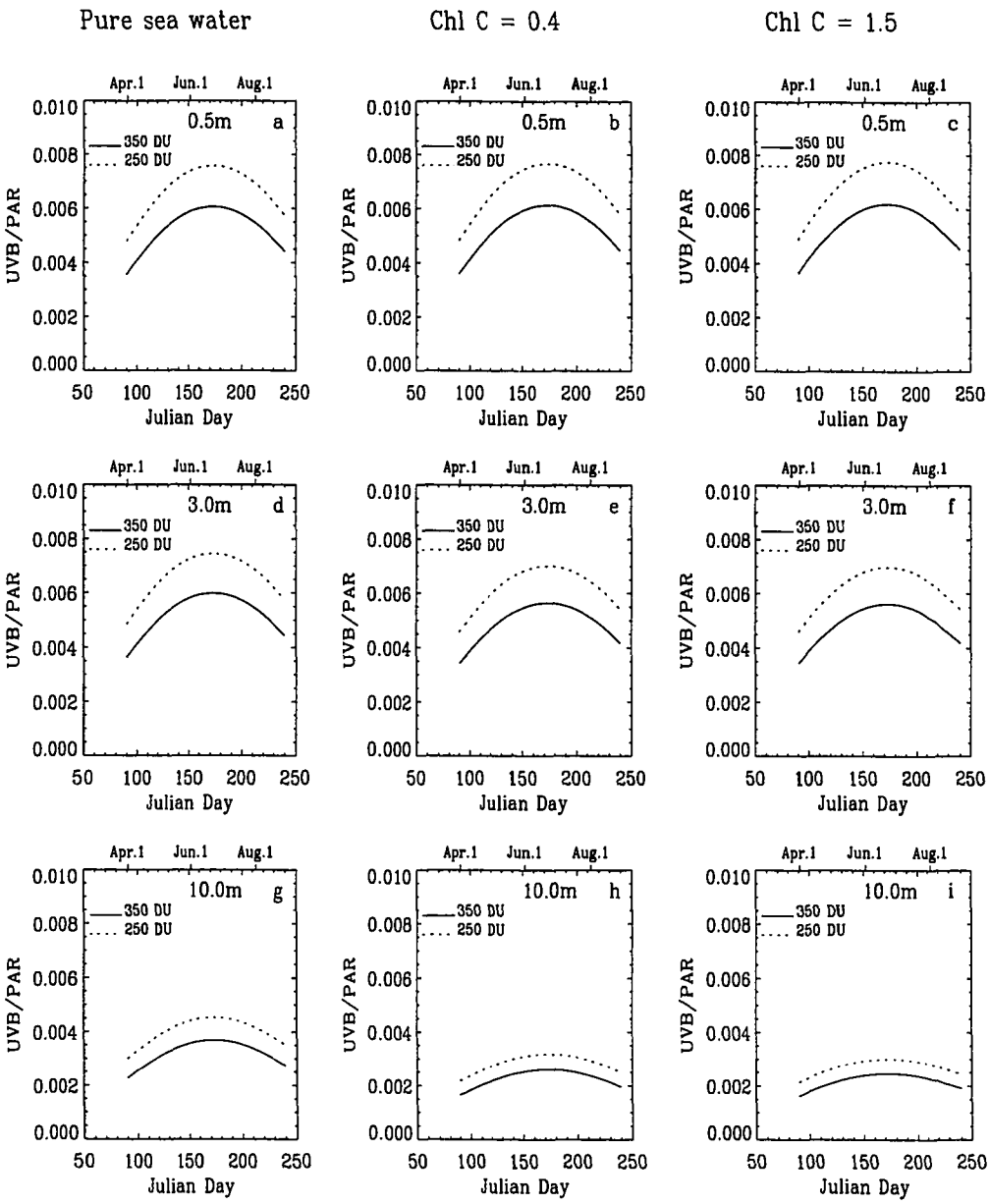

Figure 4.12 As in Figure 4.10, but for the ratios of UVB to PAR irradiance.

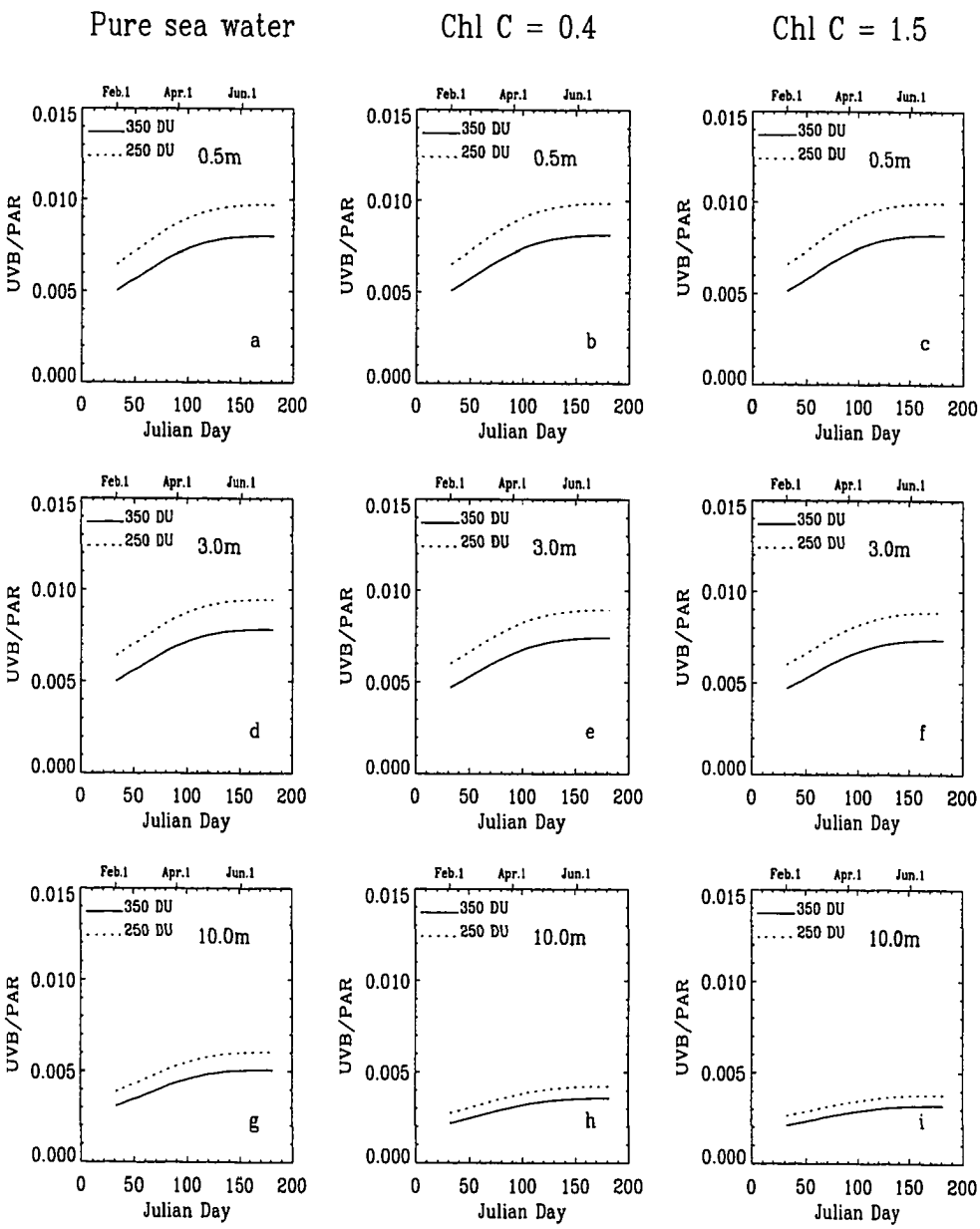

Figure 4.13 As in Figure 4.12 but for $35^0 N$.

4.6 Summary and Discussion

A comprehensive UV radiation model for the coupled atmosphere-ocean system has been described. The model rigorously accounts for multiple scattering and properly treats the radiative coupling between the atmosphere and the ocean resulting from the change in refractive index at the interface between the two strata. The air and water are each divided into a sufficient number of layers to resolve the optical properties of the atmosphere and the underlying water. This model was used to study the impact of ozone depletion on UVB penetration into aquatic systems, and the results were compared with measurements made in the marginal ice zone of the Bellingshausen Sea in austral spring of 1990. There is good qualitative agreement between modeled and measured submarine spectral irradiance from 300 to 350 nm and the ratio of UVB (280 - 320 nm) to total (280 - 700 nm) irradiance. In the spectral range 400 - 700 nm there is a disagreement between modeled and measured underwater spectral irradiance; a more likely possibility for the differences is that the attenuation coefficients of pure sea water used in the model computation are in error.

Stratospheric ozone depletion will significantly increase the penetration of ultraviolet radiation through the atmosphere and into various depths of the ocean. The UV radiation is heavily absorbed in the uppermost layers of the water system. The largest relative increase of UVB radiation arriving at the ocean surface and to various depths in the water occurs at low solar elevations. The most pronounced relative increase in UVB exposure occurs in early spring in the polar regions, which happens to be the time when ozone depletion is expected to be the most severe.

However, the increased transmission of UVB beneath the ozone hole may have only a minor impact on the phytoplankton community because the absolute value of UVB irradiance is low. At lower latitudes there is little seasonal variation of UVB increase due to the same ozone depletion. The more chlorophyll content in the water, the more UVB radiation was absorbed, but the irradiance ratio of UVB to PAR is almost unaffected by chlorophyll concentration.

Phytoplankton relies on solar radiation for photosynthesis. Primary productivity is proportional to PAR light intensity, but photoinhibition of primary productivity is proportional to UVB. Ozone depletion increases UVB radiation arriving at the earth's surface and to various layers of the ocean, but has little influence on PAR penetration. Therefore, decrease in ozone abundance will decrease net primary productivity.

Solar radiation and essential nutrient availability are the dominant physical factors controlling phytoplankton production in the sea. The amount of light varies with latitude, and the amount of nutrients contained in the euphotic zone is largely determined by physical factors controlling vertical mixing of water. Despite year-round high light intensity, tropical regions are generally low in productivity because solar heating stabilizes the water column and nutrients remain at low concentrations within the euphotic zone. Conversely, polar regions are generally high in nutrients but low in solar radiation except for a brief period in the summer. Therefore, a single pulse of phytoplankton abundance occurs during the summer in polar regions. Maximum annual productivities are generally found in temperate latitudes where light and nutrients are both reasonably abundant.

Ozone depletion is generally expected in the early spring in the polar regions.

Therefore, ozone depletion has little impact on primary productivity on a global scale.

The accurate computation of UV radiation reaching the earth's surface is important to model the underwater UV levels accurately. Precise knowledge of the optical properties of the atmosphere are required for this purpose. To make accurate predictions of UV exposure in the water body the proper optical properties of the water column must also be known correctly.

Chapter 5

Apparent Optical Properties in the Water Body

5.1 Introduction

Natural waters, both fresh and saline, are a combination of dissolved and particulate matter. These solutes and particles are both optically significant and highly variable in kind and concentration. Consequently, the optical properties of natural waters show large temporal and spatial variations.

The large-scale optical properties of water are conveniently divided into two mutually exclusive classes: inherent and apparent. Inherent optical properties are those properties that depend only upon the medium, and therefore are independent of the ambient light field within the medium. The two fundamental inherent optical properties are the absorption coefficient and the volume scattering function. Other inherent optical properties include the index of refraction, the beam

attenuation coefficient and the single scattering albedo. Apparent optical properties are those properties that depend both on the medium and on the geometric (directional) structure of the ambient light field, and that display enough regular features and stability to be useful descriptors of the water body. Commonly used apparent optical properties are the irradiance reflectance, the average cosine, and the various diffuse attenuation coefficients. The inherent optical properties specify the optical properties of natural waters in a form suited to the needs of radiative transfer theory, and radiative transfer theory provides the connection between the inherent optical properties and the apparent optical properties. Unlike inherent optical properties, apparent optical properties cannot be measured on water samples, because they depend on the ambient radiance distribution found in the water body itself. An ideal apparent optical property changes only slightly with external environmental changes, but changes enough from one water body to the next characterizing the different optical properties of the two water body.

There are few quantitative links between apparent optical properties and external environmental factors. It is very useful to investigate the sensitivity of apparent optical properties to changes in external environmental and internal intrinsic factors by using a coupled atmosphere-ocean radiative transfer model described in Section 4.2. In the following sections we will discuss two apparent optical properties, spectral irradiance reflectance and vertical diffuse attenuation coefficient.

5.2 Spectral Irradiance Reflectance

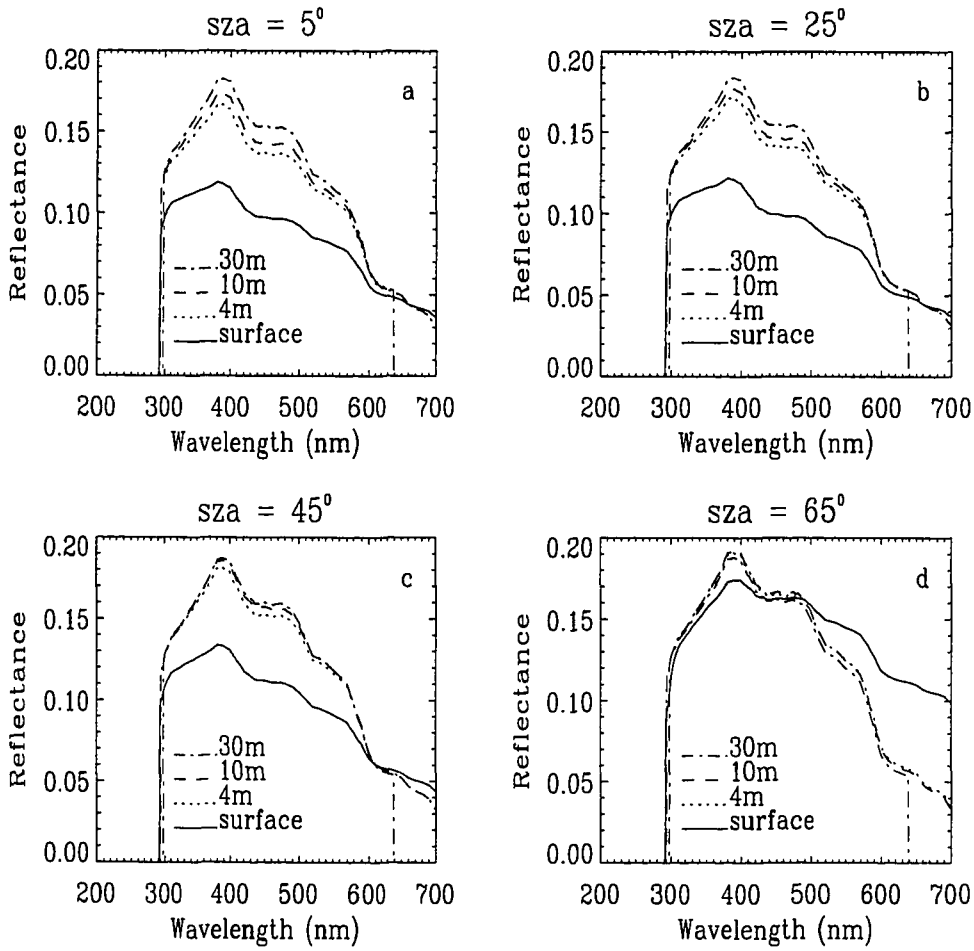

Figure 5.1 Sensitivity of irradiance reflectance at selected depths to changes in solar zenith angle (*sza*). The solid curves are the irradiance reflectances right above the water surface, dotted lines are for 4 meters below surface, dashed lines for 10 meters below surface, and dash-doted lines for 30 meters below surface.

There are many factors affecting the irradiance reflectance of a water body. It is useful to utilize a radiative transfer model to investigate their impact on surface and underwater reflectance. The spectral irradiance reflectance at selected depths is defined as:

$$R(z;\lambda) = \frac{E_u(z;\lambda)}{E_d(z;\lambda)} \tag{5.1}$$

where E_u and E_d are the spectral upwelling and downwelling irradiance respectively, and $z = 0$ at the ocean surface. Figure 5.1 shows the computed irradiance reflectance at the ocean surface and at selected depths for solar zenith angles of 5^0, 25^0, 45^0, and 65^0. This figure pertains to clear sky conditions and a chlorophyll concentration of 0.5 $mg\ m^{-3}$. The surface reflectance represents the albedo of the total water body which includes the contributions to $E_u(0;\lambda)$ by direct-solar and diffuse-sky radiance reflected upward by the water. It is noted that the surface and underwater irradiance reflectances have the highest value at the wavelength of 390 nm, where both phytoplankton and water absorptions are relatively small, and decrease towards both ends of the spectrum. The surface albedo remains relatively high in the red, but submarine reflectances drop greatly in this range. The underwater reflectances decrease greatly as the wavelengths shorten towards UVB (they become zero at the wavelengths shorter than 300 nm because there is little radiation incident on the surface at these wavelengths) and also small in the red where the water is highly absorbing. The underwater spectral reflectances change slightly with depth in the ocean. The spectral surface albedo becomes large when the sun is low, as expected, but the changes in submarine reflectance with solar elevation are much less than those at the surface. Underwater spectral irradiance

reflectances are higher than the surface albedo when the sun is high, but they are lower than the surface albedo when the sun is low enough.

Figure 5.2 shows the sensitivity of spectral surface albedo to changes in chlorophyll concentration and their relative increase compared to those for pure sea water. Figure 5.2a and c are for a clear sky and Figure 5.2b and d are for a cloudy sky with a cloud optical depth of 50. An obvious feature of these curves of spectral surface albedo is that the surface albedos both in pure sea water and in specific chlorophyll concentration are higher for cloudy sky conditions than those for clear sky throughout the whole spectrum (300 - 700 nm). Another feature of spectral surface albedo is that its highest value occurs at 390 nm and this value does not change much with chlorophyll concentration varying between 0.13 and 0.14 under clear as well as cloudy sky conditions. The surface albedos increase with chlorophyll concentration in the wavelength ranges of 290 - 320 nm and 520 - 700 nm. The surface albedo becomes zero at the wavelengths shorter than 290 nm, because there is no irradiance incident to the ocean surface. The low spectral surface albedo for pure sea water implies that pure sea water traps most of the solar radiation entering into the water body. There is a low value of surface albedo at about 430 nm as chlorophyll pigment increases, due to the strong absorption by phytoplankton at this wavelength. Figure 5.2c and d present the corresponding increases of surface albedo to that over pure sea water under clear and cloudy skies. The largest increase in surface albedo occurs around 560 nm because chlorophyll absorption is small at this wavelength. Although there are also low values of chlorophyll absorption between 570 nm and 650 nm (Figure 4.2b), the relative increase of surface albedo compared to pure sea water is low, because the absorp-

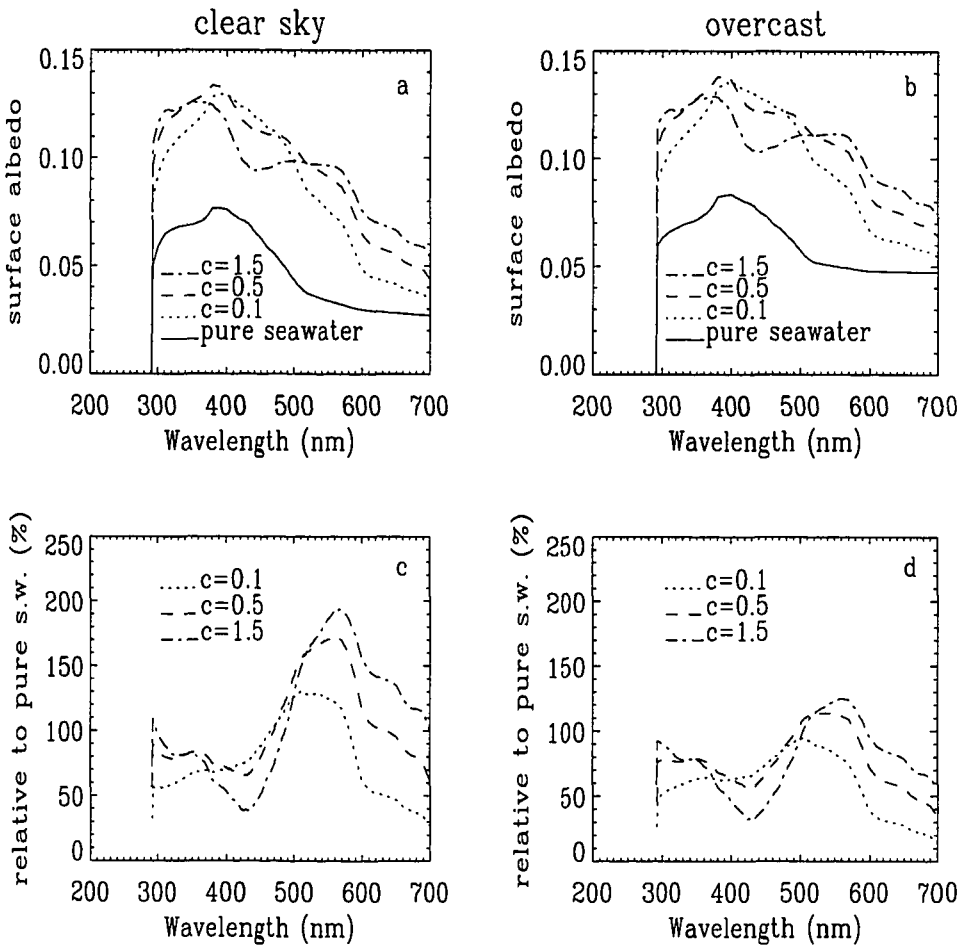

Figure 5.2 Sensitivity of spectral surface albedo to chlorophyll concentration under clear and cloudy skies. The left panels are the surface albedos under clear sky in different chlorophyll concentrations (a) and their corresponding relative increases to those in pure sea water (c); the right panels (b) and (d) are for cloudy sky with cloud optical depth of 50. The solar zenith angle of 45^0 is used in the model calculations.

tion by pure sea water is high at these wavelengths (Figure 4.2a) and compensates for the low absorption by chlorophyll.

Figure 5.3 shows the sensitivity of spectral surface albedo to chlorophyll concentration at high sun ($sza = 25^0$) and low sun ($sza = 65^0$). An intercomparison of Figure 5.2 and Figure 5.3 reveals that the surface albedo at wavelengths between 290 and 330 nm changes both with chlorophyll concentration and solar elevation; the more phytoplankton in the water and lower the sun, the larger is the surface albedo.

The relative increases of spectral surface albedo for different chlorophyll concentration compared to that in pure sea water are somewhat smaller under cloudy sky conditions (Figure 5.2d) and at high solar zenith angles (Figure 5.3d). In other words, spectral irradiance reflectance of a water body is a function of chlorophyll concentration, sky condition, and solar elevation.

5.3 Diffuse Attenuation Coefficient

The downward diffuse attenuation coefficient in Equation 4.2 is defined in terms of the decrease with depth of the ambient downwelling irradiance $E_d(z;\lambda)$, which is comprised of photons heading in all downward directions. Similar to Equation 4.2 the upward diffuse attenuation coefficient is defined as

$$K_u(z;\lambda) = -\frac{d\ln E_u(z;\lambda)}{dz} \tag{5.2}$$

where E_u is the upwelling irradiance. K_u pertains to photons heading in all upward directions.

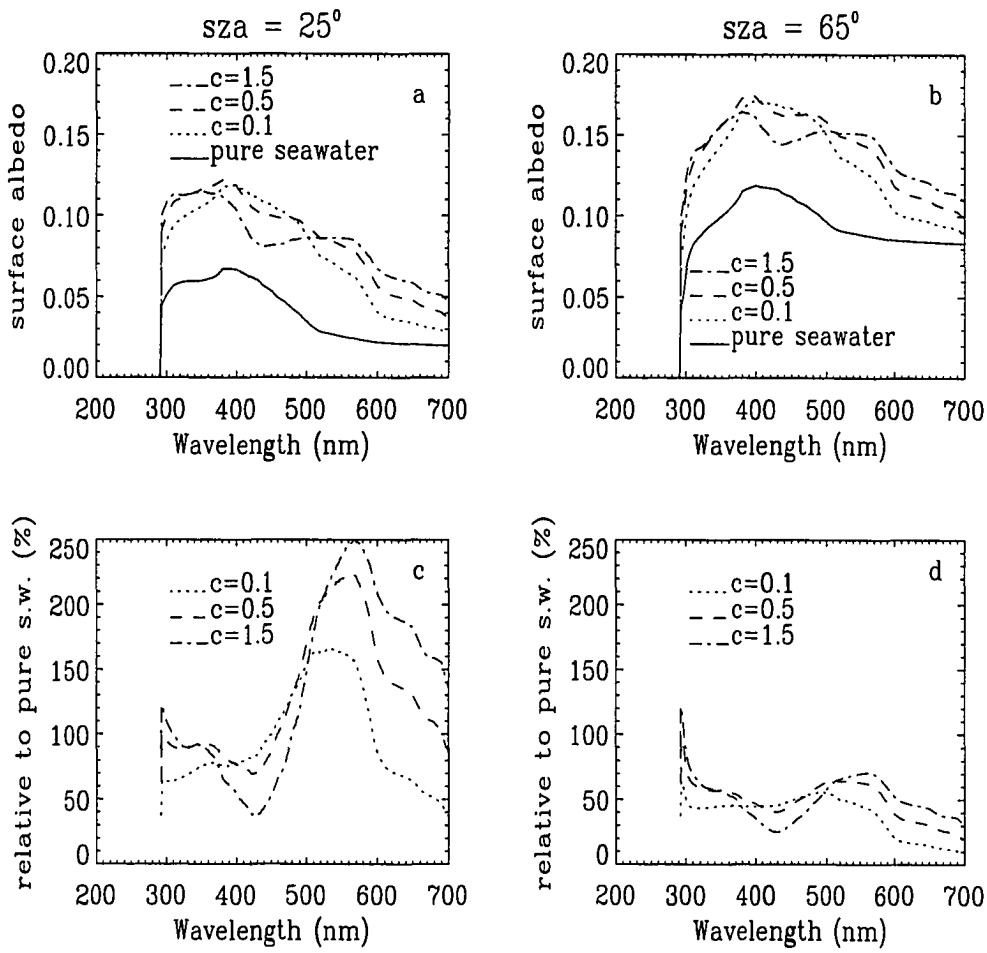

Figure 5.3 Sensitivity of spectral surface albedo to chlorophyll concentration at different solar zenith angles under clear sky. The left panels are the surface albedos at solar zenith angle of 25° in different chlorophyll concentrations (a) and their corresponding relative increases to those in pure sea water (c); the right panels (b) and (d) are for solar zenith angle of 65°.

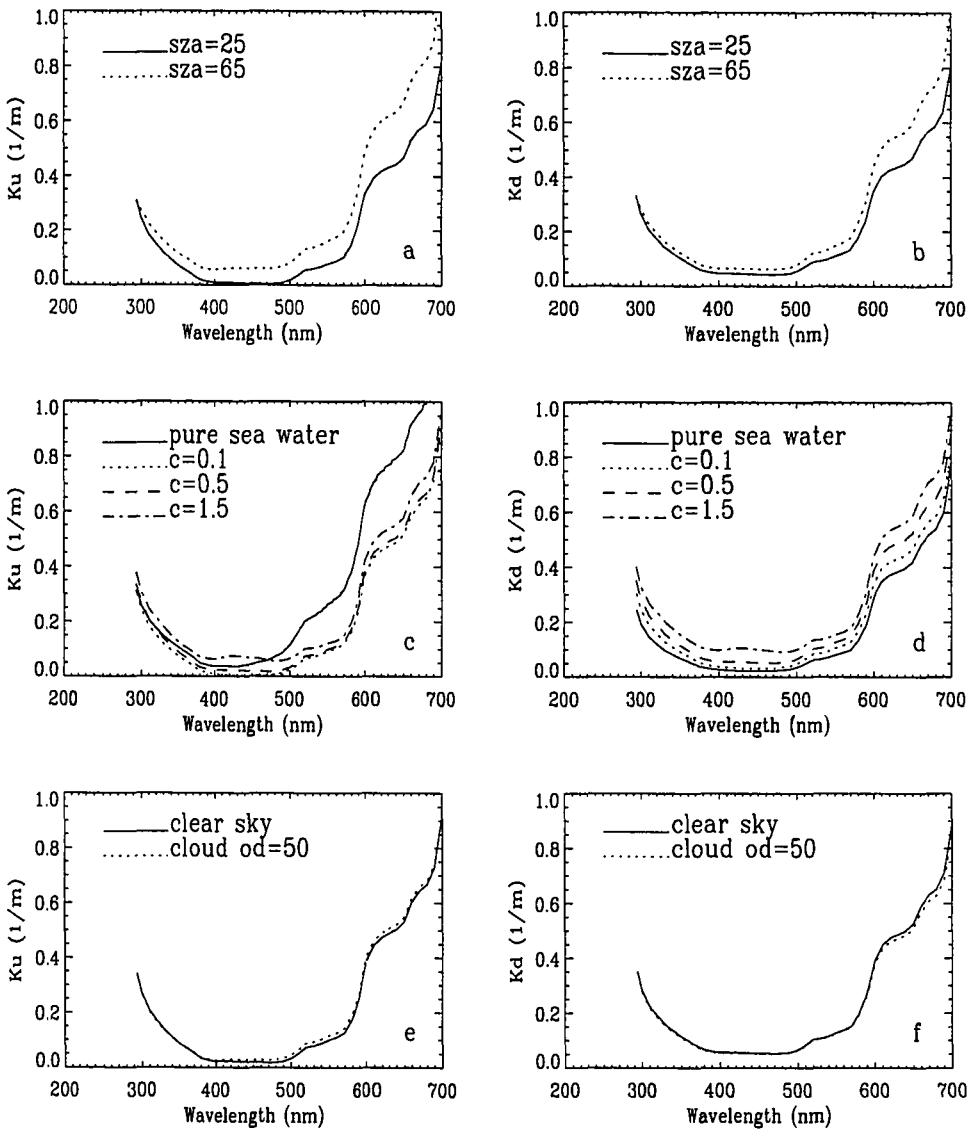

Figure 5.4 Sensitivity of diffuse attenuation coefficients for upwelling (left panels) and downwelling (right panels) irradiance to solar zenith angle (*sza*), chlorophyll concentrations, and sky conditions. (a) and (b) show the upward and downward diffuse attenuation coefficient for solar zenith angles of 25^0 (solid lines) and 65^0 (dotted line); (c) and (d) for different chlorophyll concentration: pure sea water (solid lines), c = 0.1 (dotted lines), c = 0.5 (dashed lines), and c = 1.5 (dash-dotted lines) $mg\ m^{-3}$; and (e) and (f) for different sky condition: clear sky (solid lines) and cloudy sky (dotted lines) with optical depth of 50.

In homogeneous (vertically well mixed) waters, the diffuse attenuation coefficients depend only weakly on depth, but they clearly depend on the directional structure of the ambient light field. Figure 5.4 provides a sensitivity test of diffuse attenuation coefficients for different solar zenith angles (sza), chlorophyll concentrations, and sky conditions, for upwelling and downwelling irradiance. We used a chlorophyll concentration of 0.5 $mg\ m^{-3}$ in the calculations of Figure 5.4a, b, e, and f; clear sky in Figure 5.4a, b, c, and d; solar zenith angle of 45^0 in Figure 5.4c, d, e, and f. The values of spectral diffuse attenuation coefficient for upwelling and downwelling irradiance are different in each panel, but commonly, the coefficients are shaped similar to that of pure sea water absorption shown in Figure 4.2, with small values at wavelengths between 390 - 500 nm and increasing towards the red (above 500 nm) and ultraviolet (below 390 nm).

Obviously, the diffuse attenuation coefficients for both downwelling and upwelling irradiance are sensitive to chlorophyll concentration in the water column (Figure 5.4c and d). Actually the diffuse attenuation coefficient is highly correlated with chlorophyll concentration, which can be seen clearly from the following formula (*Gordon*, 1989)

$$K_d(\lambda) \approx \frac{a(\lambda) + b_b(\lambda)}{\cos\theta_{sw}} \tag{5.3}$$

where $a(\lambda)$ and $b_b(\lambda)$ are respectively the absorption coefficient and the total backscatter coefficient (including contributions by pure water and by particles). Both of the coefficients are inherent optical properties; θ_{sw} is the solar zenith angle measured within the water. Since $a(\lambda) \gg b_b(\lambda)$ for most waters, K_d is largely determined by the absorption properties of the water, which are fairly well param-

eterized by the chlorophyll concentration.

Figure 5.4c and d show that the spectral downward diffuse attenuation coefficient increases with chlorophyll pigment content, with the lowest value for the pure sea water. However, the situation for the upward diffuse attenuation coefficient is different. It still increases in the water containing phytoplankton, like the downward diffuse attenuation coefficient, with chlorophyll concentration, but crosses that for pure sea water at 470 nm. Above this wavelength the upward diffuse attenuation coefficient in pure sea water is higher than that in the water containing phytoplankton.

The spectral diffuse attenuation coefficients are strongly dependent on solar elevation, which also can be seen in the above Equation 5.3 (note that our solar zenith angle is different from θ_{sw}, but they are related by Snell's law), with higher values at low sun than at high sun. This feature is even more pronounced in the red (Figure 5.4a and b). Physically this means that there is greater decrease of both upwelling and downwelling irradiance with depth at low sun than that at high sun.

Unlike the effects of solar zenith angle and chlorophyll concentration on the diffuse attenuation coefficients, clouds have only small affect on them (upward or downward) (Figure 5.4e and f). There is also very little influence of the atmospheric ozone content on the spectral diffuse attenuation coefficient (not shown) for both the upwelling and downwelling irradiance.

In fact, the diffuse attenuation coefficient is also affected by the sea state (roughness) in the ocean surface. *Gordon* (1989) indicated that there is an increasingly diffuse incident light field beneath the surface as the roughness increases. This

increases the diffuse attenuation coefficient with increasing roughness. However, we will not discuss this effect because our model does not include surface waves.

The diffuse attenuation coefficient is an apparent optical property which strongly depends on the ambient light field. It is very sensitive to solar zenith angle and chlorophyll concentration, but less sensitive to cloud cover and atmospheric ozone.

5.4 Summary of the Chapter

Apparent optical properties arise when bulk radiometric quantities other than radiance are used to describe the light field in the water body. They depend on both the medium and the environmental conditions. Unlike inherent optical properties, the apparent optical properties can not be measured on water samples, because they depend on the ambient radiance distributions.

The sensitivities of the spectral irradiance reflectance and diffuse attenuation coefficient to solar zenith angle, cloud cover, and chlorophyll concentration, were examined by using a coupled atmosphere-ocean radiative transfer model. The solar zenith angle and cloud cover are external environmental factors that affect the ambient light field. The chlorophyll concentration characterizes the intrinsic property of the water body.

The spectral surface albedo is very sensitive to solar elevation, cloud cover, and chlorophyll concentration. There are obvious differences between the values of surface albedo and underwater irradiance reflectances. The spectral surface albedo is smaller than the underwater reflectance when the sun is high, but it increases with solar zenith angle and becomes larger than underwater reflectance

when the sun is low enough. The underwater irradiance reflectance depends less on solar zenith angle than does the surface albedo. The underwater irradiance reflectances change little with depth especially at high solar zenith angles. The spectral surface albedo is higher under an overcast sky than under a clear sky. Pure sea water has lower surface albedo than water containing chlorophyll pigment. The largest increase of surface albedo in water containing chlorophyll relative to that in the pure sea water is at about 560 nm as chlorophyll absorption is small at this wavelength. The surface albedo increases with chlorophyll concentration in the wavelength ranges from 290 - 320 nm and 520 - 700 nm.

Vertical diffuse attenuation coefficients for upwelling and downwelling irradiance are similar in shape to pure sea water absorption coefficients. The smallest values are between 390 and 500 nm, and they increase towards both ends of the spectrum. They also increase with solar zenith angle, but depend weakly on sky conditions. They are highly dependent on chlorophyll concentration in the water body. The diffuse attenuation coefficients for downwelling irradiance increase with chlorophyll concentration, but the dependence of those for upwelling irradiance on chlorophyll concentration changes with wavelength.

Chapter 6

Summary and Suggestions for Future Studies

The primary goal of this work has been to investigate the impact of stratospheric ozone depletion on the UV radiation penetration through the atmosphere and the underlying aquatic system. In Chapter 2 a comprehensive radiative transfer model was used to calculate surface spectral ultraviolet irradiance under cloud-free conditions. The results are compared with measurements made at Lauder, New Zealand (45^0S, 170^0E) before and after the eruption of Mt. Pinatubo, and including a snow-covered surface. There is reasonable agreement between measured and calculated diffuse, direct, and global irradiances over the range 300 to 450 nm. Discrepancies may be due to calibration errors in the UV measurements, or in the extraterrestrial irradiances input to the model. Ratios of diffuse/direct irradiances are independent of such uncertainties in calibrations and therefore provide a sensitive test of the model. If appropriate ozonesonde data, surface albedo, and aerosol

optical properties are used, the model ratios are in satisfactory agreement with measurements over a wide range of observing conditions. For cases in which the atmospheric optical properties are best known the agreement is better than 8% in the UV-B range, and for wavelengths 320 to 450 nm the deviation is smaller. The comparison suggests that the ultraviolet radiation exposure can be computed with confidence for clear sky conditions if the appropriate atmospheric molecular density profiles, ozonesonde data, surface albedo, and aerosol optical properties are available. The UV radiation model is used to investigate the impact of changes in solar zenith angle, ozone abundance, surface albedo, and aerosol loading on UV radiation reaching the surface of the earth. The ratios of diffuse to direct irradiance depend critically on solar zenith angle, surface albedo and aerosol extinction. Ozone changes have pronounced effects on the global UVB irradiance, but have only a minor effect on these ratios.

In Chapter 3 ground-based spectral UV irradiances were tied to satellite data over Antarctica and the Arctic by using a radiative transfer model. The total column ozone abundance in the Arctic was relatively larger in spring than in summer. Ozone depletion is not obvious in Barrow, Alaska, but it is very severe in Antarctica in spring. The comparison of total ozone abundance between TOMS data and that derived from model computation by using the ground-based measurement at two different wavelengths (one more strongly absorbed by ozone than the other) shows generally good agreement. A small systematic difference between the two methods occurs in the austral summer and winter (South Pole, McMurdo, and Palmer station). In Barrow there is also a systematic difference between the two methods symmetrically about summer solstice. The possible causes for this

systematic difference may be the inconsistency of temperature profiles used in the derivations with those used in the TOMS algorithm and the errors introduced from the solar irradiance measurements. The agreement between TOMS and derived column ozone can be improved by the use of two distinct irradiance measurements at a narrow wavelength interval at wavelengths shorter than 340 nm. The inference of cloud equivalent optical depth in Antarctica shows that the closer to the South Pole, the thinner is the cloud optical depth.

In Chapter 4 a radiation model for the coupled atmosphere-ocean system was described and used to compute the UV penetration through the atmosphere and into the underlying water column. Comparisons between model computations and measurements of UV spectral irradiance between 300 and 350 nm, and the ratio of UVB (280 - 320 nm) to total (280 - 700 nm) irradiance show good agreement. There is disagreement in submarine spectral irradiance from 470 to 700 nm between the model and measurement which cannot be explained by errors in phytoplankton absorption. Although the cause of the disagreement is unresolved, one possible reason for the discrepancy is the pure sea water attenuation coefficients used in the model computations. For a given reduction of ozone abundance the largest relative increase of computed UVB radiation arriving at the sea surface and penetrating to various depths in the ocean occurs at large solar zenith angles. The UV radiation is absorbed in the uppermost layers of the water system. At high latitudes the most pronounced increase in UVB exposure due to an ozone depletion happens in early spring when ozone depletion is expected to be the most severe.

In Chapter 5 we discussed the sensitivities of some commonly used apparent optical properties of the water body to the changes in both environmental con-

ditions and the intrinsic optical properties by using a coupled atmosphere-ocean radiative transfer model. The spectral reflectances for both the surface and submarine irradiance are very sensitive to changes in solar elevation, cloud cover, and chlorophyll concentration in the water body. The surface albedos increase with solar zenith angle, and are higher for cloudy than for clear sky conditions. They also increase with chlorophyll concentration in the wavelength ranges of 290 - 320 nm and 520 -700 nm. The diffuse attenuation coefficients for downwelling and upwelling irradiance are sensitive to solar elevation and chlorophyll concentration, but they rarely depend on sky conditions. The spectral diffuse attenuation coefficients for both downwelling and upwelling irradiance increase with solar zenith angle, and those for downwelling irradiance increase with chlorophyll concentration in the water body. The dependence of diffuse attenuation coefficients for upwelling irradiance on chlorophyll concentration varies with wavelength.

In the future, more observational studies and UV climatology modeling should be undertaken:

- Ancillary parameters that affect UV penetration through the atmosphere must be measured at the same time as UV spectral measurements are made in order to test UV radiation models. These parameters include surface albedo, profiles of atmospheric temperature, pressure, ozone, aerosol, and relevant pollutants (depending on the site, these may include NO_2, SO_2, and other atmospheric constituents), and optical properties of clouds, in addition to solar zenith angle and total ozone abundance. The intercomparison, refinement, and testing of UV radiative transfer models will help us understand and predict UV radiation penetrating to various layers of the atmosphere and the earth surface.

• Extensive measurements are needed in order to test models of the submarine UV light field. The optical properties in the water column are not well known at present, especially in the UVB region. First we should re-evaluate the absorption and scattering coefficient for pure water and pure sea water. It is usually very difficult to make underwater measurement in the ultraviolet region because there are few photons in this region. We also need to measure the spectral absorption and scattering coefficients for phytoplankton, dissolved organic matter, and organic detritus over a wide range of waters from very clear to very turbid conditions.

• The asymmetry factors of phase functions both for the atmosphere (clouds, aerosols) and underlying water (phytoplankton, dissolved organic matter, and organic detrituse) are wavelength dependent. We need more field measurements to determine the dependence in order to make correct UV predictions.

• The accuracy of UV prediction using our discrete ordinate radiative transfer model can be within a few percent if the necessary input parameters are known. These parameters include total ozone abundance and its vertical distribution, surface albedo, cloud cover, and aerosol loading. The total ozone abundance and its vertical distribution, cloud types and their optical depths, aerosol vertical distribution and its optical properties, can be derived from satellite data. It is possible to assimilate these data into the model and use vertical profiles based on climatology for atmospheric pressure and temperature and climatological estimates of surface albedo to make surface UV radiation prediction. This makes it possible to assess the UV environment from space.

• There are several versions of the extraterrestrial solar spectrum in current use. There are some differences between them, especially in the UV range. We can

make an intercomparison among them with the help of satellite. We need a high resolution accurate solar spectrum in order to make correct ultraviolet radiation prediction.

References

Anderson, J.G., D.W. Toohey, W.H. Brune, Free radicals within the Antarctic vortex: the role of CFCs in Antarctic ozone loss, *Science, 251*, 39, 1991.

Anderson, G.P., S.A. Clough, F.X. Kneizys, J.H. Chetwynd, and E.P. Shettle, AFGL Atmospheric Constituent Profiles (0-120 km), AFGL-TR-86-0110, AFGL (OPI), Hanscom AFB, MA 01736, 1987.

Arrigo, K. R., Impact of ozone depletion on phytoplankton growth in the Southern Ocean: large scale spatial and temporal variability, *Mar. Ecol. Prog. Ser.*, in press, 1994.

Bener, P., Approximate values of intensity of natural ultraviolet radiation for different amounts of atmospheric ozone, *Final Technical Report, European Research Office, United States Army, London, Contract No DAJA37-68-C-1077*, 59, 1972.

Bricaud, A., A. Morel, and L. Prieur, Absorption by dissolved organic matter of the sea (yellow substance) in the UV and visible domains, *Limnol. Oceanogr., 26(1)*, 43-53, 1981.

Bruhl, C. and P. J. Crutzen, On the Disproportionate Role of Tropospheric Ozone as a Filter Against Solar UV-B Radiation, *Geophys. Res. Lett., 16*, 703, 1989.

Cullen, J. C., P. J. Neal, and M. P. Lesser, Biological weighting function for the inhibition of phytoplankton photosynthesis by ultraviolet radiation, *Sciences, 258*, 646-650, 1992.

Dahlback, A. and K. Stamnes, A new spherical model for computing the radiation field available for photolysis and heating at twilight, *Planet. Space Sci., 29*, 671-683, 1991.

Dahlback, A., T. Henriksen, S.H. Larsen and K. Stamnes, Biological UV-doses and the effect of an ozone layer depletion, *Photochemistry and Photobiology, 49*, 621, 1989.

Davies, R., Increased Transmission of Ultraviolet Radiation to the Surface Due to Stratospheric Scattering, *J. Geophys. Res., 98*,7251-7253, 1993.

DeLuisi, J. J., E. G. Dutton, K. L. Coulson, T. E. DeFoor, and B. G. Mendonca, On some radiative features of the El Chichon volcanic stratospheric dust cloud and a cloud of unknown origin observed at Mauna Loa, *J. Geophys. Res., 88, C11*, 6769-6772, 1983.

DeMore, W.P., S.P. Sander, D.M. Golden, M.J. Molina, R.F. Hampson, M.J. Kurylo, C.J. Howard, and A.R. Ravishankara, Chemical kinetics and photochemical data for use in stratospheric modeling, *JPL Publication 90-1*, Jet Propulsion Laboratory, Pasadena, 1990.

El-Sayed,S. Z., F. C. Stephens, R. R. Bidigare, and M. E. Ondrusek, *Antarctic Ecosystems, Ecological Change and Conservation*, Kerry, K. R. & Hempel, G. (eds.) Springer-Verlog, 379, 1990.

Farman, J. C., B. G. Gardiner, and J. D. Shanklin, Large losses of total ozone in Antarctica reveal seasonal ClO_x/NO_x interaction, *Nature, 315,* 207, 1985.

Fefèvre, F., D. Cariolle, S. Muller, and F. Karcher, Total ozone from the TIROS operational vertical sounder during the formation of the 1987 "ozone hole", *J. Geophys. Res., 96*, 12893-12911, 1991.

Frederick, J. E., H. E. Snell, and E. K. Haywood, Solar ultraviolet radiation at the Earth's surface, *Photochemistry and Photobiology, 50*,8, 443-450, 1989.

Gaudry, A., P. Monfray, G. Polian, and G. Lambert, The 1982-1983 El Nino: A 6 billion ton CO_2 release, *Tellus 39B,* 209, 1987.

Gordon, H.R., Can the Lambert-Beer law be applied to the diffuse attenuation coefficient of ocean water?, *Limnol. Oceanogr., 34(8)*, 1389, 1989.

Gordon, H. R. and A. Y. Morel, in *Remote Assessment of Ocean Color for Interpretation of Satellite Visible Imagery: A Review*, Springer-Verlag, New York, 1983.

Gordon, H.R., Radiative transfer in the ocean: a method for determining absorption and scattering properties, *Appl. Opt., 15*, 2611-2613, 1976.

Grenfell, T., S. G. Warren, and P. C. Mullen, Reflection of solar radiation by the Antarctic snow surface at ultraviolet, visible, and near-infrared wavelengths, *J. Geophys. Res., 99*, D9, 18669-18684, 1994.

Häder, D.-P. and R.C. Worrest, Effects of enhanced solar radiation on aquatic ecosystems, *Photochem. Photobiol., 53*, 717-725, 1991.

Häder, D.-P., R. C. Worrest, and H. D. Kumar, Aquatic Ecosystems, *Environmental Effects of Ozone Depletion: 1991 update*, 33, 1991.

Herman, J.R., R. Hudson, R. McPeter, R. Stolarski, Z. Ahmad, X.Y. Gu, S. Taylor, and C. Wellemyer, A new self-calibration method applied to TOMS and SBUV backscattered ultraviolet data to determine long-term global ozone change, *J. Geophys. Res., 96*, 7531-7545, 1991.

Hofmann, D.J., J.W. Harder, S.R. Rolf, and J.M. Rosen, *Nature, 322*, 59, 1987.

Holm-Hansen, O., E. W. Helbling, and D. Lubin, Ultraviolet Radiation in Antarctica Inhibition of Primary Production, *Photochemistry and Photobiology, 58,* 567-570, 1993.

Houghton, R.A. and G.M. Woodwell, Global climactic change, *Sci. Amer., 260*, 36-44,

1989.

Jerlov, N. G., in *Marine Optics*, Elsevier, New York, 1976.

Jin, Z. and K. Stamnes, Radiative Transfer in Nonuniformly Refracting Layered Media such as the Atmosphere/Ocean System, *Appl. Opt., 33*, 431, 1994.

Karentz, D., DNA repair mechanisms in Antarctic marine organisms, Antarctic, *J. of the U.S., 23*, 114, 1988.

Kattawar, G., and C. Adams, Stokes vector calculations of the submarine light field in an atmosphere-ocean with scattering according to a Rayleigh phase matrix: effect of interface refractive index on radiance and polarization, *Limnol. Oceanogr., 34*, 1453-1472, 1989.

Kirk, J., Monte Carlo procedure for simulating the penetration of light into natural waters, *Division of Plant Industry Tech. Paper 36*, Commonwealth Scientific and Industrial Research Organization, Canberra, Australia, p. 16, 1981.

Kylling, A. and K. Stamnes, Efficient yet accurate solution of the linear transport equation in the presence of internal sources: the exponential-linear approximation, *J. Comp. Phys., 102*, 265-276, 1992.

Leontyeva, E. and K. Stamnes, Estimations of cloud optical thickness from ground-based measurements of incoming solar radiation in the Arctic, *J. of Climate, 7*, No. 4, 1994.

Liou, K.N., An introduction to atmospheric radiation, Academic Press, Inc., San Diego, 1980.

Lubin, D. and J.E. Frederick, Column ozone measurements from Palmer Station, Antarctica: variations during the austral springs of 1988 and 1989, *J. Geophys. Res., 95*, 13883-13889, 1990.

Madronich, S., Implications of recent total atmospheric ozone measurements for biologically active ultraviolet radiation reaching the Earth's surface, *Geophys. Res. Lett., 19*, 37-40, 1992.

McClatchey, R. A., R. W. Fenn, J. E. A. Selby, F. E. Volz, and J. S. Garing, Rep. AFCRL-72-0497, (Air Force Cambridge Research Laboratories, Bedford, Mass., 1972).

McCormick, M.P., R.E. Veiga, and W.P. Chu, Stratospheric ozone profile and total ozone trends derived from SAGE I and SAGE II data, *Geophys. Res. Lett., 19*, 269-272, 1992.

McElroy, M.B., R.J. Salawitch, S.C. Wofsy, and J.A. Logan, Reductions of Antarctic ozone due to synergistic interactions of chlorine and bromine, *Nature 321*, 759, 1986.

McKenzie, R. L. UV spectral irradiance measurements in New Zealand: effects of Pinatubo volcanic aerosol, Ozone in the Troposphere and Stratosphere, *NASA Conference Publication 3266*, 627-630, 1994.

McKenzie, R. L., P. V. Johnston, M. Kotkamp, A. Bittar, and J. D.Hamlin, Solar ultraviolet radiometry in New Zealand: instrumentation and sample results from 1990,

Appl. Optics, 31, 30, 6501-6509, 1992.

Michelangeli, D. V., M. Allen, Y. L. Yung, R-L. Shia, D. Crisp, and J. Eluszkiewicz, Enhancement of Atmospheric Radiation by an Aerosol Layer, *J. Geophys. Res., 97*, 865-874, 1992.

Mobley, C. D., a numerical model for the computation of radiance distributions in natural waters with wind-roughened surfaces, *Limnol. Oceanogr., 34*, 1473-1483, 1989.

Mobley, C. D., B. Gentili, H. R. Gordon, Z. Jin, G. W. Kattawar, A. Morel, P. Reinersman, K. Stamnes, and R. H. Stavn, Comparison of numerical models for computing underwater light fields, *Appl. Opt., 32*, 7484 1993.

Mobley, C. D., in *Light and Water, Radiative Transfer in Natural Water*, Academic Press, 92, 1994.

Molina, L. T. and M. J. Molina, Absolute absorption cross section of ozone in the 185-to 350-nm wavelength range, *J. Geophys. Res., 91*,14501, 1986.

Morel, A. and B. Gentili, Diffuse reflectance of oceanic waters: its dependence on Sun angle as influenced by the molecular-scattering contribution, *Appl. Opt., 30*, 4427-4438, 1991.

Nicolet, M., On the Molecular Scattering in the Terrestrial Atmosphere: An Empirical Formula for its Calculation in the Homosphere, *Planet Space Sci., 33*, 1467-1468, 1984.

Nicolet, M., Solar spectral irradiances with their diversity between 120 and 900 nm, *Planet Space Sci., 37*, 1249-1289, 1989.

Paur, R. J. and A. M. Bass, Standard reference instrument for the assay of ozone, *AM. Chem. Soc. Abstracts., 186*, 169, 1983.

Rosen, J. M., and N. T. Kjome, Backscattersonde: a new instrument for atmospheric aerosol research, *Appl. Optics, 30*, 1552-1561, 1991.

Russell, P. B., J. M. Livingston, R. F. Pueschel, J. A. Reagan, E. V. Browell, G. C. Toon, P. A. Newman, M. R. Schoeberl, L. R. Lait, L. Pfister, Q. Gao, and B. M. Herman, Post-Pinatubo optical depth spectra vs. latitude and vortex structure: airborne tracking sunphotometer measurements in AASE II,*Geophys. Res. Lett., 20*, 2571-2574, 1993.

Sathyendranath, S., L. Lazzara and L. Prieur, Variations in the spectral values of specific absorption of phytoplankton, *Limnol. Oceanogr., 32(2)*, 403-415, 1987.

Schippnick, P. F., and A. E. S. Green, Analytical Characterization of Spectral Actinic Flux and Spectral Irradiance in the Ultraviolet, *Photochem. Photobiol., 35*, 89-101, 1982.

Songandares, F., Z.-F. Qi, and E. S. Fry, Spectral absorption of water, presentation at the *Optical Society of America Annual Meeting*, San Jose, CA, 1991.

Smith, R. C. and K. S. Baker, The bio-optical state of ocean waters and remote sensing,

Limnol. Oceanogr., 23, 247-259, 1978a.

Smith, R. C. and K. S. Baker, Optical classification of natural waters, *Limnol. Oceanogr., 23*, 260-267, 1978b.

Smith, R. C. and K. S. Baker, Penetration of UV-B and biologically effective dose-rates in natural waters, *Photochem. Photobiol., 29,* 311, 1979.

Smith, R. C. and K. S. Baker, Stratospheric Ozone, Middle Ultraviolet Radiation, and Carbon-14 Measurements of Marine Productivity, *Science, 208,* 592, 1980.

Smith, R. C. and K. S. Baker, Optical Properties of the Clearest Natural Waters, *Appl. Opt., 20,* 177, 1981.

Smith, R. C., and K. S. Baker, Stratospheric ozone, middle ultraviolet radiation and phytoplankton productivity, *Oceanography, 2,* 4, 1989.

Smith, R.C., Z. Wan, and K.S. Baker, Ozone depletion in Antarctica: modeling its effect on solar UV irradiance under clear-sky conditions, *J. Geophys. Res., 97*, 7383-7397, 1992a.

Smith, R. C., B. B. Prezelin, K. S. Baker, R. R. Bidigare, N. P. Boucher, T. Coley, D. Karentz, S. MacIntyre, H. A. Matlick, D. Menzies, M. Ondrusek, Z. Wan, and, K. J. Waters, Ozone Depletion: Ultraviolet Radiation and Phytoplankton Biology in Antarctic Waters, *Science, 255,* 952, 1992b.

Stamnes, K., S.-C. Tsay, W. Wiscombe, and K. Jayaweera, Numerically stable algorithm for discrete-ordinate-method radiative transfer in multiple scattering and emitting layered media, *Appl. Optics, 27,* 2502-2509, 1988.

Stamnes, K., J. Slusser, and M. Bowen, Derivation of total ozone column abundance from spectral irradiance measurements, *Appl. Optics, 30*, 4418-4426, 1991.

Stamnes, K., Z. Jin, J. Slusser, C. Booth, and T. Lucas, Several-Fold Enhancement of Biologically Effective Ultraviolet Radiation Levels at McMurdo Station Antarctica during the 1990 Ozone "Hole", *Geophys. Res. Lett., 19*, 1013, 1992.

Stamnes, K., The Stratosphere as a Modulator of Ultraviolet Radiation into the Biosphere, *Surv. in Geophys., 14*, 167, 1993.

Stolarski, R., R. Bojkov, L. Bishop, C. Zerefos, J. Staehelin, and J. Zawodny, Measurred trends in the stratospheric ozone, *Science, 256*, 342-349, 1992.

Teillet, P. M., Rayleigh optical depth comparisons from various sources, *Applied Optics, 29*, 1897-1900, 1990.

Thomas, G., and K. Stamnes, Radiative transfer in Atmospheres and oceans, Cambridge U. Press, Cambridge, in preparation, 1995.

Tsay, S.-C. and K. Stamnes, Ultraviolet Radiation in the Arctic: The Impact of Potential Ozone Depletions and Cloud Effects, *J. Geophys. Res. 97*, 7829, 1992.

United Nations Environment Programme (UNEP), Environmental Effects Panel Report,

Nairobi, Kenya, 1989.

United Nations Environment Programme (UNEP), Environmental Effects of Ozone Depletion: 1991 Update, Nairobi, Kenya, 1991.

Van Hoosier, M. E., J. -D. F. Bartoe, G. E. Brueckner, and D. K. Prinz, Absolute solar spectral irradiance 120 nm - 400 nm (Results from the Solar Ultraviolet Spectral Irradiance Monitor - SUSIM - Experiment on board Space Lab- 2), *Astro. Lett. and Communications, 27*, 163-168, 1988.

Wang, P. and J. Lenoble, Comparison between measurements and modeling of UV-B irradiance for clear sky: a case study, *Appl. Opt., 33,* 3964, 1994.

Wiscombe, W. J., The delta-M method: rapid yet accurate radiative-flux calculations for strongly asymmetric phase functions, *J. Atmos. Sci., 34,* 1408-1422, 1977.

Worrest, R. C., The effect of solar UV-B radiation on aquatic systems: An overview, *Effects of Changes in Stratospheric Ozone and Global Climate, Overview*, J.G. Titus, ed., US Environmental Protection Agency and United Nations Environmental Program 1, 175, 1986.

WMO, Scientific assessment of ozone depletion: 1991, *World Meteorological Organization, Global Ozone Research and Monitoring Project - Rep. No. 25,*, 1992.

WMO, Global ozone research and monitoring project: Atmospheric ozone 1985, *World Meteorological Organization, Rep. No. 16,* Volume 1, 1985.

Zeng, J., K. Stamnes, Z. Jin, and K.R. Arrigo, Ozone depletion and UV penetration to the earth surface and into the underlying water, submitted to *Limnol. Oceanogr.*, 1995.

Zeng, J., R. McKenzie, K. Stamnes, M. Wineland, and J. Rosen, Measured UV spectra compared with discrete ordinate method simulations, *J. Geophys. Res.,99*, 23019-23030, 1994.

Zeng, J., Z. Jin, and K. Stamnes, Impact of stratospheric ozone depletion on UV penetration into the ocean at high latitudes, *Underwater Light Measurements,* H. Chr. Eilertsen (Editor), Proc. SPIE, Volume 2048, pp. 56-63, 1993.